

**Nonlinear Phenomena in a Pure Electron Plasma  
Studied with a 2-D Fluid Code**

Thesis by

David A. Bachman

In Partial Fulfillment of the Requirements  
for the Degree of  
Doctor of Philosophy

California Institute of Technology  
Pasadena, California

1998  
(Submitted September, 1997)

© 1998  
David A. Bachman  
All Rights Reserved

## Acknowledgements

It has been a pleasure and a privilege to work towards my Ph.D. under the expert guidance of Professor Roy Gould. He provided clear explanations of concepts I struggled over, and more resources than any graduate student deserves. Along with technical knowledge, I have also gained much knowledge outside of plasma physics from our many conversations. I wish to thank Professor Gould for all the effort he has invested in me.

I also want to thank Professor Noel Corngold and Professor Paul Bellan. They were both involved in teaching me many concepts in plasma physics, and greatly assisted in the completion of my degree.

My experiences at Caltech have been interesting and positive. I wish to thank the outstanding faculty and staff for providing me with this positive learning environment. The Caltech staff have always been friendly and more than willing to go out of their way to assist me. Special thanks to Connie Rodriguez for helping me with administrative matters and providing pleasant conversation.

I would also like to thank the Office of Naval Research and the contract monitor Dr. Charles Roberson for funding this effort in non-neutral plasmas. Without Dr. Roberson's strong support for the program, non-neutral plasma physics would not be where it is today.

Fellow graduate students Jimmy Yee, Freddy Hansen and Steve Sanders provided very useful feedback on the rough draft of this manuscript. This thesis was significantly improved by their involvement.

I want to thank my parents for their constant support of my educational goals. Without their encouragement, I could not have progressed this far in my education. I also received emotional support from my girlfriend, Yun Huang. She provided the final encouragement I needed to complete this thesis.

# Abstract

This thesis presents a new computational tool for studying cylindrical pure electron plasmas. Previous research used linear methods to describe the evolution of small plasma perturbations. This new tool numerically solves the nonlinear two-dimensional (2-D) fluid equations in cylindrical coordinates, allowing the exploration of many phenomena that have been observed experimentally in these plasmas. Most experimentally observed phenomena are large in amplitude and follow nonlinear dynamics. Clearly, codes based on the linearized equations can not reproduce these nonlinear phenomena.

The plasma was first studied for small amplitude perturbations using the nonlinear fluid code, producing results that agree with linearized calculations. The perturbed electric field decays in time, due to shear in the flow of density perturbations at different radii, which results in the total contribution to the perturbed electric field phase mixing away.

At higher amplitudes, the decay envelope becomes modulated, which is a result that has been observed experimentally and is also reproduced by this fluid code. The modulation is caused by nonlinear trapping of fluid elements within the wave, which is illustrated in images of the perturbed density.

For two applied pulses separated in time, a third echo response is observed after the responses to the two applied pulses have decayed away. Echoes have been observed experimentally in neutral plasmas, but have not yet been observed experimentally in non-neutral plasmas.

At very high amplitudes, a nonlinear decay instability occurs. A high amplitude wave decays into a wave with lower azimuthal symmetry number due to an interaction occurring at the beat frequency between the two waves. The beat-wave decay instability has been observed experimentally, and is also observed using the 2-D nonlinear fluid code.

The 2-D cylindrical nonlinear fluid code is capable of reproducing a wide range of non-neutral plasma phenomena, and is an important new tool for future research on non-neutral plasmas. This research is also relevant to ordinary fluids, since the equations describing a non-neutral plasma are analogous to the 2-D Euler equations for an inviscid fluid.

# Contents

<b>Acknowledgements</b>	<b>iii</b>
<b>Abstract</b>	<b>iv</b>
<b>1 Introduction</b>	<b>1</b>
1.1 Overview . . . . .	1
1.2 Background . . . . .	2
1.3 Pure Electron Plasma Geometry . . . . .	4
1.3.1 Plasma Confinement . . . . .	4
1.3.2 Trap Operation . . . . .	4
1.3.3 Parameters in the Caltech Pure Electron Plasma Experiment .	6
1.4 Previous Work at Caltech . . . . .	7
1.5 Thesis Outline . . . . .	9
<b>2 The Fluid Model</b>	<b>12</b>
2.1 Introduction . . . . .	12
2.2 Model Assumptions and Approximations . . . . .	13
2.2.1 Approximations to Maxwell's Equations . . . . .	13
2.2.2 Approximation of a Two-dimensional Plasma . . . . .	14
2.2.3 Approximation of Zero Pressure Gradient . . . . .	14
2.2.4 Drift Approximation . . . . .	15
2.3 Steady-State Angular Velocity . . . . .	16
2.4 Nonlinear Model . . . . .	17
2.5 Normalized Variables . . . . .	18
2.6 Linearized Model . . . . .	19
2.7 Summary . . . . .	22

<b>3 Computational Methods</b>	<b>23</b>
3.1 Introduction . . . . .	23
3.2 Nonlinear Fluid Code . . . . .	24
3.2.1 Poisson's Equation . . . . .	25
3.2.2 Density Derivative Routine . . . . .	29
3.2.3 Leapfrog Time Advance . . . . .	31
3.2.4 Diagnostics and Outputs . . . . .	32
3.2.5 Accumulated Errors . . . . .	36
3.3 Linearized Fluid Code . . . . .	37
3.4 Conclusion . . . . .	39
<b>4 Small Amplitude Disturbances</b>	<b>41</b>
4.1 Introduction . . . . .	41
4.2 Collisionless Damping . . . . .	42
4.2.1 Fast Decay Profile . . . . .	42
4.2.2 Slow Decay Profile . . . . .	49
4.2.3 No Decay Profile . . . . .	52
4.2.4 Other Profiles . . . . .	55
4.2.5 Briggs, Daugherty, and Levy Decay Rate . . . . .	57
4.3 Density Perturbations . . . . .	58
4.3.1 Fast Decay Profile . . . . .	58
4.3.2 Slow Decay Profile . . . . .	60
4.3.3 No Decay Profile . . . . .	63
4.4 Linear Model . . . . .	63
4.5 Conclusion . . . . .	69
<b>5 Fluid Trapping</b>	<b>72</b>
5.1 Introduction . . . . .	72
5.2 Fluid Code Results . . . . .	74
5.2.1 Perturbed Electric Field . . . . .	74
5.2.2 Bounce Frequency Dependence . . . . .	78

5.2.3	Density Perturbations . . . . .	80
5.2.4	BGK-Like Modes . . . . .	87
5.3	Conclusion . . . . .	91
<b>6</b>	<b>Echoes in a Pure Electron Plasma</b>	<b>92</b>
6.1	Introduction . . . . .	92
6.2	Echo Concept . . . . .	93
6.3	Echo Results . . . . .	99
6.3.1	Demonstration of the Echo . . . . .	99
6.3.2	Control Sets . . . . .	102
6.3.3	Amplitude of the Echo . . . . .	107
6.3.4	Higher Amplitude Effects . . . . .	113
6.3.5	Slow Decay Density Profile . . . . .	121
6.4	Conclusion . . . . .	122
<b>7</b>	<b>Beat-Wave Decay Instability</b>	<b>124</b>
7.1	Introduction . . . . .	124
7.2	Fluid Code Results . . . . .	126
7.2.1	Choice of Density Profile . . . . .	126
7.2.2	Demonstration of the Decay Instability . . . . .	128
7.2.3	Growth Rate Versus Amplitude . . . . .	128
7.2.4	Comparison to Experimental Results . . . . .	132
7.3	Conclusion . . . . .	134
<b>8</b>	<b>Conclusion and Future Work</b>	<b>136</b>
8.1	Summary of Results . . . . .	136
8.2	Further Work . . . . .	137
8.2.1	Improvements to the Nonlinear Fluid Code . . . . .	137
8.2.2	Further Research on Non-neutral Plasmas . . . . .	139
	<b>Bibliography</b>	<b>141</b>

# List of Figures

1.1	Schematic diagram of a cylindrical Penning trap. . . . .	5
1.2	Plot of the envelope of the perturbed electric field at the wall versus time on a semilog scale for the experimental data collected by N. Sateesh Pillai. . . . .	8
3.1	Flow chart describing the logic of the nonlinear fluid code. . . . .	26
4.1	Plot of the normalized unperturbed density and normalized angular velocity versus radius for the Fast Decay Profile $n_0(r) = n_0(0)\{1 - 3(\frac{r}{\alpha})^2 + 3(\frac{r}{\alpha})^4 - (\frac{r}{\alpha})^6\}$ with the edge of the plasma at $\alpha = 0.8$ . . . . .	43
4.2	Plot of the perturbed electric field at the wall versus time for the Fast Decay Profile $n_0(r) = n_0(0)\{1 - 3(\frac{r}{\alpha})^2 + 3(\frac{r}{\alpha})^4 - (\frac{r}{\alpha})^6\}$ with $\alpha = 0.8$ . . . . .	45
4.3	Semilog plot of the amplitude of the Fourier components of the electric field at the wall versus time for the Fast Decay Profile $n_0(r) = n_0(0)\{1 - 3(\frac{r}{\alpha})^2 + 3(\frac{r}{\alpha})^4 - (\frac{r}{\alpha})^6\}$ with $\alpha = 0.8$ . . . . .	46
4.4	Fourier components of the electric field at the wall versus time for the Fast Decay Profile $n_0(r) = n_0(0)\{1 - 3(\frac{r}{\alpha})^2 + 3(\frac{r}{\alpha})^4 - (\frac{r}{\alpha})^6\}$ with $\alpha = 0.8$ and a pure $m = 2$ wall excitation. . . . .	48
4.5	Plot of the normalized unperturbed density and normalized angular velocity versus readius for the Slow Decay Profile $n_0(r) = n_0(0)\{1 - 6(\frac{r}{\alpha})^4 + 8(\frac{r}{\alpha})^6 - 3(\frac{r}{\alpha})^8\}$ with the edge of the plasma at $\alpha = 0.8$ . . . . .	50
4.6	Fourier components of the electric field at the wall versus time for the Slow Decay Profile $n_0(r) = n_0(0)\{1 - 6(\frac{r}{\alpha})^4 + 8(\frac{r}{\alpha})^6 - 3(\frac{r}{\alpha})^8\}$ with $\alpha = 0.8$ and a pure $m = 2$ angular wall excitation. . . . .	51
4.7	Plot of the normalized unperturbed density and normalized angular velocity versus radius for the No Decay Profile $n_0(r) = n_0(0)\{1 - 10(\frac{r}{\alpha})^6 + 15(\frac{r}{\alpha})^8 - 6(\frac{r}{\alpha})^{10}\}$ with the edge of the plasma at $\alpha = 0.8$ . . . . .	53

4.8	Plot of the perturbed electric field at the wall versus time on a semilog scale for the No Decay Profile $n_0(r) = n_0(0)\{1 - 10(\frac{r}{\alpha})^6 + 15(\frac{r}{\alpha})^8 - 6(\frac{r}{\alpha})^{10}\}$ , with $\alpha = 0.8$ .	54
4.9	Plot of the normalized density versus radius for the normalized Fermi function with $\beta = 2, 4, 6, 8, 10, 12, 14$ , and $16$ .	56
4.10	Density perturbations at six successive times for the Fast Decay Profile $n_0(r) = n_0(0)\{1 - 3(\frac{r}{\alpha})^2 + 3(\frac{r}{\alpha})^4 - (\frac{r}{\alpha})^6\}$ with $\alpha = 0.8$ .	59
4.11	Density perturbations at six successive times for the Fast Decay Profile $n_0(r) = n_0(0)\{1 - 3(\frac{r}{\alpha})^2 + 3(\frac{r}{\alpha})^4 - (\frac{r}{\alpha})^6\}$ with $\alpha = 0.8$ , assuming the plasma convected in the theta direction at the unperturbed angular velocity, ignoring the self consistent perturbed electric field.	61
4.12	Density perturbations at six successive times for the Slow Decay Profile $n_0(r) = n_0(0)\{1 - 6(\frac{r}{\alpha})^4 + 8(\frac{r}{\alpha})^6 - 3(\frac{r}{\alpha})^8\}$ with $\alpha = 0.8$ .	62
4.13	Density perturbations at six successive times for the No Decay Profile $n_0(r) = n_0(0)\{1 - 10(\frac{r}{\alpha})^6 + 15(\frac{r}{\alpha})^8 - 6(\frac{r}{\alpha})^{10}\}$ with $\alpha = 0.8$ .	64
4.14	Magnitude of density perturbations versus radius at six successive times for the Fast Decay Profile.	67
4.15	Magnitude of continuum density perturbations versus radius for the Fast Decay Profile obtained after the quasimode has decayed away.	68
4.16	Resulting density perturbations for six different times for the Fast Decay Profile using the Quasimode and Continuum mode linear model.	70
5.1	Plot of the envelope of the perturbed electric field at the wall versus time on a semilog scale for the experimental data collected by N. Sateesh Pillai.	73
5.2	Plot of the perturbed electric field at the wall for the Slow Decay Profile, using an applied three cycle pulse amplitude of $4.28 \times 10^{-5}\phi_0$ .	75
5.3	Plot of the perturbed electric field at the wall demonstrating bounce oscillations.	76

5.4	Plot of the envelope of the perturbed electric field versus time on a semilog scale for various amplitude pulses applied to the Slow Decay Profile. . . . .	77
5.5	Plot of the angular bounce frequency versus the perturbed electric field at the wall for 12 high amplitude traces. . . . .	80
5.6	Plot of the envelope of the perturbed electric field at the wall for a typical computation displaying bounce oscillations. . . . .	81
5.7	Images of the total density at six different times. An external Gaussian pulse with a maximum amplitude of $0.005\phi_0$ , and a FWHM of $1.06t_{cr}$ is applied to the Slow Decay Profile. The resulting perturbed electric field at the wall exhibits strong bounce oscillations. . . . .	83
5.8	Images of the perturbed density at six different times for an external Gaussian pulse with a maximum amplitude of $0.005\phi_0$ , and a FWHM of $1.06t_{cr}$ applied to the Slow Decay Profile. The resulting perturbed electric field at the wall exhibits strong bounce oscillations. . . . .	84
5.9	Magnification of the trapped fluid elements causing bounce oscillations. . . . .	86
5.10	Plot of the envelope of the perturbed electric field at the wall resulting from a slow Gaussian pulse applied to the Slow Decay Profile and exciting a BGK-like mode. . . . .	89
5.11	(a) Perturbed density resulting from slowly applying a Gaussian pulse to the Slow Decay Profile, which excites a BGK-like mode. Image (b) is a magnification of the outer plasma edge, stretched out flat. . . . .	90
6.1	Plot of the perturbed electric field at the wall versus time for a calculation which demonstrates the echo. . . . .	100
6.2	Plot of the perturbed electric field at the wall versus time for a one cycle $m_1 = 2$ pulse at time $t = 0$ , and a one cycle $m_2 = 6$ pulse at time $\tau = 25t_{cr}$ applied to the Fast Decay Profile. An echo occurs at time $t = 37.5t_{cr}$ with $m_3 = 4$ azimuthal symmetry. . . . .	101

6.3	Perturbed electric field at the wall versus time for a one cycle pulse with $m = 2$ azimuthal symmetry applied to the Fast Decay Profile. . .	103
6.4	Perturbed electric field at the wall versus time for a one cycle pulse with $m = 4$ azimuthal symmetry applied to the Fast Decay Profile. . .	104
6.5	Perturbed electric field at the wall versus time for a one cycle pulse with $m = 6$ azimuthal symmetry applied to the Fast Decay Profile. . .	105
6.6	Perturbed electric field at wall for a one cycle $m_1 = 4$ pulse at time $t = 0$ , and a one cycle $m_2 = 2$ pulse at time $\tau = 25t_{cr}$ applied to the Fast Decay Profile. Both pulses decay away, with no echo produced. . .	107
6.7	Perturbed electric field at wall for four echo computations varying in applied amplitude. . . . .	109
6.8	Plot of the maximum amplitude of the echo versus applied $m_1 = 2$ amplitude of the first pulse on a log-log scale. . . . .	110
6.9	Plot of the maximum amplitude of the echo versus applied $m_2 = 4$ amplitude of the second pulse on a log-log scale. . . . .	111
6.10	Perturbed electric field at wall for three echo computations, varying the interpulse spacing, $\tau$ . . . . .	112
6.11	Plot of the amplitude of the echo versus interpulse spacing of the applied pulses on a log-log scale. . . . .	114
6.12	Response of the $m_1 = 2$ pulse, $m_2 = 4$ pulse, and $m_3 = 2$ echo response as a function of pulse 1 amplitude and pulse 2 amplitude. . . . .	116
6.13	Perturbed electric field at the wall versus time for two high amplitude applied pulses. . . . .	118
6.14	Semilog plot of a computation demonstrating higher order echoes. . .	119
6.15	Plot of the perturbed electric field at the wall versus time for an $m_1 = 2$ applied pulse at time $t = 0$ , and an $m_2 = 6$ applied pulse at time $\tau = 25t_{cr}$ , demonstrating an echo of an echo. . . . .	120
6.16	Plot of the perturbed electric field at the wall versus time for a computation demonstrating the echo while using the Slow Decay Profile. .	122

7.1	Experimental results of Mitchell and Driscoll for the beat-wave decay instability in a pure electron plasma. . . . .	126
7.2	Plot of the normalized density and normalized angular velocity for the Beat Profile. . . . .	127
7.3	Plot of the envelope of the perturbed electric field at the wall versus time on a semilog scale for the $m = 1, 2$ and $3$ Fourier components due to a large applied pulse with $m = 3$ azimuthal symmetry. The beat-wave decay instability causes the decay of the $m = 3$ mode and growth of the $m = 2$ mode. . . . .	129
7.4	Images of the total density at times $2.47t_{cr}$ , $6.92t_{cr}$ , $11.4t_{cr}$ , $15.8t_{cr}$ , $20.3t_{cr}$ , and $24.7t_{cr}$ , after excitation from a large pulse with $m = 3$ azimuthal symmetry. Due to beat-wave resonance damping, the $m = 3$ mode decays into an $m = 2$ mode. . . . .	130
7.5	Plot of the envelope of the perturbed electric field at the wall for the $m = 3$ and $m = 2$ mode versus time on a semilog scale. . . . .	131
7.6	Estimated growth rates $\gamma_2$ for daughter mode $m = 2$ normalized to the central rotation time versus normalized amplitude $A_3$ of parent mode $m = 3$ . . . . .	133
7.7	Plot of the experimental and computational growth rates for the $m = 2$ daughter mode versus parent mode $m = 3$ amplitude. . . . .	134

## List of Tables

1.1	Typical physical parameters for the Caltech Pure Electron Plasma Experiment. . . . .	6
2.1	Description of the normalized variables used in the numerical calculations. . . . .	18
4.1	Decay Rates for Various Profiles. . . . .	56
4.2	Comparison with Briggs decay rate for various profiles. For density profiles which deviate strongly from a step function, the Briggs decay formula is not very accurate. . . . .	58
6.1	Echo amplitude versus applied pulse 1 and pulse 2 amplitude. Pulse 1 is a one cycle pulse with $m_1 = 2$ symmetry and is applied at time $t = 0$ . Pulse 2 is a one cycle pulse that has $m_2 = 4$ symmetry and is applied at time $\tau = 25t_{cr}$ . The echo has $m_3 = 2$ symmetry and occurs at time $t = 50t_{cr}$ . The echo amplitude is given as a percentage of the unperturbed electric field at the wall. . . . .	108
6.2	Echo amplitude as a function of interpulse spacing. A one cycle pulse with $m_1 = 2$ symmetry and amplitude $1.0 \times 10^{-3}\phi_0$ is applied at time $t = 0$ . A second one cycle pulse with $m_2 = 4$ symmetry and amplitude $2.0 \times 10^{-3}\phi_0$ is applied at time $t = \tau$ . The echo amplitude is measured as a percentage of the unperturbed electric field at the wall. . . . .	113
7.1	Growth rate of the $m = 2$ mode as a function of $m = 3$ mode initial amplitude. . . . .	132

# Chapter 1 Introduction

## 1.1 Overview

This thesis presents results obtained using a new computational tool for studying a cylindrical pure electron plasma. Previous research has studied these plasmas using linear methods to describe the evolution of small perturbations of the steady-state density and electric potential. This newly developed tool numerically solves the full nonlinear two-dimensional (2-D) fluid equations in a cylindrical geometry. The nonlinear code allows the exploration of many phenomena that have been observed experimentally in these plasmas. Most of the experimentally observed phenomena are of large amplitude and therefore follow nonlinear dynamics. The previous codes based on the linearized equations can not reproduce these high amplitude phenomena.

To test the nonlinear fluid code, the plasma response was studied for small amplitude perturbations and compared with results from the linearized theory. For small amplitude perturbations, the results from the nonlinear fluid code were found to agree with the results from linearized calculations. The perturbed electric field at the wall was found to decay exponentially in time. This decay is due to a process where density perturbations at different radial layers undergo shear, so that the total contribution to the electric field at the wall phase mixes away.

At higher amplitudes, a modulation of the decay envelope occurs. This modulation has been observed experimentally and is qualitatively reproduced by the fluid code. The modulation is caused by the nonlinear trapping of fluid elements within the excited wave. The trapped fluid elements can be observed in images of the perturbed density that are produced by the nonlinear fluid code.

For two applied pulses that are separated in time, a third echo response is observed which occurs after the responses to the two applied pulses have decayed away. Echoes have been observed experimentally in neutral plasmas, but have not yet been observed

experimentally in a pure electron plasma.

At very high amplitudes, a nonlinear decay instability can occur. A high amplitude wave can decay into a wave with a lower azimuthal symmetry mode number due to an interaction at the beat frequency between these two waves. The beat-wave decay instability has been observed experimentally, and is also found to occur in computations using the 2-D nonlinear fluid code.

The 2-D cylindrical nonlinear fluid code is capable of reproducing a wide range of non-neutral plasma phenomena. It is expected that this nonlinear fluid code will be an important new tool for future research on non-neutral plasmas. This research can also be applied to other single species plasmas such as ion, positron, and antiproton plasmas, and also to ordinary fluids, since the 2-D equations describing a non-neutral plasma have the same form as the 2-D Euler equations for an inviscid fluid.

## 1.2 Background

Plasma is common throughout the universe, comprising more than 99% of the luminescent matter within it. On Earth, plasma may be found in neon signs or in laboratory experiments attempting to harness fusion energy from a confined plasma. These plasmas are neutral in total electrical charge. Non-neutral plasmas can also exist, usually comprised of a single species of charged particles; e.g., only electrons, ions, positrons, or antiprotons.

Non-neutral plasmas have numerous applications. Non-neutral plasmas are similar to the beams in microwave devices. Non-neutral plasma traps allow antiprotons produced in a collider to be transported to experiments located a large distance away [1][2]. Such a trap may eventually hold antimatter fuel for an extended space flight. The National Institute of Standards and Technology is pursuing research directed at using a non-neutral plasma to produce a clock that is more precise than the atomic clocks of today [3]. Another research effort is attempting to obtain fusion in a non-neutral plasma [4]. These applications, as well as unforeseen future applications, will benefit from a better understanding of the physics of non-neutral plasmas.

The history of pure electron plasmas begins with work on magnetized electron beams. Brillouin [5] first noticed that an electron beam could be focused with a magnetic field, where the repulsive force from the space charge of the electrons could be balanced by a Lorentz force due to the electrons passing through a magnetic field. Further research by Webster [6] found a magnetically focused hollow beam to be unstable. The hollow beam instability was attributed to shear in the azimuthal electron flow and named the slipping stream instability [7], which later became known as the diocotron instability [8].

Research performed by Levy [9] found that an analogy existed between the approximate equations describing a magnetized electron beam and the equations for 2-D incompressible inviscid fluid flow. Further research by Briggs, Daugherty, and Levy [10] predicted collisionless damping of wave perturbations for plasmas with density profiles that are monotonically decreasing in radius. This damping was found to be analogous to Landau damping in neutral plasmas [11].

Malmberg, deGrassie [12], and Driscoll developed the cylindrical Penning trap to confine a non-neutral plasma and study the basic physics of these plasmas. Many results have come from their research, including experimental results for 2-D vortex dynamics [13]. They have shown that the 2-D drift-Poisson equations suffice to describe a variety of phenomena in non-neutral plasmas, and the 2-D drift-Poisson equations will be used in this thesis. Theoretical work using the linearized 2-D drift-Poisson equations has been performed by Pillai [14], Corngold [15], and Spencer and Rasband [16]. Recent research on non-neutral plasmas has been summarized in two AIP Conference Proceedings [17][18].

The pure electron plasma laboratory at the California Institute of Technology is actively studying the physics of non-neutral plasmas with both experimental and computational efforts. Those experimental results relevant to this thesis will be summarized below, after explaining more clearly the geometrical configuration of a confined pure electron plasma in a cylindrical Penning trap. The results from the experiment motivated the computational research described in this thesis.

## 1.3 Pure Electron Plasma Geometry

### 1.3.1 Plasma Confinement

Pure electron plasmas are typically confined in a cylindrical Penning trap [12]. A schematic diagram of this trap is shown in Figure 1.1(a). The plasma is confined axially by electrodes biased to a sufficiently negative electric potential. The plasma is confined radially by a uniform externally applied axial magnetic field. In this configuration, there is a radial electric field due to the space charge of the electrons. Because the electrons are in an externally applied uniform magnetic field, they undergo cyclotron motion.

This thesis will focus on the low frequency phenomena related to rotation of the plasma. The plasma rotation frequency is much smaller than the cyclotron frequency for these plasmas. The cyclotron orbits of the electrons are not important, and the plasma will be discussed in the guiding center drift approximation.

The radial electric field causes an azimuthal  $\vec{E} \times \vec{B}$  drift in the motion. The azimuthal drift occurs at every radius, and thus the plasma rotates. The rotational angular velocity is not necessarily the same at every radius, so the flow of electrons may be sheared. With the flow of electrons in the azimuthal direction, the electrons are radially confined by the external magnetic field. The radial space charge repulsion force is balanced by the inward Lorentz  $\vec{v} \times \vec{B}$  force due to the plasma rotating in this uniform magnetic field.

### 1.3.2 Trap Operation

The procedure for operating the cylindrical Penning trap is as follows. A uniform external magnetic field in the axial direction surrounds the trap. Electrons are emitted from a hot filament and injected into the trap. The dump electrode is biased negatively to prevent electrons escaping from that end of the trap. After the trap is filled with electrons, the inject electrode is biased negatively and the electrons can not escape. During the confinement time, experiments are performed on the plasma.

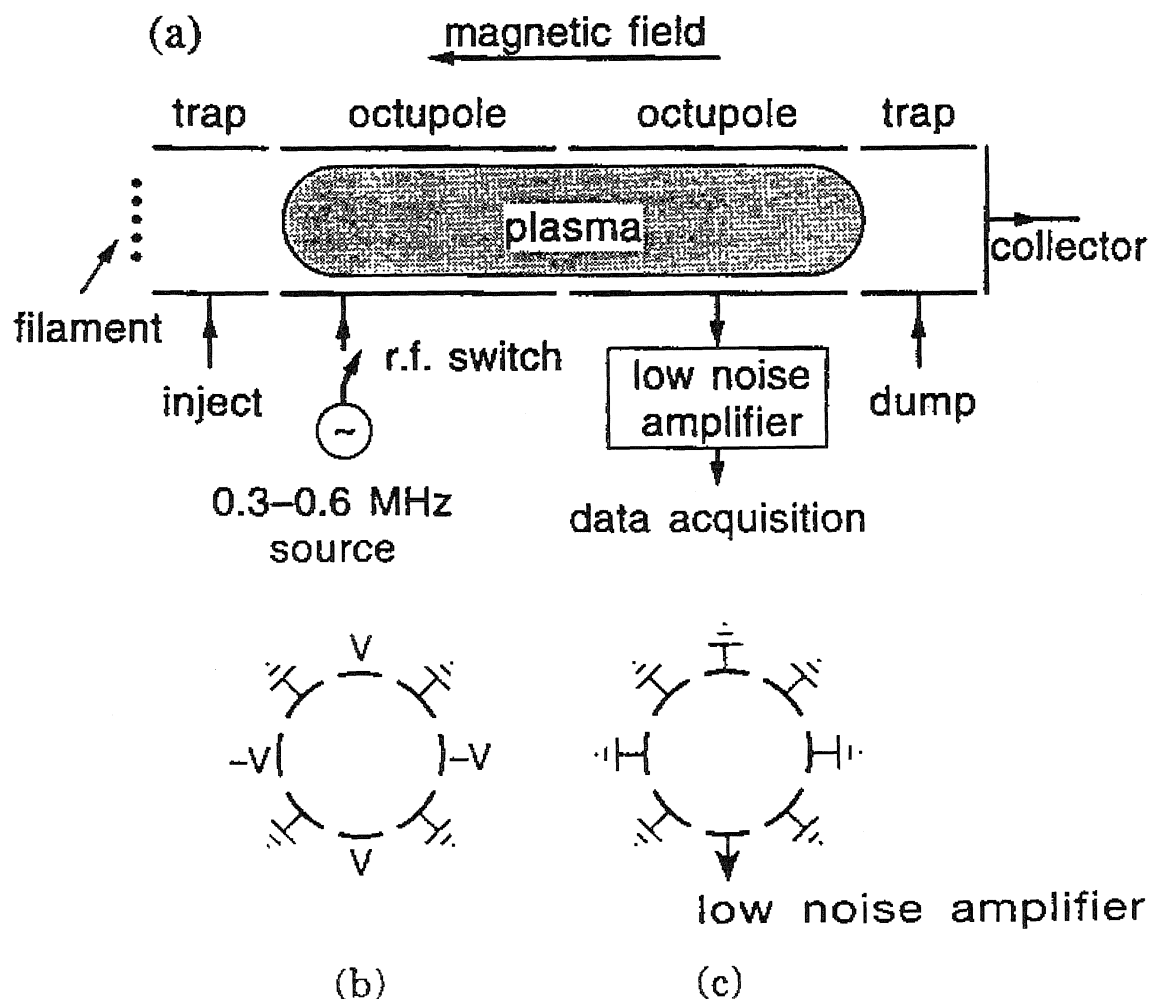


Figure 1.1: (a) Schematic diagram of a cylindrical Penning trap. (b) Diagram of the first sectored electrode structure in a configuration to produce a perturbation with  $m = 2$  symmetry. (c) Diagram of the second sectored electrode in a configuration to receive the response of the plasma at the wall.

Parameter	Value
Magnetic Field	50 Gauss
Central Electron Density	$\sim 1 \times 10^6 \text{ cm}^{-3}$
Electron Temperature	2 eV
Trap Radius	2.5 cm
Trap Length	40 cm
Cyclotron Frequency	140 MHz
Central Plasma Frequency	$\sim 9 \text{ MHz}$
Wall Rotation Frequency	$\sim 0.15 \text{ MHz}$
$m = 2$ Diocotron Frequency	$\sim 0.5 \text{ MHz}$
Axial Bounce Frequency	1 MHz
Larmor Radius	1 mm
Debye Length	1 cm

Table 1.1: Typical physical parameters for the Caltech Pure Electron Plasma Experiment.

Finally, the dump electrode is grounded, and the electrons are emptied from the trap. The experiment is repeated periodically in an inject, confine, and dump cycle.

The plasma is surrounded by a conducting cylindrical wall, which in the Caltech device is divided into two regions containing eight sectors each. A diagram of the sectored electrodes is shown in Figure 1.1(b) and (c). While the plasma is confined, voltages can be applied to the first set of wall sectors to excite perturbations in the plasma. Figure 1.1(b) demonstrates the sector configuration to excite a perturbation in the plasma with  $m = 2$  azimuthal symmetry. As the plasma rotates, perturbations in the plasma rotating past the second set of wall sectors cause an oscillating perturbed electric field at these sectors. This signal is then amplified and digitized, as shown in Figure 1.1(c). Sensing the oscillating perturbed electric field at the wall is the primary diagnostic measurement for the Pure Electron Plasma Experiment at Caltech.

### 1.3.3 Parameters in the Caltech Pure Electron Plasma Experiment

Physical parameters for the Caltech Pure Electron Plasma Experiment are summarized in table 1.1. This table is based on quantities measured in the experiment [19].

This thesis will focus on the low frequency diocotron modes that are near the average plasma rotation frequency. The  $m = 2$  diocotron frequency of 500 kHz corresponds to a resonant layer of plasma with a rotation frequency of 250 kHz.

This diocotron frequency is less than the plasma frequency, and much less than the cyclotron frequency, since the cyclotron frequency is much greater than the plasma frequency for this pure electron plasma. The cyclotron frequency being greater than the diocotron frequency justifies the approximation that inertial effects may be ignored, and the average electron velocity is given by  $\vec{E} \times \vec{B}$  drift. The plasma model will be discussed in more detail in Chapter 2.

Additionally, the axial bounce frequency is greater than the diocotron frequency, and for many phenomena the plasma may be treated as two-dimensional.

This is the basic geometry for a cylindrical pure electron plasma. The next section will describe some previous research performed on the Caltech Pure Electron Plasma Experiment, which motivated much of the effort in this thesis.

## 1.4 Previous Work at Caltech

The Caltech Pure Electron Plasma Experiment described above was used to study the response of the plasma to an externally applied sinusoidal burst. The experiment performed by N. Sateesh Pillai [14] found that for a small amplitude applied pulse, the oscillating electric field of the plasma at the wall decayed exponentially, experimentally verifying the exponential decay results of Briggs, Daugherty, and Levy [10]. For larger pulses, a modulation of the decay envelope was observed. These results are summarized in figure 1.2 which shows the envelope of the perturbed electric field at the wall versus time on a semilog scale.

Linearized fluid theory, reviewed in Chapter 2, was used to explain the exponential damping of the electric field at the wall for small applied pulses [14]. The damping is due to a collisionless phase mixing process [10]. The decay rates for power law density profiles has been studied analytically by Corngold [15]. The modulation of the decay envelope for larger pulses was attributed to trapping of a small fraction of

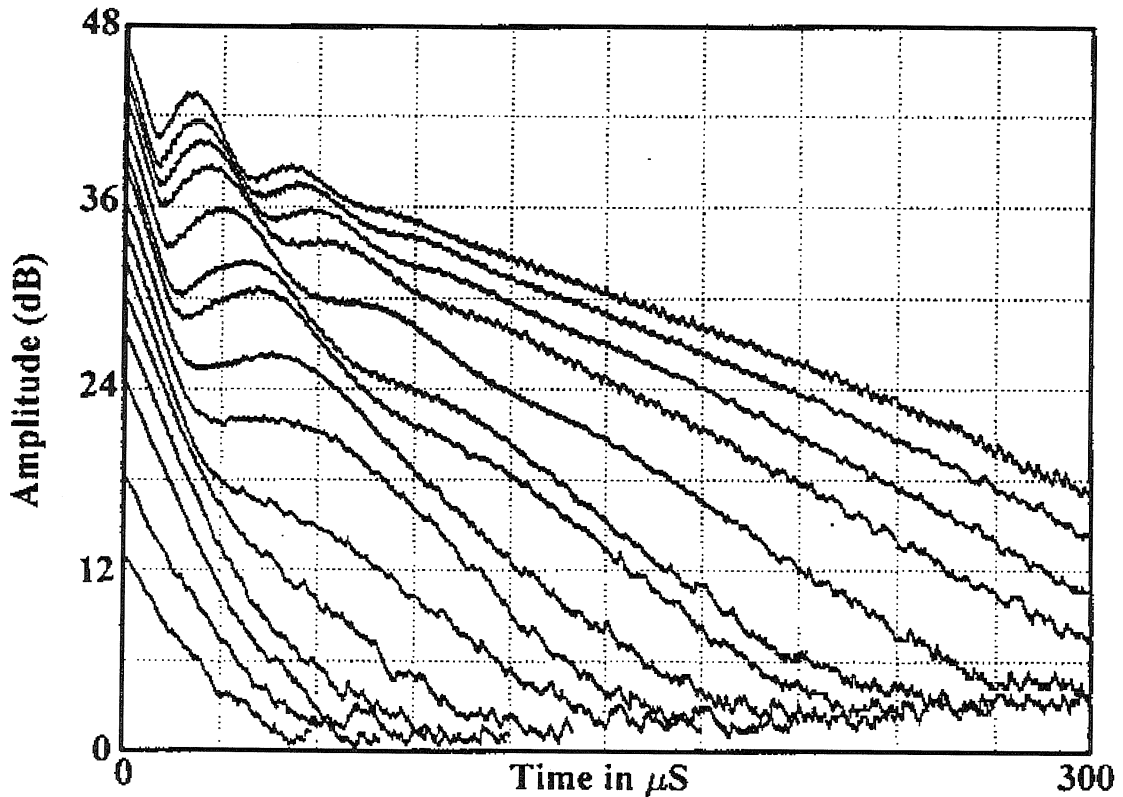


Figure 1.2: Plot of the envelope of the perturbed electric field at the wall versus time on a semilog scale for the experimental data collected by N. Sateesh Pillai. The applied  $m = 2$  excitation voltage ranges from 10 mV for the lowest amplitude pulse, to 1000 mV for the highest amplitude trace. The vertical scale is calibrated in dB.

plasma by the excited wave.

The experiment did not permit direct measurement of plasma density perturbations. Therefore the hypothesis of trapped plasma at higher amplitudes could not be verified by direct observation. This motivated my use of computational methods to better understand these phenomena. Computation allows access to quantities which can not be diagnosed in the Caltech experiment, and provides verification of the nonlinear fluid model used in the computation to describe the plasma.

## 1.5 Thesis Outline

This thesis is based on the results of a nonlinear 2-D cylindrical fluid code. The fluid code is used to study the response of a pure electron plasma to one or more externally applied pulses. First the plasma model will be discussed in Chapter 2, followed by a discussion of the numerical techniques applied to the model equations in Chapter 3. Chapter 4 and Chapter 5 will describe the results from the fluid code for initial plasma conditions that have been studied in previous experiments at Caltech. Chapter 4 examines the plasma response for a small amplitude applied pulse and Chapter 5 examines the response for larger pulses. Chapter 6 will discuss two applied pulses interacting to produce an echo, a result seen in the fluid code that has not yet been observed experimentally. Chapter 7 will discuss preliminary research on a decay instability that occurs at very high amplitudes. This decay instability has been observed experimentally and also occurs in computations using the nonlinear fluid code. Chapter 8 will present a summary of results and discuss further research opportunities.

Chapter 2 will discuss the fluid model used to describe the pure electron plasma. Under certain approximations, a pure electron plasma can be modeled by the equations for an incompressible and inviscid fluid. The dynamics of the plasma are governed by Poisson's equation, the continuity equation, and the equation for  $\vec{E} \times \vec{B}$  drift. These equations are then linearized around steady-state quantities to obtain a more tractable equation for the perturbed quantities, valid when the perturbations are small. A set of normalized variables will be introduced, that will be used throughout the remainder of the thesis.

Chapter 3 will discuss the application of numerical techniques to the fluid model. A nonlinear 2-D cylindrical fluid code will be presented. Numerical solution of Poisson's equation and the time derivative of the density will be discussed, followed by the method for advancing the density in time. The diagnostics in the code will be mentioned, and errors in the fluid code will be discussed. The nonlinear 2-D cylindrical fluid code is the primary tool used to obtain the results presented in this thesis. A

model based on the linearized equations presented in Chapter 2 will then be discussed.

Chapters 4, 5, 6, and 7 contain results from the nonlinear fluid code. Chapter 4 describes the response of the plasma to a small amplitude applied pulse. The response in the electric field at the wall is found to decay exponentially in time. This is consistent with experimental results for small applied pulses. The decay is due to a collisionless phase mixing process where density perturbations at different radii convect at different angular velocities. This mixing process is clearly illustrated by successive images of the perturbed density. An approximate analytical solution to the linearized fluid equations is then presented, further illustrating the plasma dynamics.

Chapter 5 discusses higher amplitude pulses which cause a modulation of the decay envelope due to trapping of fluid elements within the excited wave. The experimental results showing an exponential decay at lower amplitudes and the modulation of the decay envelope at higher amplitudes are qualitatively reproduced using the nonlinear fluid code. Images of the perturbed density show regions of plasma trapped by the wave, causing the modulation of the decay envelope at higher amplitudes. Thus the explanation of modulation of the decay as being due to trapping is confirmed. Applying the external pulse slowly excites a wave that has a greatly reduced decay rate with no apparent modulation in the decay. This suggests a similarity to BGK modes in neutral plasmas [20].

Chapter 6 describes the phenomena of echoes which is predicted to occur in a pure electron plasma [21]. An echo can occur when a single pulse that decays in time is followed by a second pulse of higher azimuthal symmetry that also decays in time. These two perturbations then undergo a nonlinear interaction to generate a third echo response at a later time. An approximate theoretical description of echoes is first presented, followed by the results from the fluid code. The time of the echo and its amplitude dependence are studied, as well as higher order effects for larger pulses. These effects have not yet been observed experimentally in a non-neutral plasma.

Chapter 7 discusses the effects of very large pulses on the plasma. Such large perturbations are found to be subject to a “decay instability.” A large perturbation with  $m = 3$  azimuthal symmetry is found to decay into a perturbation with  $m = 2$

azimuthal symmetry due to an interaction with the plasma at the beat frequency of the  $m = 3$  and  $m = 2$  waves. The  $m = 2$  growth rate is systematically studied as a function of  $m = 3$  mode amplitude. The beat-wave resonance damping results are compared to the experimental results of Mitchell and Driscoll [22].

Chapter 8 presents a summary of the results of this thesis. The summary is followed by a discussion of questions which remain for future research to answer.

# Chapter 2 The Fluid Model

## 2.1 Introduction

The geometry of the experimental setup for creating and trapping a pure electron plasma was previously shown in Chapter 1. This chapter presents a mathematical model for a pure electron plasma which will be used in subsequent chapters.

A pure electron plasma in the discussed geometry and under certain approximations can be described as a cylindrical column of rotating fluid surrounded by a conducting cylinder. A strong axial magnetic field confines the plasma radially, while electrostatic trapping end electrodes confines the plasma axially, as previously discussed in Chapter 1.

The first section will discuss the approximations made in the fluid equation model. The plasma may be taken as electrostatic, two-dimensional, and with zero pressure gradient.

After the discussion of approximations, the fluid model will be discussed. Under the approximations, the plasma may be treated as an incompressible, inviscid 2-D fluid. The 2-D nonlinear fluid equations which describe a non-neutral plasma will be presented. These equations will be used to model a pure electron plasma, and are analogous to the Euler inviscid fluid equations. The presented set of equations are the basis for the Nonlinear Fluid Code presented in Chapter 3.

A normalized set of variables will be introduced. These normalized variables will absorb such quantities as the radius of the wall, magnitude of the magnetic field, charge of the electron and the permittivity of free space. The use of normalized variables simplifies the equations, and these new variables will be used throughout the thesis.

The nonlinear 2-D fluid equations can be linearized for small perturbations around steady-state quantities. Such a linearization reduces the 2-D fluid equations to a

single equation for the perturbed electric potential. This equation is valid for small amplitude perturbations to the plasma, and forms the basis of the Linearized Fluid Code presented in the next chapter.

## 2.2 Model Assumptions and Approximations

### 2.2.1 Approximations to Maxwell's Equations

The fields due to the plasma are taken to be entirely electrostatic. Currents produced by the motion of electrons are assumed to be small, and the induced magnetic fields due to these currents are taken as negligible compared to the strong external magnetic field. The magnetic force between moving electrons is taken to be small compared to the electrostatic force. Electric fields induced inductively by time dependent currents in the plasma are negligible compared to the electrostatic space charge fields of the plasma. Additionally, changes in the electric field are assumed to propagate much faster than any motion of the plasma.

The surrounding cylinder is taken to be perfectly conducting, so that no dissipation from resistance in the wall will be considered. This corresponds to a boundary condition for the electric potential at the wall. The wall will be held at zero electric potential, except during application of an external pulse of voltage along wall sectors to induce plasma perturbations.

Under these approximations, Maxwell's Equations reduce to

$$\begin{aligned}\vec{\nabla} \cdot \vec{E} &= -\frac{e}{\epsilon_0} n \\ \vec{\nabla} \cdot \vec{B} &= 0 \\ \vec{\nabla} \times \vec{E} &= 0 \\ \vec{\nabla} \times \vec{B} &= 0\end{aligned}$$

for the electric field  $\vec{E}$ , and the magnetic field  $\vec{B}$ , with  $n$  representing the electron

density. The quantity  $e$  is the magnitude of the electron charge, and  $\epsilon_0$  is the permittivity of free space. The electric field may be written as the gradient of an electric potential

$$\vec{E} = -\vec{\nabla}\phi$$

so that the electric potential is given by Poisson's equation

$$\nabla^2\phi = \frac{e}{\epsilon_0}n$$

with the boundary condition at the wall discussed above. The magnetic field is a constant  $\vec{B}$  in the  $\hat{z}$ -direction.

### 2.2.2 Approximation of a Two-dimensional Plasma

A large number of experimental results are essentially 2-D in nature, and this thesis will focus only on 2-D phenomena. A possible reason for the 2-D behavior of these plasmas can be argued from the axial motion of the electrons along the magnetic field lines. The electrons rapidly bounce back and forth between the electrostatic trapping electrodes at each end of the cylinder, with a bounce frequency higher than the plasma rotation frequency, effectively averaging over any  $\hat{z}$ -direction asymmetries.

For the rest of this thesis, only two-dimensional effects will be considered. The  $\hat{z}$ -direction will be ignored, treating the plasma column as infinite in length, and only components in  $r$  and  $\theta$  will be considered.

### 2.2.3 Approximation of Zero Pressure Gradient

The electron density is assumed to have a monotonically decreasing radial distribution with the density highest at the center and approaching zero near the wall. Related to the radial density gradient in a warm plasma is a radial pressure gradient which will cause a diamagnetic drift. Previous research [13] has found that the diamagnetic drifts and thermal effects appear to be of minimal importance in describing phenomena

observed in non-neutral plasmas. Accordingly, all thermal effects will be ignored in this thesis, and the plasma will be taken to have a zero pressure gradient.

### 2.2.4 Drift Approximation

This section discusses the drift approximation. Neglecting viscosity and thermal effects, the equation for the fluid velocity is given by

$$nm_e \frac{D \vec{v}}{Dt} = -ne(\vec{E} + \vec{v} \times \vec{B}) \quad (2.1)$$

where  $m_e$  is the mass of the electron,  $\vec{v}(r, \theta, t)$  is the fluid velocity, and  $\frac{D}{Dt}$  denotes the convective derivative. This equation may be rewritten as

$$\frac{D \vec{v}}{Dt} = -\frac{e}{m_e} \vec{E} - \omega_c \vec{v} \times \hat{z}$$

where the cyclotron frequency  $\omega_c = \frac{eB}{m_e}$ , and the magnetic field  $\vec{B} = B\hat{z}$ . For low density electron plasmas in a strong magnetic field, the electric field  $\vec{E}$  from the space charge of the plasma, and the  $\vec{v} \times \vec{B}$  term are large compared to the inertial  $\frac{D \vec{v}}{Dt}$  term. The low frequency modes studied in this thesis are of the same order as the fluid angular rotation frequency  $\omega_0$ , which is assumed to be much less than the cyclotron frequency. The inertial  $\frac{D \vec{v}}{Dt}$  term is of the order  $\omega_0 v$ , which is therefore small compared to  $\omega_c v$  in the magnetic term, and can be neglected. By neglecting the inertial term in equation 2.1, the fluid velocity is given by

$$\vec{v} = \frac{\vec{E} \times \vec{B}}{|\vec{B}|^2} \quad (2.2)$$

which is the standard expression for the velocity due to  $\vec{E} \times \vec{B}$  drift.

Applying equation 2.2 to a cylindrical pure electron plasma, the strong radial electric field causes a drift velocity in the  $\hat{\theta}$ -direction, with central rotational angular frequency  $\omega_0(0) = \frac{\omega_p^2(0)}{2\omega_c}$  where  $\omega_p^2 = \frac{ne^2}{\epsilon_0 m_e}$  is the plasma frequency (A discussion of the steady-state angular velocity  $\omega_0(r)$  will be left to the next section). Therefore the

inertial term in equation 2.1 is of order  $\frac{\omega_p^2}{\omega_c^2}$  compared to the magnetic term. If the plasma frequency is much smaller than the cyclotron frequency; i.e.,  $\frac{\omega_p^2}{\omega_c^2} \ll 1$ , then at every radius the rotational angular frequency  $\omega_0$  is small compared to the cyclotron frequency, satisfying the above assumptions. In fact, the criterion  $\frac{\omega_p^2}{\omega_c^2} \ll 1$  is well satisfied for a low density electron plasma in a strong magnetic field, as seen in table 1.1 for the Caltech Pure Electron Plasma Experiment.

## 2.3 Steady-State Angular Velocity

This section describes the steady-state angular velocity for an unperturbed pure electron plasma. The angular velocity of these plasmas is a very important quantity responsible for many plasma phenomena. For a nonuniform density, the angular velocity is sheared. The shear in the angular velocity is responsible for the collisionless damping described in Chapter 4.

For a confined, unperturbed cylindrical pure electron plasma, the electron density  $n(r)$  is only a function of the radius. The radial electric field is given by

$$E_r(r) = -\frac{e}{\varepsilon_0} \frac{1}{r} \int_0^r r' n(r') dr', \quad (2.3)$$

and the plasma motion is dominated by  $\vec{E} \times \vec{B}$  drift. Inserting equation 2.3 into 2.2, the azimuthal velocity is given by

$$v_\theta(r) = \frac{e}{\varepsilon_0} \frac{1}{rB} \int_0^r r' n(r') dr'$$

where  $B$  is the magnitude of the uniform magnetic field that is in the  $\hat{z}$ -direction. The angular rotation frequency  $\omega_0(r) = v_\theta(r)/r$  can be written as

$$\omega_0(r) = \frac{e}{\varepsilon_0} \frac{1}{r^2 B} \int_0^r r' n(r') dr'. \quad (2.4)$$

For a plasma with uniform electron density that is independent of radius, equation 2.4 can be integrated to give an angular rotation frequency which is independent of

radius. Thus, in this special case, the plasma rotates as a rigid body with angular frequency

$$\omega_0 = \frac{1}{2} \frac{e}{\varepsilon_0} \frac{n}{B}.$$

On the other hand, for electron density profiles that do vary with radius, the angular rotation frequency becomes dependent on the radius and can be calculated by equation 2.4. This thesis will focus on non-uniform density profiles that decrease monotonically with radius. For these density profiles, the plasma flow is sheared. The angular velocity at the origin is given by

$$\omega_0(0) = \frac{1}{2} \frac{e}{\varepsilon_0} \frac{n(0)}{B} = \frac{\omega_p^2(0)}{2\omega_c}.$$

## 2.4 Nonlinear Model

The plasma is described in two dimensions by the electron density  $n(r, \theta, t)$ , the electrostatic potential  $\phi(r, \theta, t)$ , and the fluid velocity  $\vec{v}(r, \theta, t)$ . The  $\hat{z}$  dependence is ignored. Under the assumptions of the previous section, the instantaneous relationship between the density and electric potential is given by Poisson's equation

$$\nabla^2 \phi(r, \theta, t) = \frac{e}{\varepsilon_0} n(r, \theta, t) \quad (2.5)$$

where  $e$  is the magnitude of the electron charge, and  $\varepsilon_0$  is the permittivity of free space.

Under the approximations discussed in the previous section, the fluid velocity is given by

$$\vec{v} = \frac{-\vec{\nabla} \phi \times \vec{B}}{|\vec{B}|^2}. \quad (2.6)$$

The final equation for this system is the continuity equation for 2-D inviscid fluids, written as

Variable Name	Normalized Variable Symbol	Dimensionless Variable
time	$t$	$\frac{en_0(0)}{\epsilon_0 B} t$
radius	$r$	$\frac{r}{r_w}$
electron density	$n$	$\frac{n}{n_0(0)}$
electric potential	$\phi$	$\frac{\epsilon_0}{en_0(0)r_w^2} \phi$
electric field	$\vec{E}$	$\frac{\epsilon_0}{en_0(0)r_w} \vec{E}$

Table 2.1: Description of the normalized variables used in the numerical calculations.

$$\frac{\partial n}{\partial t} + \nabla \cdot (n \vec{v}) = 0.$$

Because the drift form of the velocity is divergence free, the fluid is incompressible, and the continuity equation reduces to

$$\frac{\partial n}{\partial t} + \vec{v} \cdot \vec{\nabla} n = 0. \quad (2.7)$$

Equations 2.5, 2.6, and 2.7 describe the full nonlinear time evolution of the plasma under the assumptions of the previous section. These equations are isomorphic to the Euler equations for incompressible, inviscid fluids [9][10], where the vorticity is analogous to the electron density, and the electric potential is analogous to the stream function.

## 2.5 Normalized Variables

The three equations governing the full nonlinear dynamics of the plasma are Poisson's equation 2.5, the incompressible fluid continuity equation 2.7, and the drift equation 2.6. To simplify the calculations and to make the results of the fluid code easily scalable, a normalized set of variables will be introduced which eliminate the physical constants from the equations. The definition of these new normalized variables are summarized in table 2.1. The quantity  $r_w$  is the wall radius,  $B$  is the magnitude of the magnetic field, and  $n_0(0)$  is the central electron density.

Using these dimensionless variables, the fluid equations 2.5, 2.6 and 2.7 reduce to

$$\nabla^2 \phi = n \quad (2.8)$$

$$\frac{\partial n}{\partial t} = -\vec{v} \cdot \vec{\nabla} n \quad (2.9)$$

$$\vec{v} = -\vec{\nabla} \phi \times \hat{z}. \quad (2.10)$$

## 2.6 Linearized Model

It is useful to analyze the case in which the plasma deviates slightly from a cylindrical equilibrium [10][13][14][15][16]. Separating the electron density, electric potential, and fluid velocity into steady-state quantities and perturbed quantities gives

$$n(r, \theta, t) = n_0(r) + n_1(r, \theta, t)$$

$$\phi(r, \theta, t) = \phi_0(r) + \phi_1(r, \theta, t)$$

$$\vec{v}(r, \theta, t) = \vec{v}_0(r) + \vec{v}_1(r, \theta, t)$$

where the subscript 0 indicates large steady-state zero order quantities and the subscript 1 represents perturbed quantities that are first order in amplitude. In a later chapter describing echoes, second order quantities will be considered to produce a source term. In this discussion, quantities higher than first order are neglected.

Poisson's equation is linear, so it can be separated into unperturbed and perturbed components

$$\nabla^2 \phi_0 = n_0$$

and

$$\nabla^2 \phi_1 = n_1. \quad (2.11)$$

For the drift equation 2.10, the magnetic field is in the  $\hat{z}$  direction and  $\vec{\nabla}\phi_0$  is in the  $\hat{r}$  direction, so the only unperturbed velocity component is in the  $\hat{\theta}$  direction, and is given by

$$[v_0(r)]_\theta = \frac{\partial \phi_0}{\partial r}.$$

The steady-state angular velocity is given by

$$\omega_0(r) = \frac{1}{r} v_{0\theta} = \frac{1}{r} \frac{\partial \phi_0}{\partial r}.$$

The continuity equation is simply

$$\frac{\partial n_0}{\partial t} = 0$$

as this is a steady-state quantity, and for the perturbed quantities

$$\frac{\partial n_1}{\partial t} + (\vec{v}_0 + \vec{v}_1) \cdot \vec{\nabla} (n_0 + n_1) = 0.$$

Neglecting the higher order term  $\vec{v}_1 \cdot \vec{\nabla} n_1$ , the perturbed continuity equation becomes

$$\frac{\partial n_1}{\partial t} + \vec{v}_0 \cdot \vec{\nabla} n_1 + \vec{v}_1 \cdot \vec{\nabla} n_0 = 0.$$

As only the  $\hat{\theta}$  component of  $\vec{v}_0$  and the  $\hat{r}$  component of  $\vec{\nabla} n_0$  is nonzero, the perturbed continuity equation reduces to

$$\frac{\partial n_1}{\partial t} + \frac{v_{0\theta}}{r} \frac{\partial n_1}{\partial \theta} + v_{1r} \frac{dn_0}{dr} = 0$$

where  $v_{1r} = -\frac{1}{r} \frac{\partial \phi_1}{\partial \theta}$ . The term  $v_{0\theta}/r$  is equal to the steady-state angular velocity

$\omega_0(r)$ . Making this substitution, the continuity equation for the perturbed quantities becomes

$$\frac{\partial n_1}{\partial t} + \omega_0(r) \frac{\partial n_1}{\partial \theta} + v_{1r} \frac{dn_0}{dr} = 0. \quad (2.12)$$

The next step is to assume an angular dependence of the perturbation. Complex exponentials will be used to represent this angular dependence. Since the perturbed density and perturbed potential are real quantities, it will be necessary eventually to either add the complex conjugate to the results, or to take the real part of the quantity to obtain real values. Taking an angular dependence of  $e^{im\theta}$  for the perturbed quantities,  $n_1(r, \theta, t) = n_{1,m}(r, t)e^{im\theta}$ ,  $\phi_1(r, \theta, t) = \phi_{1,m}(r, t)e^{im\theta}$  and  $[v_1(r, \theta, t)]_r = [v_{1,m}(r, t)]_r e^{im\theta}$  the continuity equation 2.12 for the perturbed quantities is

$$\frac{\partial n_{1,m}(r, t)}{\partial t} + im\omega_0(r)n_{1,m}(r, t) + [v_{1,m}(r, t)]_r \frac{dn_0(r)}{dr} = 0. \quad (2.13)$$

A Laplace transform is applied to the equation 2.13. The Laplace transform variable  $s = -i\omega$ , where  $\omega$  is complex and includes a small positive imaginary part. The variable  $s$  lies in the right hand plane, so  $\omega$  is in the upper half plane. The plasma is initially unperturbed, leading to the initial condition  $n_{1,m}(r, 0) = 0$ . The transformed equation may be solved for the transformed perturbed density with the solution

$$\tilde{n}_{1,m}(r, \omega) = \frac{m}{r(m\omega_0(r) - \omega)} \frac{dn_0(r)}{dr} \tilde{\phi}_{1,m}(r, \omega). \quad (2.14)$$

Using this form of the perturbed density, and substituting back into the perturbed form for Poisson's equation 2.11 gives the result

$$\frac{d^2 \tilde{\phi}_{1,m}(r, \omega)}{dr^2} + \frac{1}{r} \frac{d\tilde{\phi}_{1,m}(r, \omega)}{dr} - \left[ \frac{m^2}{r^2} + \frac{m}{r(m\omega_0(r) - \omega)} \frac{dn_0(r)}{dr} \right] \tilde{\phi}_{1,m}(r, \omega) = 0. \quad (2.15)$$

This is an ordinary linear differential equation that can be solved for the perturbed potential  $\tilde{\phi}_{1,m}(r, \omega)$ . The boundary condition at the origin is given by  $\tilde{\phi}_{1,m}(0, \omega) = 0$ ,

and the boundary condition at the wall is given by the Laplace transform of the wall potential. Once the solution for  $\tilde{\phi}_{1,m}(r, \omega)$  is found, the perturbed density is given by Poisson's equation or by equation 2.14. The time dependence of the perturbed density and perturbed potential is given by the inverse Laplace transform of  $\tilde{n}_{1,m}(r, \omega)$  and  $\tilde{\phi}_{1,m}(r, \omega)$ . This is the equation used in the linearized computation to obtain results for small amplitude applied pulses.

## 2.7 Summary

A pure electron plasma under certain approximations can be treated as an incompressible, inviscid fluid. Under these approximations, the equations of motion are given by Poisson's equation, the continuity equation, and the equation for  $\vec{E} \times \vec{B}$  drift. These equations can be linearized to obtain a single equation for the perturbed potential. A solution to this linearized equation should be valid for small amplitude applied pulses, where the resulting perturbed potential is much smaller than the unperturbed electric potential of the plasma.

These are the model equations used throughout this thesis. The next chapter will discuss the methods for applying numerical techniques to these equations.

# Chapter 3 Computational Methods

## 3.1 Introduction

The fluid model equations discussed in the last chapter are difficult to solve analytically for anything but the most trivial choices of plasma density and wall potential. However, Corngold has made substantial progress for certain power law density profiles [15]. In order to allow exploration of a variety of different nontrivial phenomena, computational methods were used to solve the 2-D fluid equations. Two different types of codes were developed to solve the equations, each applicable to a particular regime of plasma behavior.

The first code solves the full 2-D nonlinear fluid equations in cylindrical geometry. This code will be referred to as the *Nonlinear Fluid Code* throughout the remainder of this thesis. The Nonlinear Fluid Code presented here is a new tool for studying pure electron plasmas. The primary results of this thesis are based on results obtained from the Nonlinear Fluid Code which was written in Microsoft PowerFORTRAN.

The second code numerically integrates the ordinary differential equation resulting from the *linearized* fluid equations (equation 2.15) for infinitesimal perturbations in a single azimuthal symmetry eigenmode number and as a function of frequency. Throughout this thesis, the program which solves equation 2.15 will be referred to as the *Linearized Fluid Code*. This code was written in Microsoft Quickbasic. Similar codes to solve equation 2.15 have been used successfully to study pure electron plasmas [14][16].

Results from these two codes were compared for small amplitude perturbations. The results from the Nonlinear Fluid Code agree with the results from the Linearized Fluid Code. This provides evidence that the computational methods are valid, since each code uses a quite different method to solve the equations.

This chapter will first present a discussion of the various components of the Non-

linear Fluid Code. The density and potential are discretized on a cylindrical mesh, and numerical techniques are used to solve Poisson's equation and the nonlinear equation for the time derivative of the density. The density is then numerically integrated forward in time. The diagnostics from the nonlinear code are discussed, including the effects of accumulated errors.

The next section will describe the Linearized Fluid Code. This code numerically integrates equation 2.15 for 500 points in radius and 512 discrete frequencies, leading to a solution for the perturbed potential as a function of time.

## 3.2 Nonlinear Fluid Code

This section will describe the two-dimensional cylindrical fluid code used to obtain most of the results in this thesis. Originally this code was written in Cartesian coordinates by R. W. Gould and produced some useful results. However, it was found that the Cartesian code generated some numerical artifacts, caused by the Cartesian grid failing to properly represent the cylindrical symmetry of the problem. By rewriting the code in cylindrical geometry, these numerical artifacts were avoided. A grid resolution of 512 points in radius and 128 points in angle was used for most computations. For several computations, a grid resolution of 1024 points in radius and 256 points in angle was used, but this increases the necessary computation time by a factor of 8. This section will focus on the methods used in the cylindrical code. The specific numerical methods for solving each part of the system will be discussed, with the final section describing the diagnostic outputs of the code and numerical errors in the code.

The nonlinear fluid code has three main subroutines. These three subroutines solve Poisson's equation, calculate the time derivative of the density, and advance the density in time. Given a density input, the Poisson solver computes the electric potential. Given the density and electric potential, the density derivative routine computes the time derivative of the density. Given the density, time derivative of the density, and a time step, the time advance routine advances the density in time. For

computational stability, the density is advanced using a half-step, full-step leapfrog time integration method. The program logic is summarized in the flow chart diagram of figure 3.1. The details of the individual subroutines will be described in the next sections.

### 3.2.1 Poisson's Equation

The first equation to solve is Poisson's equation (equation 2.8). The following procedure is partially based on the method presented by Birdsall and Langdon [23]. Given a specific electron density distribution  $n(r, \theta)$ , this allows the calculation of the electric potential  $\phi(r, \theta)$  throughout the plasma, subject to the boundary conditions at the wall. In cylindrical coordinates, Poisson's equation is given by

$$\frac{\partial^2 \phi}{\partial r^2} + \frac{1}{r} \frac{\partial \phi}{\partial r} + \frac{1}{r^2} \frac{\partial^2 \phi}{\partial \theta^2} = n.$$

The electric potential is decomposed into two parts, the electric potential from the plasma,  $\phi_{plasma}$ , and the electric potential from the applied sectors in vacuum without the plasma,  $\phi_{applied}$ . The total potential is then just the sum of these two potentials,  $\phi = \phi_{plasma} + \phi_{applied}$ . This is done so that the details of the plasma potential can be observed without being hidden by the applied pulse potential. In this manner, the buildup of the plasma potential can be observed during the application of the applied pulse. The plasma potential  $\phi_{plasma}$  may be solved with the following procedure by setting the wall boundary conditions to zero, and the applied potential  $\phi_{applied}$  may also be solved with this method by using a density of zero, and only considering the boundary conditions at the wall. The applied potential is non-zero for only a short period of time to initiate a perturbation in the plasma.

To solve Poisson's equation, the first step is to represent the angular part of the variables as a Fourier series  $\phi(r, \theta) = \sum \phi_m(r) e^{im\theta}$  and  $n(r, \theta) = \sum n_m(r) e^{im\theta}$ , with each azimuthal symmetry eigenmode number represented by the variable  $m$ . The Poisson equation then becomes a set of equations, one for each  $m$  value given by

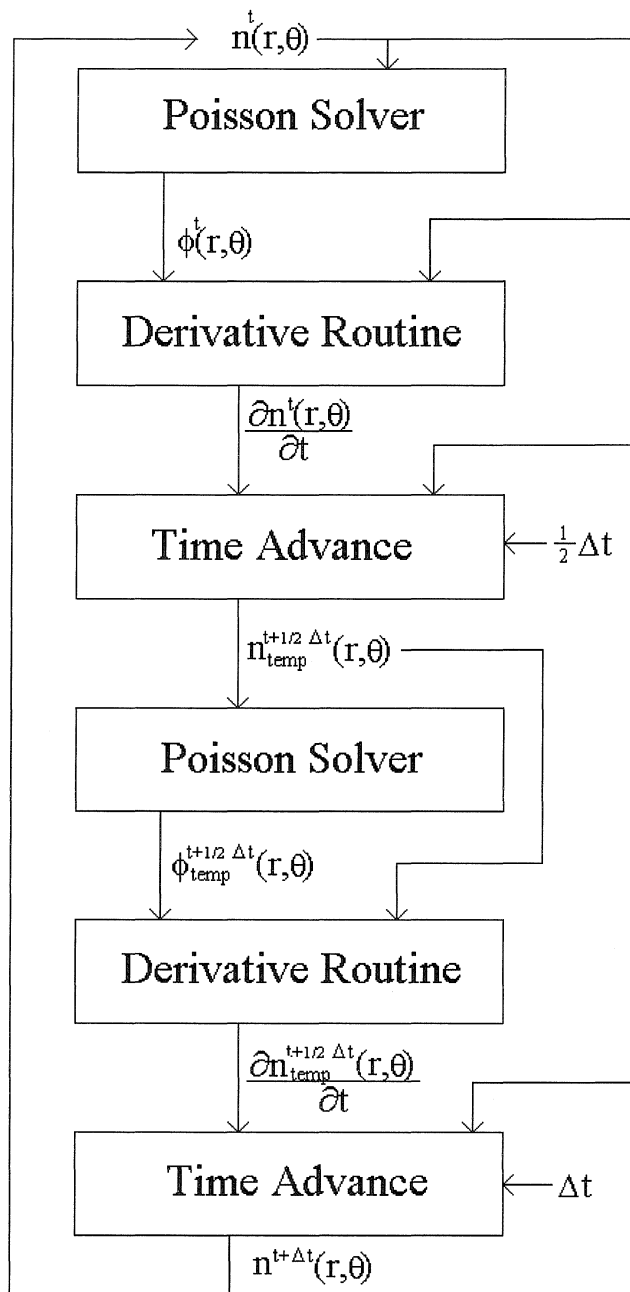


Figure 3.1: Flow chart describing the logic of the nonlinear fluid code. The superscript represents time, with the time step given by  $\Delta t$ . The subscript temp stands for temporary.

$$\frac{d^2\phi_m}{dr^2} + \frac{1}{r} \frac{d\phi_m}{dr} - \frac{m^2}{r^2} \phi_m = n_m$$

where  $\phi_m(r)$  and  $n_m(r)$  are the Fourier series coefficients for the electric potential and electron density, respectively.

The next step is to discretize the system in the radial direction, setting  $r_i = i\Delta r$  where  $\Delta r$  is the radial grid spacing and the subscript  $i$  represents the radial integer index for the discretized system. Applying second order finite difference methods the equation becomes

$$\frac{\phi_{i+1,m} - 2\phi_{i,m} + \phi_{i-1,m}}{(\Delta r)^2} + \frac{\phi_{i+1,m} - \phi_{i-1,m}}{2r_i(\Delta r)} - \frac{m^2}{r_i^2} \phi_{i,m} = n_{i,m}$$

which can be rewritten as

$$\left(\frac{1}{(\Delta r)^2} - \frac{1}{2r_i(\Delta r)}\right)\phi_{i-1,m} - \left(\frac{2}{(\Delta r)^2} + \frac{m^2}{r_i^2}\right)\phi_{i,m} + \left(\frac{1}{(\Delta r)^2} + \frac{1}{2r_i(\Delta r)}\right)\phi_{i+1,m} = n_{i,m}.$$

The index  $i$  has a range of 1 to  $N_i$ , where  $N_i$  is the total number of radial grid points. The origin at index  $i = 0$  is a boundary condition to be discussed below. This system is a set of linear algebraic equations, one for each index  $i$ , that can be solved by linear algebra matrix techniques. Specifically, the system can be rewritten in vector form as  $\vec{A}\vec{\phi} = \vec{n}$  where  $A$  is a tridiagonal matrix and  $\vec{\phi}$  and  $\vec{n}$  are vectors with index  $i$  ranging 1 to  $N_i - 1$ . The boundary conditions at the origin and at  $i = N_i$  have been included in  $n_{1,m}$  and  $n_{N_i,m}$ . A tridiagonal solve routine, IMSL library call DLSLTQ, was used to solve for each  $\phi_{i,m}$  for the given set of  $n_{i,m}$ . The set of  $n_{i,m}$  is found by performing a discrete Fourier transform in angle on the density  $n_{i,j}$ , where  $i$  is the index in radius and  $j$  is the index in angle.

For the plasma potential  $\phi_{plasma}$ , the boundary condition at the wall is zero for the electric potential due to the plasma since any potentials at the wall are contained in the applied potential. The boundary condition is satisfied by setting the Fourier coefficients  $\phi_{N_i,m} = 0$  for all  $m$  values. For the applied potential  $\phi_{applied}$ , the boundary

condition at the wall for the electric potential from applied voltages at the wall in vacuum are determined by Fourier analyzing the applied wall potential in angle  $\theta$  to obtain the Fourier coefficients  $\phi_{N_i,m}$ . Using this wall boundary condition, the vacuum potential is found by using a value of zero for the density, i.e.,  $n_{i,m} = 0$  for all  $i$  and  $m$ .

The boundary condition at the origin is simply given by  $\phi_{0,m} = 0$  for all  $|m| \geq 1$ , since a well behaved solution to Poisson's equation can not contain a finite angular component at the origin. However, the  $m = 0$  case must be treated separately, using a different boundary condition at the origin.

The origin boundary condition for the  $m = 0$  component can be understood by a simple application of Gauss' Law. For the plasma potential  $\phi_{plasma}$ , the origin  $m = 0$  density component  $n_{0,0}$  represents the density in an area of a circle with a radius of  $\frac{1}{2}\Delta r$ . Therefore, if we draw a Gaussian surface of a circle around this disk with a radius of  $\frac{1}{2}\Delta r$ , the enclosed charge is given by  $-\frac{1}{4}n_{0,0}(\Delta r)^2$ . This leads to a radial electric field at the radius  $r = \frac{1}{2}\Delta r$ , of  $E_r(\frac{1}{2}\Delta r) = -\frac{1}{4}n_{0,0}\Delta r$ . This electric field at  $r = \frac{1}{2}\Delta r$  gives rise to a boundary condition relating to the radial derivative of the electric potential at  $r = \frac{1}{2}\Delta r$ , which can be computed using the points at  $\phi_{0,0}$  and  $\phi_{1,0}$ . Using the finite difference form of the equation  $E_r(\frac{1}{2}\Delta r) = -\frac{\partial\phi}{\partial r}|_{r=\frac{1}{2}\Delta r}$ , we obtain the result  $-\frac{\phi_{1,0}-\phi_{0,0}}{\Delta r} = -\frac{1}{4}n_{0,0}\Delta r$ , or  $\phi_{0,0} - \phi_{1,0} = -\frac{1}{4}n_{0,0}(\Delta r)^2$ . This is the boundary condition used at the origin for the  $m = 0$  component of the system for the plasma potential. For the applied potential  $\phi_{applied}$ , the  $m = 0$  boundary condition at the origin is zero.

After solving for the set of  $\phi_{i,m}$  for each value of  $m$ , iterative refinement is performed to remove errors accumulated in the tridiagonal solve routine. Iterative refinement takes the set of  $\phi_{i,m}$  for each  $m$  and multiplies it by the tridiagonal matrix. This should give back the set of  $n_{i,m}$ . However, due to numerical accumulation of errors, this new set of  $n_{i,m}$  differs from the original by a small difference. This small difference  $\Delta n_{i,m}$  is recorded and reapplied to the tridiagonal solve routine, resulting in a set of small corrections to the potential,  $\Delta\phi_{i,m}$ . Subtracting off this error from the original potential set of  $\phi_{i,m}$  gives the refined potential solution that should have

near machine accuracy precision. A further discussion of iterative refinement may be found in [24].

This process for finding the potential solution set of  $\phi_{i,m}$  is repeated for each value of  $m$ . After all  $\phi_{i,m}$  for all values of  $m$  have been computed, the Fourier series is summed, obtaining the real space electric potential solution  $\phi_{i,j} = \sum \phi_{i,m} e^{im\theta}$  where  $i$  is the index over radius and  $j$  is the angle index which ranges from 1 to  $N_j$ . The electric potential at the origin is represented by  $\phi_{0,0}$ .

This is the method used to solve Poisson's equation for the electric potential. It is second order accurate with respect to  $\Delta r$ . The electric potential found from this solver is then passed to the density derivative routine, discussed in the next section.

### 3.2.2 Density Derivative Routine

The equation for the time derivative of the density is a combination of the continuity equation 2.9 and drift equation 2.10. Inserting equation 2.10 for the drift velocity  $\vec{v}$  into the continuity equation 2.9 gives

$$\frac{\partial n}{\partial t} = (\vec{\nabla} \phi \times \hat{z}) \cdot \vec{\nabla} n$$

which can be rewritten as

$$\frac{\partial n}{\partial t} = (\vec{\nabla} n \times \vec{\nabla} \phi) \cdot \hat{z}. \quad (3.1)$$

Writing this equation in cylindrical coordinates gives the result

$$\frac{\partial n}{\partial t} = \frac{1}{r} \left( \frac{\partial n}{\partial r} \frac{\partial \phi}{\partial \theta} - \frac{\partial n}{\partial \theta} \frac{\partial \phi}{\partial r} \right). \quad (3.2)$$

One might consider applying standard second order finite difference techniques to this equation to obtain a value for the time derivative of the density. However, this approach will lead to computational instability first demonstrated by Phillips [25][26]. Akio Arakawa recognized the cause of this instability, and devised a method to compute the spatial derivatives while maintaining computational stability [27].

Specifically, Arakawa took four second order finite difference representations for the spatial derivatives that used neighboring grid points, and found that a linear combination of these would produce a method that conserved mean density, total energy, and mean squared density, while maintaining computational stability. Using this method, the finite difference representation for the density time derivative is

$$\begin{aligned} \frac{\partial n_{i,j}}{\partial t} = & -\frac{1}{12r_i\Delta r\Delta\theta}[(\phi_{i,j-1} + \phi_{i+1,j-1} - \phi_{i,j+1} - \phi_{i+1,j+1})(n_{i+1,j} - n_{i,j}) \\ & + (\phi_{i-1,j-1} + \phi_{i,j-1} - \phi_{i-1,j+1} - \phi_{i,j+1})(n_{i,j} - n_{i-1,j}) \\ & + (\phi_{i+1,j} + \phi_{i+1,j+1} - \phi_{i-1,j} - \phi_{i-1,j+1})(n_{i,j+1} - n_{i,j}) \\ & + (\phi_{i+1,j-1} + \phi_{i+1,j} - \phi_{i-1,j-1} - \phi_{i-1,j})(n_{i,j} - n_{i,j-1}) \\ & + (\phi_{i+1,j} - \phi_{i,j+1})(n_{i+1,j+1} - n_{i,j}) \\ & + (\phi_{i,j-1} - \phi_{i-1,j})(n_{i,j} - n_{i-1,j-1}) \\ & + (\phi_{i,j+1} - \phi_{i-1,j})(n_{i-1,j+1} - n_{i,j}) \\ & + (\phi_{i+1,j} - \phi_{i,j-1})(n_{i,j} - n_{i+1,j-1})] \end{aligned}$$

where  $i$  is the index over radius,  $r_i = i\Delta r$ , and  $j$  is the index over angle. The radial grid spacing is represented by  $\Delta r$ , and the angular grid spacing by  $\Delta\theta$ .

The boundary condition at the wall is straightforward. For the electric potential, the wall potential is used which is either zero when no external pulse is present, or equal to the applied voltage at the wall during an applied pulse. For the electron density, it is assumed that any electrons that hit the wall will be lost, and the density is therefore zero at the wall. At the origin, the equation must be modified since the area must be calculated differently, and there is no angular component at the origin. The derivative for the density at the origin is given by

$$\begin{aligned} \frac{\partial n_{0,0}}{\partial t} = & -\frac{1}{3\pi(\Delta r)^2} \sum_{j=1}^{N_j} [(\phi_{1,j+1} - \phi_{1,j-1})(n_{0,0} + n_{1,j}) \\ & + (\phi_{0,0} - \phi_{1,j})(n_{0,0} + n_{1,j+1})] \end{aligned}$$

$$+(\phi_{1,j} - \phi_{0,0})(n_{1,j-1} + n_{0,0})]$$

where  $n_{0,0}$  is the density at the origin and  $\phi_{0,0}$  is the electric potential at the origin. The origin does not have an angular component and therefore does not have an angle index  $j$ .

The system has cylindrical symmetry, and therefore is periodic in angle. To handle the boundary conditions in angle, the indices are “wrapped” around. For example, when using the value  $\phi_{i,N_j+1}$ , the value for  $\phi_{i,1}$  is used, and when  $\phi_{i,0}$  is encountered, the value for  $\phi_{i,N_j}$  is used.

This routine will give a second order accurate time derivative of the density at each grid point, given the density and electric potential at each point. With this derivative, the density at each grid point can be advanced in time by the procedure described in the next section.

### 3.2.3 Leapfrog Time Advance

With the above two procedures, the electric potential can be calculated given the electron density distribution, and the density time derivative can be computed using the electric potential and the electron density. The leapfrog method then allows the density to be advanced by a time step  $\Delta t$ .

The leapfrog method begins by calculating the electric potential and density time derivative from the given density distribution. A new temporary density is calculated at half a time step. This can be written as

$$n_{temp_{i,j}}^{t+\frac{1}{2}\Delta t} = n_{i,j}^t + \frac{1}{2}\Delta t \frac{\partial n_{i,j}^t}{\partial t}$$

with the superscripts representing the time variable.

This temporary density is inserted into the Poisson solver and derivative algorithm, resulting in a temporary potential  $\phi_{temp_{i,j}}$  and derivative  $\frac{\partial n_{temp_{i,j}}}{\partial t}$  at a time of  $t + \frac{1}{2}\Delta t$ . This derivative is then used to advance the original density a full time step, written as

$$n_{i,j}^{t+\Delta t} = n_{i,j}^t + \Delta t \frac{\partial n_{temp}^{t+\frac{1}{2}\Delta t}}{\partial t}$$

where the superscripts  $t, t + \frac{1}{2}\Delta t, t + \Delta t$  represent the original time, time advanced half a time step, and time advanced a full time step, respectively.

This procedure is then repeated to advance the density at each grid point in time. The routine is second order accurate with respect to the time step  $\Delta t$ . For the procedure to be numerically stable, the Courant condition requires that the time step be sufficiently small [24]. The maximum stable time step  $\Delta t_{\max}$  must satisfy  $\Delta t_{\max} \lesssim \frac{\Delta r}{v_r}$  and  $\Delta t_{\max} \lesssim \frac{\Delta \theta}{\omega_0(r)}$  for all  $r$ . For the typical resolution of 1024 points in radius and 256 points in angle,  $\Delta t_{\max}$  was experimentally determined to be around  $1 \times 10^{-3}t_{cr}$  where  $t_{cr} = \frac{4\pi\varepsilon_0 B}{en_0(0)}$  is the time for one central rotation. For most computations, values of  $\Delta t$  somewhat below  $\Delta t_{\max}$  were used for the time step. For a resolution of 1024 points in radius and 256 points in angle, a value of  $\Delta t = 5 \times 10^{-4}t_{cr}$  was used.

This now completes the system necessary to advance the density as a function of time and observe the time evolution of the system. The next section discusses diagnostics and output data in the code so that the time evolution of the electric potential and electron density can be conveniently displayed and analyzed.

### 3.2.4 Diagnostics and Outputs

There are several computer data files produced by the code at periodic intervals during a computation, with this interval denoted as a frame. The time step is too small for data to be stored at every time step. Therefore successive frames are separated by hundreds of time steps, with the perturbation rotating approximately  $\frac{1}{8}$  of a revolution between frames. These files contain data describing the density, perturbed density, perturbed potential, Fourier analyzed density and potential, electric field at the wall, and conserved quantities. These output files will be described below.

The plasma density is stored internally as a double precision real value for each grid point throughout the computation. When this file is stored to disk, each grid

point is scaled and rounded into a one byte integer. Thus the density is stored with 8 bit resolution, and the value for the density varies between zero and 255 at each grid point. This scaling is necessary due to the limited disk capacity, where even at 8 bit resolution, for a typical run of 200 frames at 1024 points in radius and 256 points in angle, the total storage requirement is 50 megabytes. Storing the full double precision values at each grid point would require 400 megabytes for this single file (significant in the year 1997). This byte resolution storage method is also used for the perturbed density and perturbed potential.

Often the perturbations are small, and thus no changes are perceptible when observing the total density. For this reason, the perturbed density is also stored. The perturbed density is calculated by subtracting off the unperturbed density at each radius from the total density. This leaves the perturbed density which varies from the background average density. The perturbed density is then scaled so that the perturbation has a value ranging from -127 to +127. The initial scaling factor for the perturbed density is not known ahead of time. If too large a scale factor is used, the perturbed density will exceed the limit of 127, and thus the stored file will be inaccurate. If too small a scale factor is used, the full 8 bit dynamic range will not be exploited. Therefore, a variable scale factor is used. The scale factor is normalized so the highest absolute perturbation has a value of 127 at each instant of time during the application of the applied pulse. After the applied pulse is turned off, the scale factor remains fixed for the remainder of the computation. The value of the maximum absolute perturbation is stored in a separate file, so the scale factor is always known. As the maximum perturbations should not grow after the applied pulse is turned off, this method maximizes the use of the 8 bit dynamic range without saturation. The perturbed density is then stored in byte resolution.

Usually, variations can not be seen in the total potential either. Therefore the same method used for the perturbed density is also used for the perturbed potential, where the average potential is subtracted off, and the difference scaled to byte resolution. Again the scale factor varies during the applied pulse, and then remains fixed throughout the rest of the computation.

The exact rotation frequency of the perturbation is not known before a calculation is performed. The angular frequency profile  $\omega_0(r)$  can be computed, but the resonant frequency of the wave remains unknown. However, a reasonable guess can be made which will be used to calculate the time between frames and the frequency of the initial applied pulse. After the calculation is finished, the actual perturbation rotation frequency can be determined and used to calculate an accurate time between frames and used for the applied pulse frequency in subsequent calculations. The perturbation rotation frequency is less than the central rotation frequency for monotonically decreasing profiles. Thus the time between frames may correspond to  $\sim 0.3t_{cr}$  for a particular density profile, and a total run of 200 frames would correspond to an elapsed time of 60 central rotation periods for this density profile.

After the density, perturbed density, and perturbed potential files have been computed and stored, a conversion program is used to produce 2-D contour plots of these variables. The converter program takes the cylindrical input data, and converts it into rectangular coordinates with 480 by 480 resolution using bilinear interpolation. This resolution is used since the typical resolution for a VGA screen is 640 by 480. This file can then be read by an animation program which will display the files frame by frame in rapid succession, showing smooth flow of plasma in time. The animation program divides the data by 16, giving 16 contours. In the total density picture, the white regions represent high density, and the black regions low density. For the perturbed pictures, the white regions represent areas of high positive perturbation, the middle grey transition represents a contour of zero perturbation, and the black regions represent an area of high negative perturbation.

The  $\sin(m\theta)$  and  $\cos(m\theta)$  components of the density and potential at each radius are stored for the values  $m = 0, 1, 2, 3, 4$  at each frame. The components are stored in full 8 byte double precision. These files allow analysis of the Fourier component variation in both amplitude and phase as a function of radius and time.

Additionally, the electric field at the wall is written to a file in full 8 byte double precision. The electric field is computed by taking the negative of the derivative of the potential at the wall. A second order finite difference is used to approximate the

derivative, using the neighboring grid points to the wall. The electric field is stored for each grid point in angle. The time between storing the electric field is  $\frac{1}{10}$  the time between storing frames. Thus in the time between each density picture, the electric field has been stored 10 times.

Finally, for every frame a file is written which contains several calculated conserved quantities. The finite difference method used in the code should ideally conserve mean density, mean squared density, and total energy. These values are computed over the area of the plasma and written to a text file. It is found that for a small amplitude perturbation, the mean density and mean squared density are found to vary by less than 1 part in  $10^9$ . For a very large amplitude perturbation, the mean density may vary by 1 part in  $10^7$ , and the mean squared density may vary by 1 part in  $10^3$ . At very large amplitudes, some plasma may hit the wall and be lost.

There is one more feature of the code worth mentioning here. It is often useful to observe the plasma dynamics in the rotating frame that is moving with the plasma perturbation. For the system of equations we are studying, moving into the rotating frame is equivalent to including a uniform, time independent, positively charged background density in the calculation. This can be seen by using the result that the rigid rotor solution to the fluid equations has a uniform density distribution as discussed in Chapter 1. The rotation frequency of the rigid rotor is proportional to the value of the uniform density. This value for the background positively charged density is placed into the Poisson solver, where the density used in the solver is the electron density minus the uniform positively charged background density. This will then remove the rotation of the wave, and allow the plasma dynamics to be observed in the rotating frame.

The value of the uniform positive background density is chosen to remove the rotation of the perturbed potential. This wave angular frequency value may not be known ahead of time, as discussed earlier. Therefore, a feedback loop is used to track the perturbed potential position in angle, and adjust the value of the uniform positive background density to keep the perturbation from rotating. This adjustment is made at each frame, and the new perturbation frequency is written to a file. This tracking

method is also useful for determining if the wave frequency changes with time.

### 3.2.5 Accumulated Errors

There are several sources of errors in the Nonlinear Fluid Code. First, all spatial derivatives are second order accurate in  $\Delta r$  and  $\Delta\theta$ . In time, higher order error terms accumulate, producing fine scale numerical structure. The error becomes more significant when spatial features of the plasma approach the dimensions of the grid resolution. The grid can not accurately represent features that are smaller than the grid spacing.

Additionally, errors exist in the time integration method. The leapfrog time step method discussed above is second order accurate in  $\Delta t$ . These errors also accumulate in time, and limit the accuracy of the code for later times.

The nonlinear fluid code also suffers from aliasing errors [27]. These errors manifest themselves as phase inaccuracies and distortions in the spectral distribution of energy. However, the total energy and average scale of motion do not suffer from these aliasing errors.

Due to these accumulated errors, the results from the code become less accurate for long integration times. These errors may be observed in images of the perturbed density as small points of perturbed density with dimensions on the order of the grid resolution. As the computation proceeds, this high spatial frequency component becomes more evident, and contours of constant perturbed density become “fuzzy” due to accumulated numerical noise.

Therefore, the computation is valid for a limited range in time. Typically, a computation is stopped at 200 frames, corresponding to 60 – 100 central rotation periods. At 200 frames, the effects from numerical noise become noticeable.

It is possible to reduce the accumulated errors by increasing the grid resolution and decreasing the time step. Increasing the radial and angular resolution by a factor of 2 requires decreasing the time step by a factor of 2, and the required computation time increases by a factor of 8. Since increasing the grid resolution substantially

increases computation time, it is not always practical to use higher resolutions.

### 3.3 Linearized Fluid Code

The final linearized equation from the previous chapter, equation 2.15, is a differential equation for the perturbed electric potential  $\tilde{\phi}_{1,m}(r, \omega)$  as a function of the radius  $r$  and angular frequency  $\omega$ , with an assumed angular dependence of  $e^{im\theta}$  where  $m$  is the azimuthal symmetry eigenmode number. The plasma density is then related to the potential through the Poisson equation. To obtain the time evolution of the system, it is necessary to solve  $\tilde{\phi}_{1,m}(r, \omega)$  for various frequencies, and perform an inverse Laplace transform. In the linear equations, different  $m$  modes are clearly independent of each other. Therefore, for simplicity a single  $m$  mode is studied.

A range of  $\omega$  is chosen, and this frequency range is then divided into 512 discrete frequencies. This range is selected to include the azimuthal symmetry eigenmode number  $m$  times the fluid rotational velocity  $\omega_0(r)$  at each radii and neighboring frequencies at which the plasma has a significant response. For each discrete frequency, the equation is solved for 500 points in radius using a fourth order Runge-Kutta method. There is a pole in the equation when  $\omega = m\omega_0(r)$ , and numerical difficulties with this pole are avoided by including a small positive imaginary component to the frequency.

Boundary conditions for the transformed potential are specified at the origin and at the wall for the integration. The density perturbation is expected to be very small at the origin, and therefore the Laplace equation vacuum solution  $\tilde{\phi}_{1,m}(r, \omega) = Ar^m$  is used for the first few integration points, where  $A$  is an unknown constant which is initially assumed to be one. Equation 2.15 is then integrated outward to the wall via the Runge-Kutta method for a discrete set of 512 angular frequencies. The boundary condition at the wall is set by assuming a potential perturbation which is described by the discrete transform of a delta function in time at  $t = 0$ . The delta function solution can be treated as a Green's function in order to construct a solution for an applied pulse with a finite time extent. A delta function impulse in time corresponds

to a flat frequency spectrum with all frequency modes of the applied potential at the wall equal to one. When the Runge-Kutta scheme reaches the wall, the potential in general will not be equal to one. To remedy this, the solution is then renormalized by dividing the potential at each radius by the final wall potential. This procedure is valid because the equations are linear. This then gives the final solution for  $\tilde{\phi}_{1,m}(r, \omega)$  with the correct boundary conditions at the origin and at the wall. This solution procedure is applied to all 512 discrete frequencies.

The discrete numerical solution  $\tilde{\phi}_{1,m}(r, \omega)$  is the approximate delta function impulse response of the system to a potential applied at the wall. This solution is “windowed” by multiplying the solution by a function that approaches zero near the boundary frequencies to remove aliasing errors due to the finite extent of the discrete frequency range. A Gaussian in frequency which rolls off quickly near the edge frequencies is used to window the solution  $\tilde{\phi}_{1,m}(r, \omega)$ . This Gaussian function is multiplied by the solution  $\tilde{\phi}_{1,m}(r, \omega)$  for all radii at each specific angular frequency. This is equivalent to using a burst with a short Gaussian envelope to excite the perturbation, instead of a delta function. Again this is valid due to the fact that the system is linear.

To find the time dependence, an inverse *Laplace* transform of  $\tilde{\phi}_{1,m}(r, \omega)$  is required. However, the function to be transformed has only been computed at 512 discrete frequencies. We would like to perform this inverse transform using discrete fast *Fourier* transform (DFT) methods, except that the frequencies used in evaluating the function are not real, but are complex and contain a small imaginary part. If a DFT, which assumes data at real frequencies were to be used, an artificial exponential decay would be introduced. However, as the argument below shows, this is readily corrected.

To correct for this artificial decay, the solution  $\phi_{1,m}(r, t)$  is multiplied by  $e^{\omega_i t}$  where  $\omega_i$  is the constant imaginary part of the angular frequency. This correction may be understood from the definition of the inverse Laplace transform

$$f(t) = \frac{1}{2\pi} \int_{-\infty}^{\infty} \tilde{f}(\omega) e^{-i\omega t} d\omega$$

where  $\omega$  is in the upper half plane, i.e.,  $\omega = \omega_r + i\omega_i$ . This can be written

$$f(t) = \frac{1}{2\pi} \int_{-\infty}^{\infty} \tilde{f}(\omega_r + i\omega_i) e^{-i(\omega_r + i\omega_i)t} d\omega_r.$$

Since the imaginary part of the frequency  $\omega_i$  is a constant, the exponential can be taken outside of the integral giving

$$f(t) = \frac{1}{2\pi} e^{\omega_i t} \int_{-\infty}^{\infty} \tilde{f}(\omega_r + i\omega_i) e^{-i\omega_r t} d\omega_r.$$

This is a routine to perform the inverse transform using *real values for  $\omega$*  even though the function  $\tilde{f}(\omega)$  has been evaluated by including an *imaginary part for  $\omega$* . Therefore DFT routines can be used, provided that a correction is included after the inverse transform has been completed.

Now that the time dependent solution of the potential has been found, the time dependent electric field at the wall is equal to the negative of the derivative of the electric potential at the wall. Additionally, the time dependence of the perturbed density is given by the Laplacian of the time dependent potential through Poisson's equation 2.8, and is computed in the code with the electric potential. Images of the perturbed density are generated by including the angular dependence, and dividing the density into 16 equally spaced contours.

### 3.4 Conclusion

Both the Nonlinear Fluid Code and the Linearized Fluid Code are useful for studying pure electron plasmas. The Nonlinear Fluid Code is useful for studying higher amplitude effects where nonlinear terms are important. The required computational time varies, depending on the complexity of the case running, but a typical calculation

requires one week of computation on a 133 MHz Pentium PC. The Linearized Fluid Code is convenient for studying a variety of small amplitude effects quickly, since the computation requires only 20 minutes on a 66 MHz 486 PC.

For small amplitudes, the results from the Nonlinear Fluid Code are found to agree with the results of the Linearized Fluid Code. This is a useful diagnostic, as each code uses a different method for solving the equations. Obtaining the same results with each method for low amplitude applied pulses provides evidence that the computational methods are valid.

These two computational methods are used to study a variety of aspects in pure electron plasmas. The results from these computations are the subject of the next several chapters.

# Chapter 4 Small Amplitude Disturbances

## 4.1 Introduction

Before attempting to solve large amplitude nonlinear problems, the Nonlinear Fluid Code was first used to study small amplitude disturbances in order to verify that the well understood results from linear calculations could be reproduced using the Nonlinear Fluid Code. For small amplitude perturbations, the results from the Nonlinear Fluid Code were found to agree with the results from the Linearized Fluid Code.

The linearized differential equation approach has been used many times in previous research on non-neutral plasmas. In particular, computational work by Pillai [19] using a Linearized Fluid Code found that, for a small amplitude applied pulse, the response of the plasma at the wall decays exponentially for early times, and transitions to an algebraic decay at later times. He also found that by choosing a plausible density profile, he could match the experimentally observed decay rates. However, there is no reason to believe that the density profile he chose is the only profile that has a decay rate which matches the experimental decay rate.

The first section will describe perturbations in the electric field at the wall resulting from application of an external pulse. The perturbed electric field at the wall is found to decay exponentially in time. Several density profiles are considered, and the decay rate is found to be strongly dependent on the radial density profile. The decay rate is studied as a function of the density profile, and compared to the theoretical prediction of Briggs, Daugherty, and Levy [10].

The second section will describe the density perturbations caused by the external pulse. The perturbed density images illustrate the sheared flow of the plasma, and explain the collisionless damping as a phase mixing process caused by the different

radial layers rotating at different rates. Images of the perturbed density will be compared for plasmas with different radial density profiles and different decay rates.

Finally an approximate analytic solution to the linearized fluid equations will be presented and compared to the results from the computation. The approximate solution models the perturbed potential as a decaying exponential function, and models the perturbed density as a sum of two exponentials. Using parameters obtained from the computation, the images of the perturbed density can be reproduced.

## 4.2 Collisionless Damping

### 4.2.1 Fast Decay Profile

The Nonlinear Fluid Code is used to study the response of a pure electron plasma to an externally applied pulse. The response of the plasma is observed in the perturbed electric field at the wall. After application of the external pulse, the perturbed electric field at the wall is found to decay exponentially in time. The decay rate is a strong function of the unperturbed density profile. These results are consistent with those found by N. Sateesh Pillai [19].

The Nonlinear Fluid Code is used to study the unperturbed normalized density profile  $n_0(r) = n_0(0)\{1 - 3r^2 + 3r^4 - r^6\}$  for  $r \leq 1$ . This normalized density profile has a value of one at the origin, with the first derivative vanishing at the origin. Furthermore, the density is monotonically decreasing to zero at the plasma edge at  $r = 1$ , with two derivatives vanishing at the plasma edge. The density profile may also incorporate a parameter  $\alpha$  which is the radius of the edge of the plasma, beyond which there is vacuum until the wall. For values of  $\alpha < 1$ , the normalized density profile is modified to become  $n_0(r) = n_0(0)\{1 - 3(\frac{r}{\alpha})^2 + 3(\frac{r}{\alpha})^4 - (\frac{r}{\alpha})^6\}$  for  $r < \alpha$ , and  $n_0(r) = 0$  for  $r \geq \alpha$ .

Each density profile has a corresponding radial electric field due to the electrostatic space charge of the plasma. The radial electric field causes an  $\vec{E} \times \vec{B}$  drift velocity in the plasma perpendicular to the electric field, creating a rotation of the plasma.

This drift velocity at each radius corresponds to an angular velocity at that radius. For a plasma with uniform density, the angular velocity is constant in radius, and the plasma rotates as a rigid rotor. For a monotonically decreasing profile as presented above, the angular velocity is different at different radii, and the flow is sheared. For the normalized density profile presented above, the normalized angular velocity profile is given by  $\omega_0(r) = \omega_0(0)\{1 - \frac{3}{2}r^2 + r^4 - \frac{1}{4}r^6\}$  where  $\omega_0(0) = \frac{\omega_p^2(0)}{2\omega_c} = \frac{1}{2} \frac{en_0(0)}{\varepsilon_0 B}$  is the central angular rotation frequency. For values of  $\alpha < 1$ , the normalized angular velocity profile is modified to become  $\omega_0(r) = \omega_0(0)\{1 - \frac{3}{2}(\frac{r}{\alpha})^2 + (\frac{r}{\alpha})^4 - \frac{1}{4}(\frac{r}{\alpha})^6\}$  for  $r < \alpha$ , and  $\omega_0(r) = \omega_0(0)\{\frac{1}{4}(\frac{r}{\alpha})^2\}$  for  $r \geq \alpha$ . For the computation in this section, the value  $\alpha = 0.8$ . is chosen. A plot of the normalized density profile and normalized angular velocity is shown in figure 4.1.

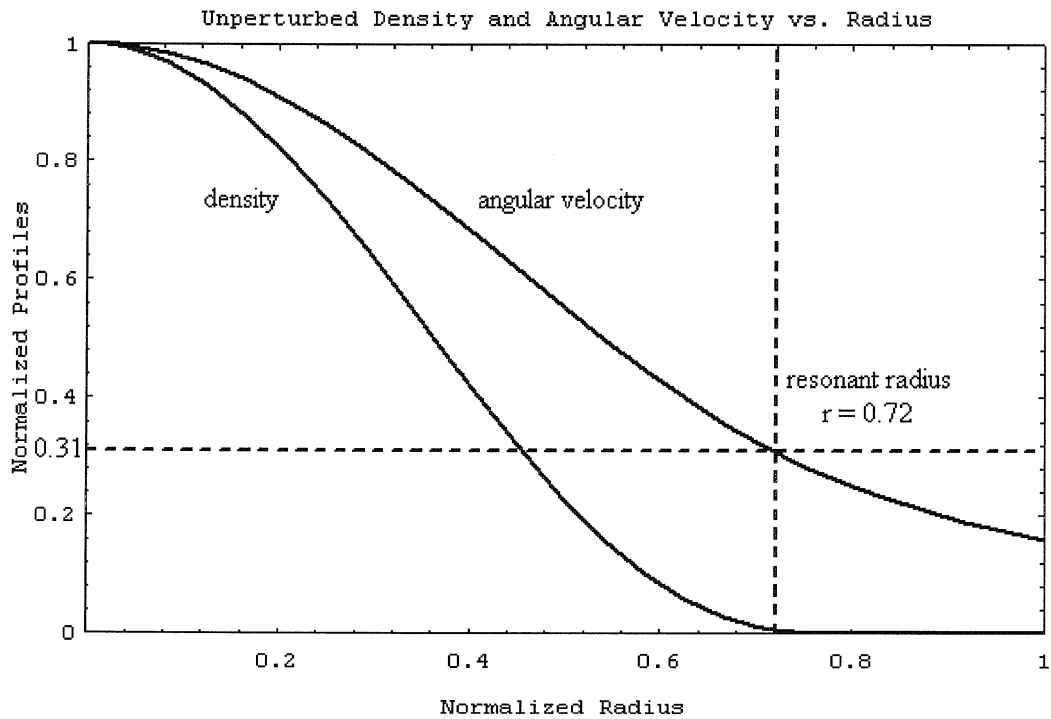


Figure 4.1: Plot of the normalized unperturbed density and normalized angular velocity versus radius for the Fast Decay Profile  $n_0(r) = n_0(0)\{1 - 3(\frac{r}{\alpha})^2 + 3(\frac{r}{\alpha})^4 - (\frac{r}{\alpha})^6\}$  with the edge of the plasma at  $\alpha = 0.8$ . The  $m = 2$  resonant radius at  $r_s = 0.72r_w$  is indicated by the dashed vertical line.

A perturbation in the plasma will propagate with a certain phase velocity. For a

monotonically decreasing density profile, at a single radius, the  $\vec{E} \times \vec{B}$  drift velocity of the plasma may be equal to the phase velocity of the wave. This radius is denoted as the resonant radius  $r_s$ . For the density profile in figure 4.1, the  $m = 2$  resonant radius is indicated by a dashed vertical line.

The computation begins with a three cycle sinusoidal pulse of voltage applied to sectors along the wall to excite a perturbation in the plasma with  $m = 2$  azimuthal symmetry. The configuration of the sectors is modeled after the experiment, which was shown in figure 1.1(b) of Chapter 1. The pulse is applied at the  $m = 2$  resonant angular frequency, which is found to be  $\omega_r = 0.61\omega_0(0)$  for this profile. Because the resonant angular frequency is not known before the computation is performed, each computation is performed with an initial guess of the resonant frequency. From the response of the initial computation, a resonant frequency is calculated and used for the applied pulse frequency in subsequent calculations. The resonant angular frequency of  $\omega_r = 0.61\omega_0(0)$  corresponds to a resonant radius at  $r_s = 0.72r_w$  for this profile, where  $r_w$  is the wall radius. At this radius, the plasma has an unperturbed density of  $0.0060n_0(0)$ . The amplitude of the applied pulse is  $5 \times 10^{-5}\phi_0$  where  $\phi_0$  is the electric potential at the origin. For this profile  $\phi_0 = -0.101185\frac{e}{\varepsilon_0}n_0(0)r_w^2$ .

Figure 4.2 shows a plot of the perturbed electric field at the wall as a function of time. Time is presented in units of the central rotation period  $t_{cr} = \frac{4\pi\varepsilon_0 B}{en_0(0)}$ . The perturbed field oscillates as the plasma density perturbations rotate past the wall sectors. In this plot, you can see the perturbation increasing in amplitude, approximately linearly, for the first three cycles while the applied pulse is present. After the applied pulse has terminated, a decay of the perturbation, which is approximately exponential, is observed. The perturbed electric field reaches a maximum of 0.0086% of the unperturbed electric field at the wall for this three cycle applied pulse. For this profile, the unperturbed electric field at the wall has the value  $-0.08\frac{e}{\varepsilon_0}n_0(0)r_w$ .

Figure 4.3 is a plot of the envelope of the perturbed electric field at the wall versus time on a semilog scale, separated into angular Fourier components. This plot more clearly illuminates the exponential decay of the perturbation, and also shows a transition to an algebraic decay later in time [10][19][28], with interference between

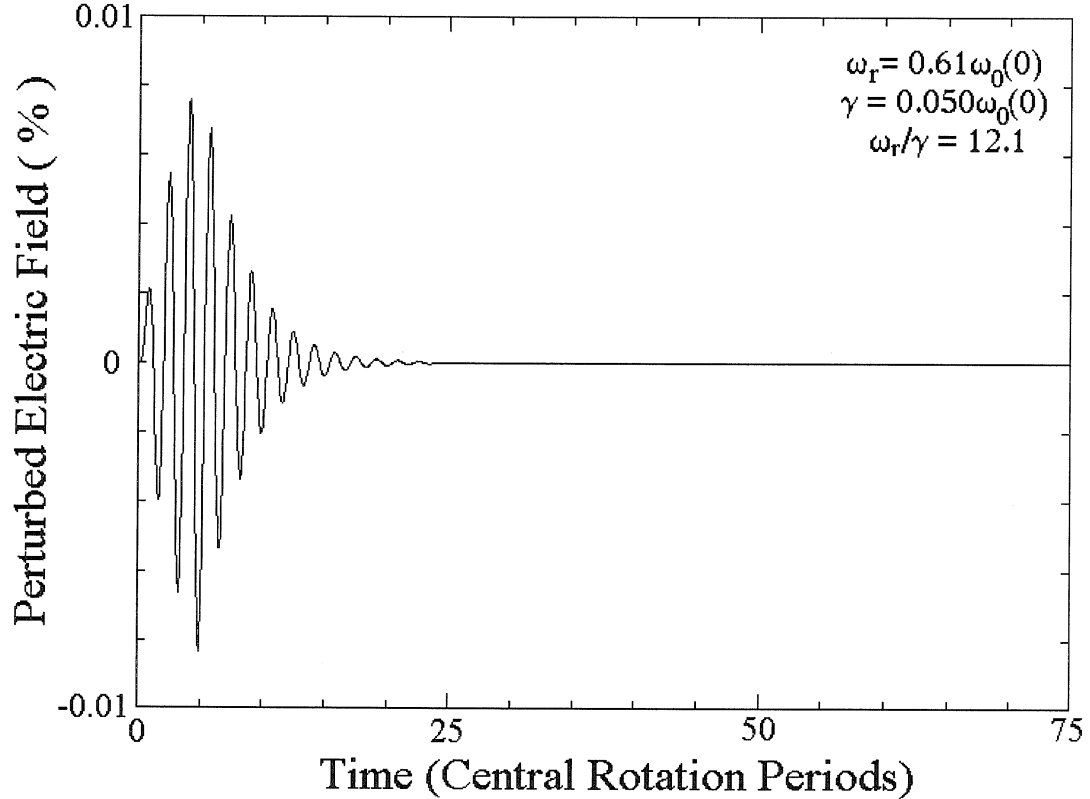


Figure 4.2: Plot of the perturbed electric field at the wall versus time for the Fast Decay Profile  $n_0(r) = n_0(0)\{1 - 3(\frac{r}{\alpha})^2 + 3(\frac{r}{\alpha})^4 - (\frac{r}{\alpha})^6\}$  with  $\alpha = 0.8$ . A three cycle burst of voltage is applied at the wall with an amplitude of  $5 \times 10^{-5}\phi_0$ . The response in the perturbed electric field at the wall reaches a maximum amplitude of 0.0086% of the unperturbed field at the wall, and then decays exponentially in time.

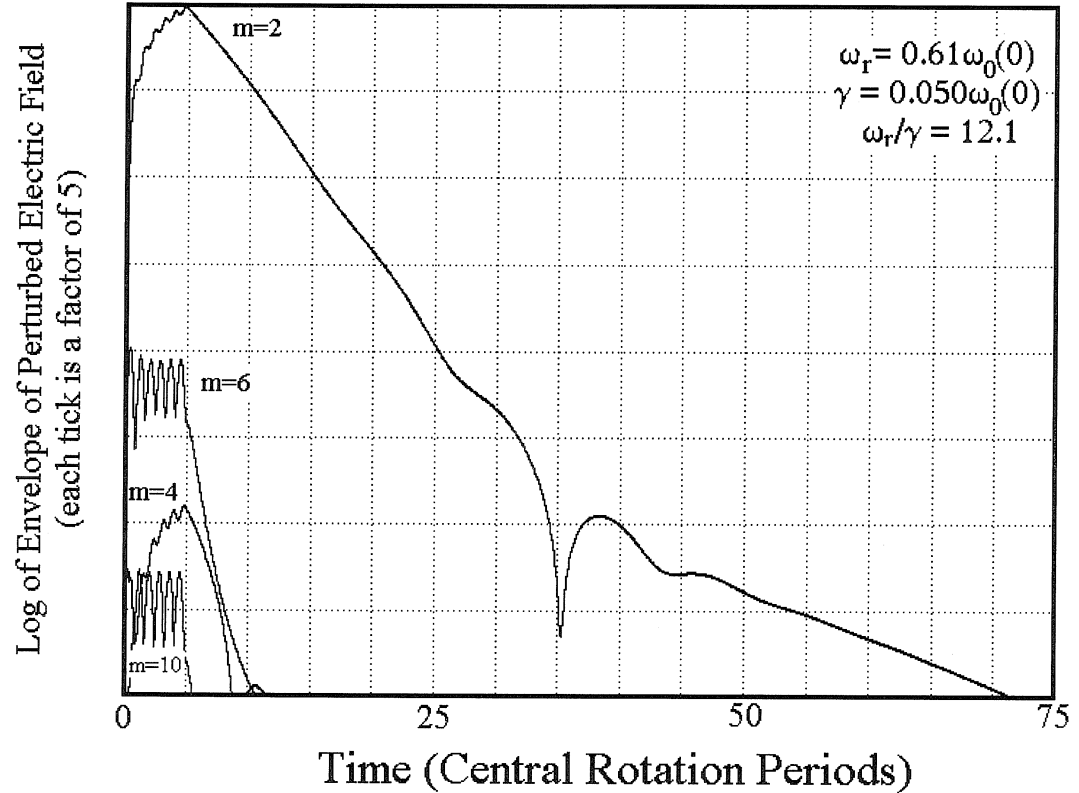


Figure 4.3: Semilog plot of the amplitude of the Fourier components of the electric field at the wall versus time for the Fast Decay Profile  $n_0(r) = n_0(0)\{1 - 3(\frac{r}{\alpha})^2 + 3(\frac{r}{\alpha})^4 - (\frac{r}{\alpha})^6\}$  with  $\alpha = 0.8$ . The exponential decay of the  $m = 2$  perturbation is observed, followed by a transition to an algebraic decay. The perturbation is excited by a three cycle burst of voltage on wall sectors with amplitude  $5 \times 10^{-5}\phi_0$ . The perturbed  $m = 2$  electric field at the wall reaches a maximum amplitude of 0.0086% of the unperturbed electric field at the wall. The  $m = 4$  component is a harmonic of the  $m = 2$  pulse that is generated within the plasma, while the other higher  $m$  values are excited by spatial harmonics of the sectored electrode. Each tick on the vertical axis represents a factor of 5 in amplitude.

the two contributions during the transition. The initial decay rate for the  $m = 2$  component is found to be  $\gamma = 0.050\omega_0(0)$  leading to a value of  $\frac{\omega_r}{\gamma} = 12.1$  for this density profile.

In addition to the  $m = 2$  mode, higher Fourier components are also observed in figure 4.3. The components  $m = 2$ ,  $m = 6$ ,  $m = 10$ , and  $m = 14$  are excited directly by the sectored electrode structure (shown in figure 1.1(b) of Chapter 1), which has angular Fourier coefficients of  $\frac{2\sqrt{2}}{\pi}$ ,  $\frac{2\sqrt{2}}{3\pi}$ ,  $\frac{2\sqrt{2}}{5\pi}$ , and  $\frac{2\sqrt{2}}{7\pi}$ , respectively for this  $m = 2$  sector configuration. In contrast, the  $m = 4$  Fourier component is not excited directly from the sectors. Instead, this component is a harmonic of the  $m = 2$  mode that is generated within the plasma. These higher Fourier components are not of too much concern for this chapter, but they will become more important in Chapter 6 where plasma wave echoes are discussed.

To demonstrate the effect of a sectored electrode structure, a second computation was performed using the same profile, but with a pure angular  $m = 2$  electric potential perturbation rather than a sectored electric potential configuration applied to the wall. Additionally, a Gaussian pulse shape in time is applied in a frame rotating with the wave, rather than using a three cycle sinusoidal pulse. The Gaussian pulse reaches a maximum amplitude of  $1.18 \times 10^{-4}\phi_0$  and has a full width at half maximum (FWHM) of  $1.06t_{cr}$  where  $t_{cr}$  is the time for one central rotation. The perturbed electric field at the wall reaches a maximum value of 0.015% of the unperturbed electric field at the wall.

Figure 4.4 is a semilog plot of the Fourier components of the electric field at the wall versus time for this applied Gaussian pulse. As is seen from the figure, the initial exponential decay rate is unchanged for the  $m = 2$  component of the electric field at the wall. However, since the wall perturbation has a pure  $m = 2$  angular symmetry, the  $m = 6$ ,  $m = 10$ , and  $m = 14$  components are no longer directly excited from the applied pulse at the wall. The  $m = 4$  component remains, however, as it is a harmonic that is generated by the plasma. Higher order harmonics are also generated, but are too small in amplitude to be visible in figure 4.4.

As we will see in the next section, the decay rate depends strongly on the unper-

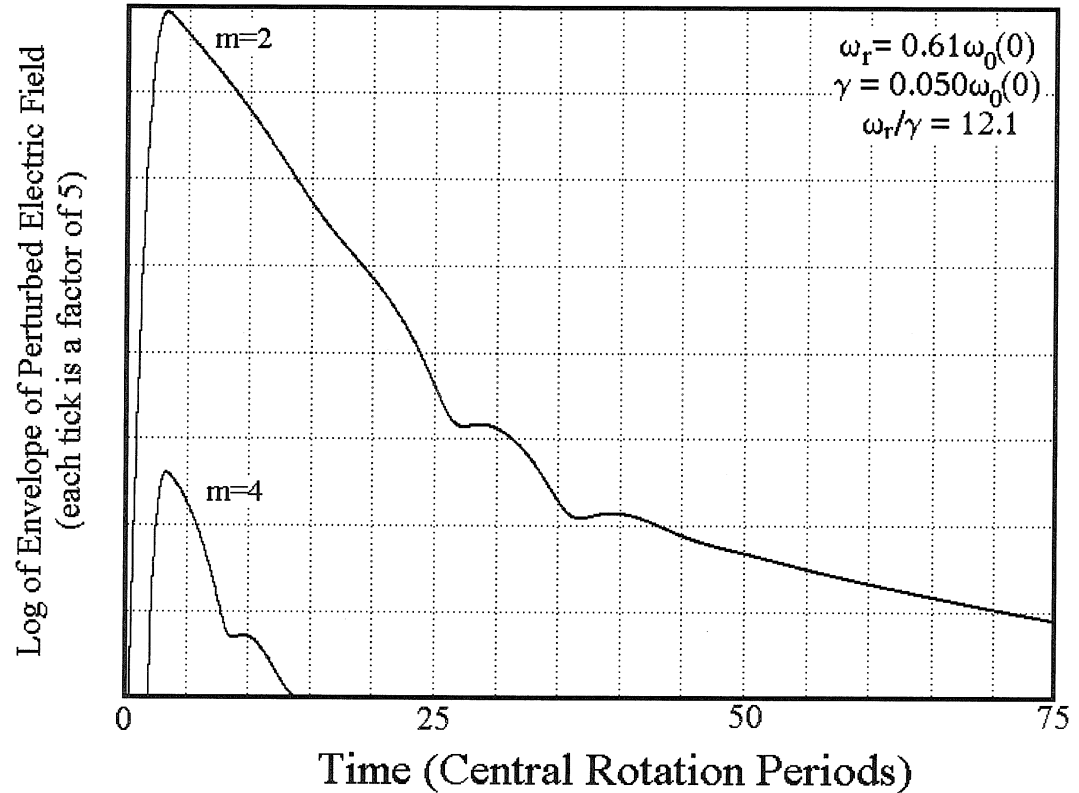


Figure 4.4: Semilog plot of the amplitude of the Fourier components of the electric field at the wall versus time for the Fast Decay Profile  $n_0(r) = n_0(0)\{1-3(\frac{r}{\alpha})^2+3(\frac{r}{\alpha})^4-(\frac{r}{\alpha})^6\}$  with  $\alpha = 0.8$ . Each tick on the vertical axis represents a factor of 5 in amplitude. This calculation uses a pure angular  $m = 2$  excitation at the wall. The applied pulse has a Gaussian shape, reaching a maximum amplitude of  $1.18 \times 10^{-4}\phi_0$  with a FWHM of  $1.06t_{cr}$ . The  $m = 2$  perturbed electric field reaches a maximum amplitude of 0.015% of the unperturbed electric field at the wall. The  $m = 4$  component is a harmonic that is generated within the plasma.

turbed density profile. The perturbations of the electric field at the wall decay rather quickly for the density profile discussed in this section. Accordingly, I will refer to this density profile,  $n_0(r) = n_0(0)\{1 - 3(\frac{r}{\alpha})^2 + 3(\frac{r}{\alpha})^4 - (\frac{r}{\alpha})^6\}$  with  $\alpha = 0.8$  as the *Fast Decay Profile*. Since this profile exhibits strong damping, it is useful for studying the mechanism that causes the decay of perturbations in the electric field at the wall. The Fast Decay Profile will be the primary density profile used in Chapter 6.

#### 4.2.2 Slow Decay Profile

The previous section looked at the decay rate of the electric field at the wall for the Fast Decay Profile. This section will examine a density profile that has a much lower decay rate. The computation in this section uses the same Gaussian pulse shape excitation in a pure  $m = 2$  electric potential perturbation at the wall, reaching a maximum amplitude of  $1.18 \times 10^{-4}\phi_0$  and a FWHM of  $1.06t_{cr}$ .

This section discusses the normalized density profile  $n_0(r) = n_0(0)\{1 - 6(\frac{r}{\alpha})^4 + 8(\frac{r}{\alpha})^6 - 3(\frac{r}{\alpha})^8\}$  with  $\alpha = 0.8$ . The corresponding normalized angular velocity is  $\omega_0(r) = \omega_0(0)\{1 - 2(\frac{r}{\alpha})^4 + 2(\frac{r}{\alpha})^6 - \frac{3}{5}(\frac{r}{\alpha})^8\}$ . This density profile is flatter near the origin, with three derivatives vanishing at the origin, and smooth near the edge with two derivatives vanishing at the plasma edge. A plot of this normalized density profile and normalized angular velocity profile is shown in figure 4.5. This profile has a central electric potential of  $\phi_0 = -0.142696\frac{e}{\varepsilon_0}n_0(0)r_w^2$ , and an unperturbed electric field at the wall of  $-0.128\frac{e}{\varepsilon_0}n_0(0)r_w$ .

For this profile, the  $m = 2$  resonant angular frequency is found to be  $\omega_r = 0.843\omega_0(0)$ , which corresponds to a resonant radius of  $r_s = 0.779r_w$ . The plasma density at this radius is  $0.00053n_0(0)$ . For the given applied pulse, the electric field at the wall reaches a maximum perturbation of 0.027% of the unperturbed electric field at the wall. The initial decay rate of the perturbed electric field at the wall is found to be  $\gamma = 0.0089\omega_0(0)$  which leads to a value of  $\frac{\omega_r}{\gamma} = 95$ . A semilog plot of the Fourier components of the electric field at the wall versus time for this profile is shown in figure 4.6.

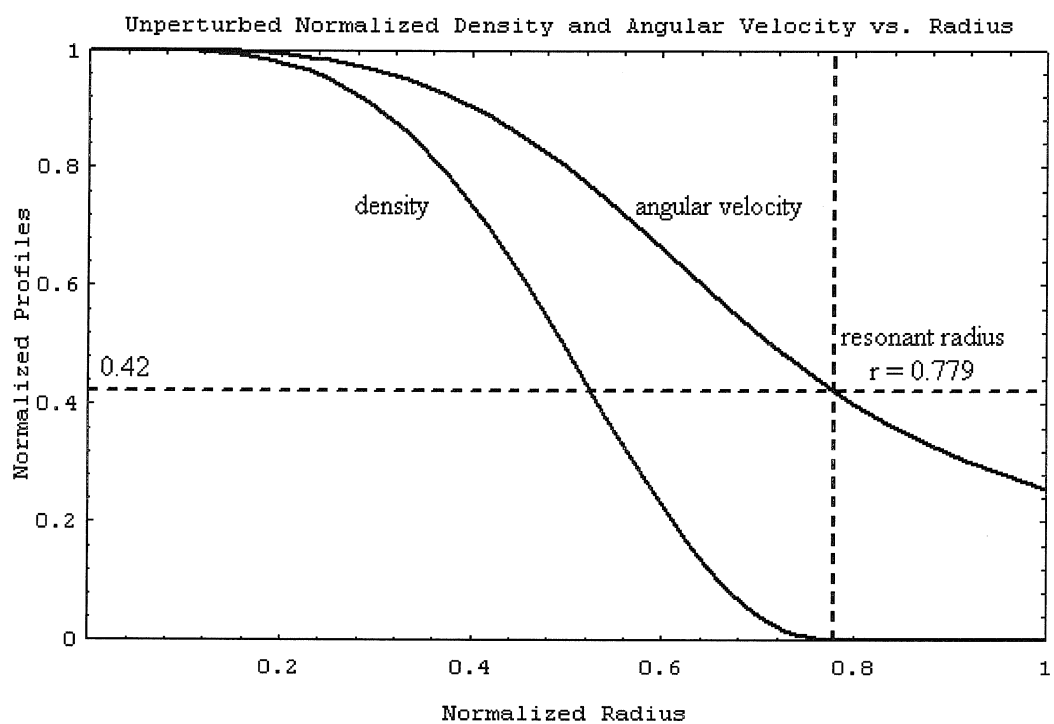


Figure 4.5: Plot of the normalized unperturbed density and normalized angular velocity versus readius for the Slow Decay Profile  $n_0(r) = n_0(0)\{1 - 6(\frac{r}{\alpha})^4 + 8(\frac{r}{\alpha})^6 - 3(\frac{r}{\alpha})^8\}$  with the edge of the plasma at  $\alpha = 0.8$ . The  $m = 2$  resonant radius at  $r_s = 0.779r_w$  is indicated by the dashed vertical line.

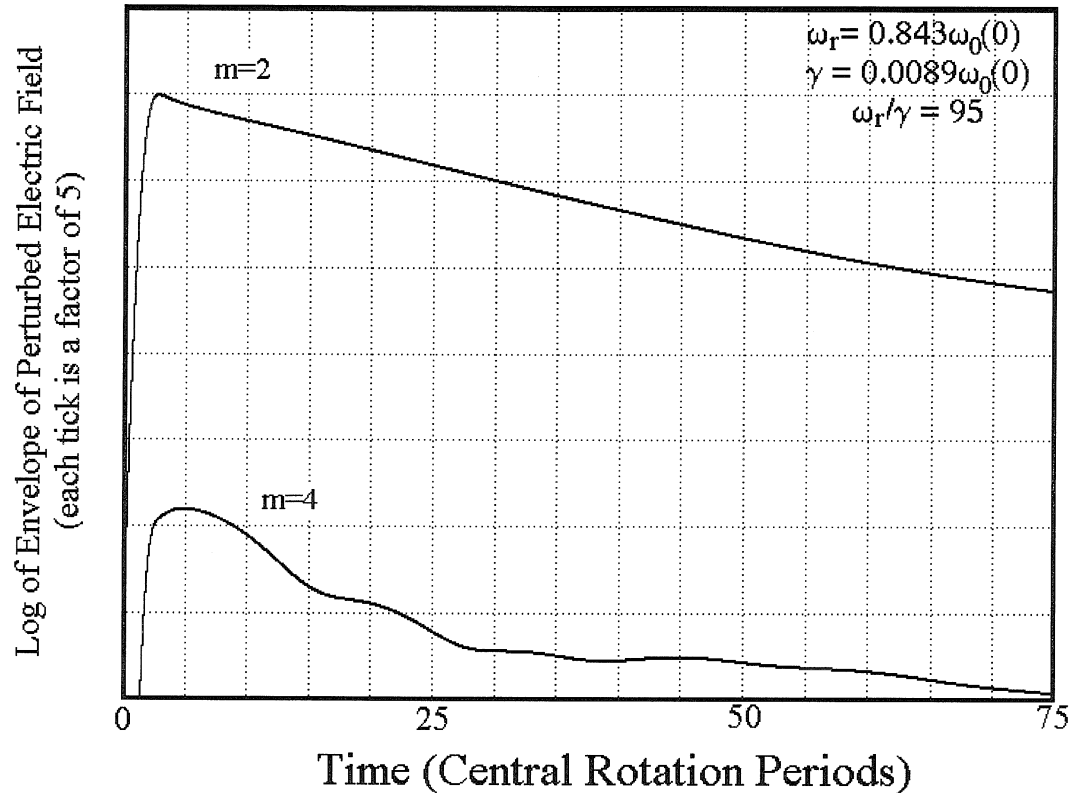


Figure 4.6: Fourier components of the electric field at the wall versus time for the Slow Decay Profile  $n_0(r) = n_0(0)\{1 - 6(\frac{r}{\alpha})^4 + 8(\frac{r}{\alpha})^6 - 3(\frac{r}{\alpha})^8\}$  with  $\alpha = 0.8$ . This calculation uses a pure  $m = 2$  excitation at the wall. The applied pulse has a Gaussian shape, reaching a maximum amplitude of  $1.18 \times 10^{-4}\phi_0$  with a FWHM of  $1.06t_{cr}$ . The perturbed  $m = 2$  electric field at the wall reaches a maximum amplitude of 0.027% of the unperturbed electric field at the wall. Each tick on the vertical axis represents a factor of 5 in amplitude.

As seen from figure 4.6, this profile has wall electric field perturbations that decay much more slowly than those of the Fast Decay Profile. Therefore, I have named the density profile  $n_0(r) = n_0(0)\{1 - 6(\frac{r}{\alpha})^4 + 8(\frac{r}{\alpha})^6 - 3(\frac{r}{\alpha})^8\}$  with  $\alpha = 0.8$  the *Slow Decay Profile*. This profile was chosen because, in the low amplitude limit, the wall electric field perturbation decay rate of this profile is similar to the decay rate found in the experiment of N Sateesh Pillai [19]. Since the linear decay rate of the experiment matches the linear decay rate for this profile, the Slow Decay Profile is expected to resemble the experimental density profile. The Slow Decay Profile will be used for the computations of Chapter 5 where higher amplitude applied pulses cause trapping oscillations.

An  $m = 4$  perturbation is also visible in this computation. As mentioned previously, the  $m = 4$  perturbation is a harmonic that is driven by the  $m = 2$  perturbation in the plasma. The  $m = 4$  mode has its own resonant frequency and decay rate that differs from the  $m = 2$  mode. Since the  $m = 4$  mode is being driven by the  $m = 2$  perturbation at the  $m = 2$  resonant frequency rather than at the  $m = 4$  resonant frequency, there is an interference effect present that causes a modulation of the  $m = 4$  perturbation.

#### 4.2.3 No Decay Profile

Another density profile with a still different behavior is given by  $n_0(r) = n_0(0)\{1 - 10(\frac{r}{\alpha})^6 + 15(\frac{r}{\alpha})^8 - 6(\frac{r}{\alpha})^{10}\}$  with  $\alpha = 0.8$ . The corresponding angular velocity profile is  $\omega_0(r) = \omega_0(0)\{1 - \frac{5}{2}(\frac{r}{\alpha})^6 + 3(\frac{r}{\alpha})^8 - (\frac{r}{\alpha})^{10}\}$ . This density and angular velocity profile is shown in figure 4.7. The central potential is  $\phi_0 = -0.165036\frac{e}{\epsilon_0}n_0(0)r_w^2$ , and the unperturbed electric field at the wall is  $-0.16\frac{e}{\epsilon_0}n_0(0)r_w$ .

Again a Gaussian pulse shape excitation is applied with pure  $m = 2$  symmetry, reaching a maximum amplitude of  $1.18 \times 10^{-4}\phi_0$  and having a FWHM of  $1.06t_{cr}$ . For this profile, the  $m = 2$  resonant angular frequency is found to be  $\omega_r = 0.98\omega_0(0)$ , which corresponds to a resonant radius of  $r_s = 0.81r_w$ . The resonant radius lies outside of the plasma edge, at  $r = 0.80r_w$  since  $\alpha = 0.8$ . For the given applied

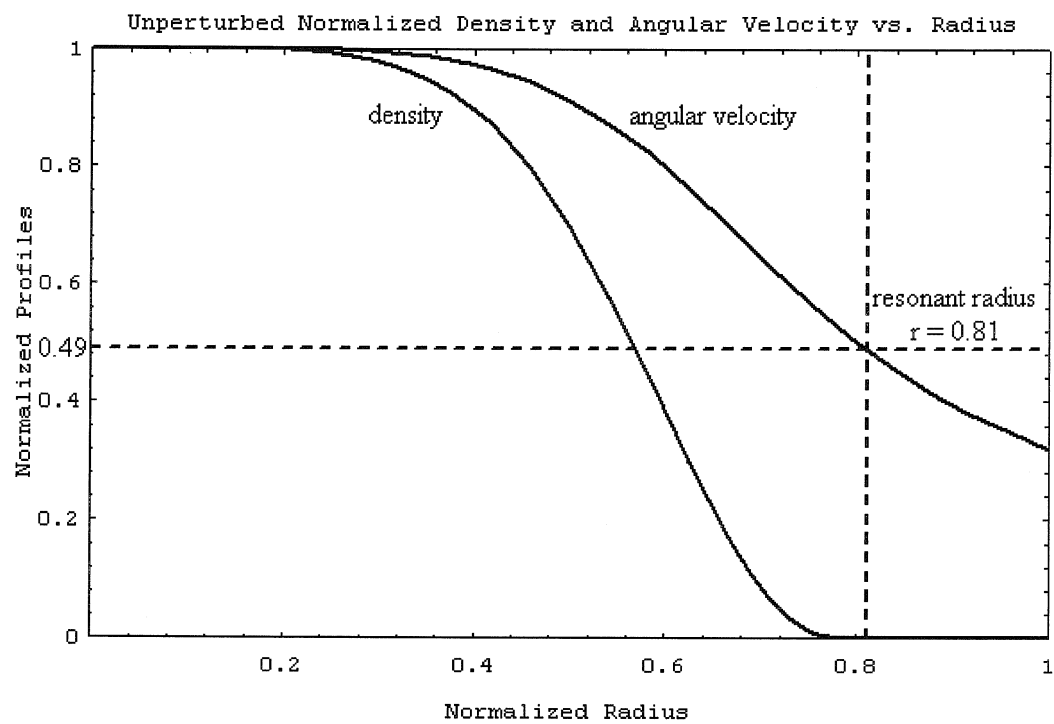


Figure 4.7: Plot of the normalized unperturbed density and normalized angular velocity versus radius for the No Decay Profile  $n_0(r) = n_0(0)\{1 - 10(\frac{r}{\alpha})^6 + 15(\frac{r}{\alpha})^8 - 6(\frac{r}{\alpha})^{10}\}$  with the edge of the plasma at  $\alpha = 0.8$ . The  $m = 2$  resonant radius at  $r_s = 0.81r_w$  is indicated by the dashed vertical line, and lies outside of the plasma for this profile.

pulse, the electric field at the wall reaches a maximum perturbation of 0.038% of the unperturbed electric field at the wall. For this profile, the electric field perturbations at the wall are found to not decay at all. This profile is therefore named the *No Decay Profile*. A semilog plot of the envelope of the perturbed electric field at the wall versus time for this computation is shown in figure 4.8.

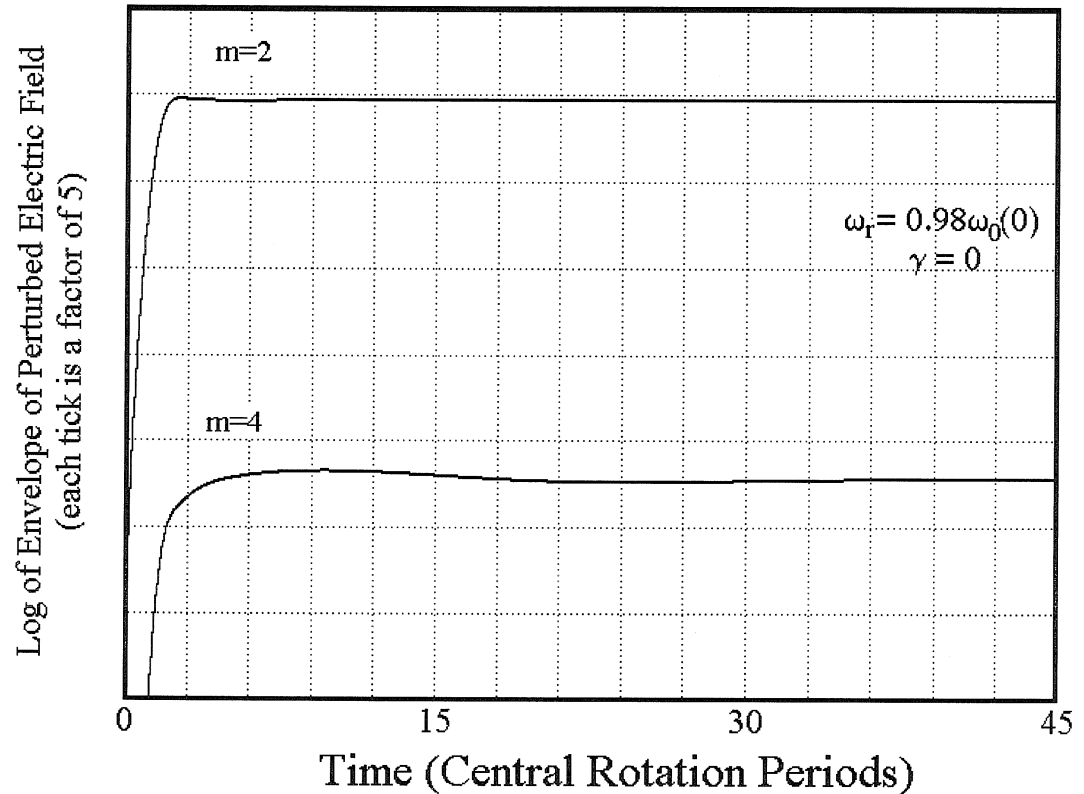


Figure 4.8: Plot of the perturbed electric field at the wall versus time on a semilog scale for the No Decay Profile  $n_0(r) = n_0(0)\{1 - 10(\frac{r}{\alpha})^6 + 15(\frac{r}{\alpha})^8 - 6(\frac{r}{\alpha})^{10}\}$  with  $\alpha = 0.8$ . This calculation uses a pure  $m = 2$  spatial excitation at the wall. The applied pulse has a Gaussian shape, reaching a maximum amplitude of  $1.18 \times 10^{-4}\phi_0$  with a FWHM of  $1.06t_{cr}$ . The perturbed  $m = 2$  electric field at the wall reaches a maximum amplitude of 0.038% of the unperturbed electric field at the wall. Each tick on the vertical axis represents a factor of 5 in amplitude. The  $m = 2$  resonant radius lies outside the plasma for this profile, and thus the perturbed electric field at the wall does not decay in time.

#### 4.2.4 Other Profiles

To study the effect density profiles with differing degrees of plasma edge “sharpness” has on the decay rate in a more systematic manner, a standard profile is chosen with one free parameter that varies the profile. This density profile is given by the Fermi function

$$n(r) = n_0(0) \frac{1}{1 + e^{\beta(4r^2-1)}}.$$

Renormalizing the equation so that  $n(0) = n_0(0)$  and  $n(1) = 0$ , the equation becomes

$$n_0(r) = n_0(0) \frac{e^{3\beta} - e^{\beta(4r^2-1)}}{(e^{3\beta} - e^{2\beta} + e^\beta - 1)(1 + e^{\beta(4r^2-1)})}. \quad (4.1)$$

This profile smoothly approaches the origin and the wall, with the maximum change in density near  $r = \frac{1}{2}r_w$ . Computations were performed with this profile for the values of  $\beta = 2, 4, 6, 8, 10, 12, 14, 16$ . The profiles are shown in figure 4.9. All computations use the same applied Gaussian pulse as described in the previous sections.

For small values of  $\beta$ , the profiles look similar to the polynomial profiles discussed earlier. As  $\beta$  increases, the profile edge becomes sharper, and the profile resembles a step function, as can be seen in figure 4.9. The sharper density profiles are found to have a higher resonant frequency and a lower decay rate compared to density profiles that change more slowly. The corresponding resonant frequencies and decay rates are summarized in table 4.1. For  $\beta = 2$ , the value for  $\frac{\omega_r}{\gamma}$  is similar to that for the Fast Decay Profile, and for  $\beta = 6$ , the value for  $\frac{\omega_r}{\gamma}$  is similar to the value for the Slow Decay Profile. The Fermi function profile with  $\beta = 8$  is used in Chapter 7, and is named the *Beat Profile*.

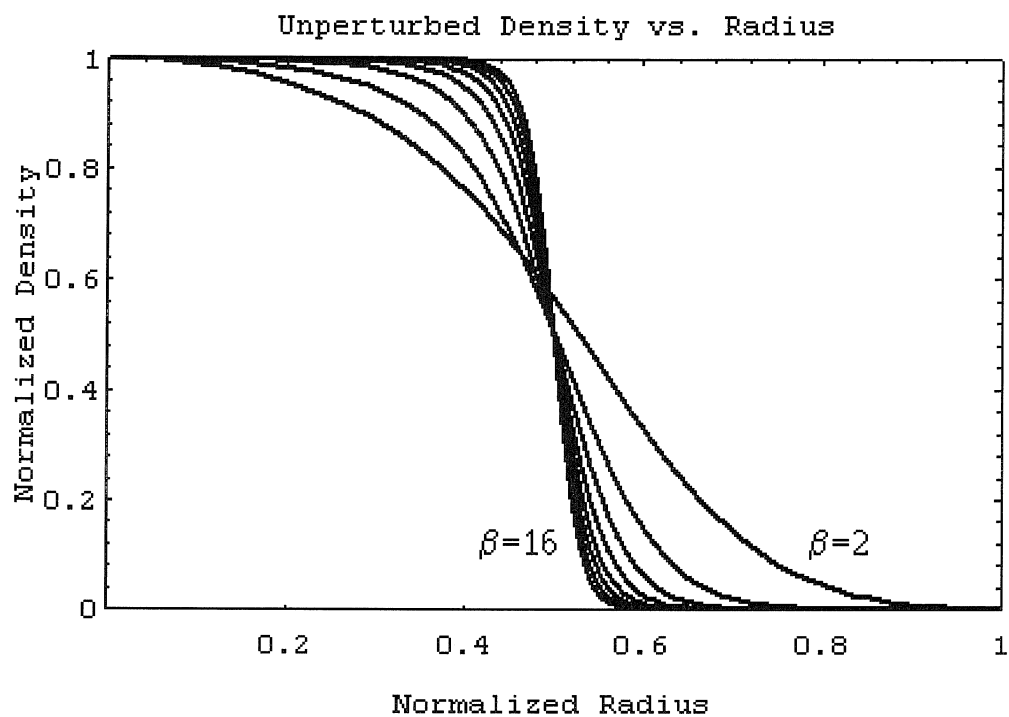


Figure 4.9: Plot of the normalized density versus radius for the normalized Fermi function with  $\beta = 2, 4, 6, 8, 10, 12, 14$ , and  $16$ .

$\beta$	$\omega_r$	$r_s$	$\gamma$	$\frac{\omega_r}{\gamma}$
2	0.870	0.825	0.0741	11.7
4	0.916	0.746	0.0314	29.2
6	0.977	0.716	0.0105	93.0
8	1.012	0.703	0.00302	335
10	1.030	0.697	$7.66 \times 10^{-4}$	1340
12	1.040	0.693	$1.76 \times 10^{-4}$	5910
14	1.046	0.691	$3.68 \times 10^{-5}$	28400
16	1.050	0.690	$6.40 \times 10^{-6}$	164000

Table 4.1: Decay Rates for Various Profiles.

#### 4.2.5 Briggs, Daugherty, and Levy Decay Rate

Briggs, Daugherty, and Levy [10] derived an approximate analytic expression for the perturbed electric potential decay rate of a pure electron plasma subjected to a small excitation with angular symmetry  $m$ . The analysis made use of results derived from a step function density profile, and assumes that the derivative of the density is small except near the radius  $r = b$ . Their formula is

$$\gamma = -\frac{\pi}{m} \frac{bn'_0(r_s)}{n_0(0)} \left| \frac{\phi(r_s)}{\phi(b)} \right|^2 \frac{[\omega_r - m\omega_0(b)]^2}{b |\omega'_0(r_s)|}$$

where  $\gamma$  is the decay rate,  $n_0(r)$  is the unperturbed density profile,  $n'_0(r)$  is the derivative of the density profile,  $\omega_0(r)$  is the unperturbed angular velocity profile,  $\omega'_0(r)$  is its derivative,  $\phi(r)$  is the perturbed electric potential,  $m$  is the azimuthal symmetry eigenvalue,  $\omega_r$  is the resonant angular frequency, and  $r_s$ , the corresponding resonant radius. Unfortunately, the quantities appearing in their expression can only be obtained from a full solution to the problem. In particular, the resonant frequency  $\omega_r$  and the corresponding resonant radius  $r_s$  are not known for a specific profile before a numerical computation is performed. Furthermore, the parameter  $b$  is not clearly defined, but will be taken as the radius where the absolute value of the derivative of the density profile is maximum. The value of  $\phi(r)$  varies with time. It is expected, though, that  $\phi(r_s)$  will have the same time dependence as  $\phi(b)$ , so the ratio  $\left| \frac{\phi(r_s)}{\phi(b)} \right|$  will be independent of time. The value for  $\phi(r)$  is taken at time  $t \sim 7.5t_{cr}$ , which is within the exponential decay range for all of these density profiles. The results from the formula for the various Fermi function profiles are summarized in table 4.2.

In this table,  $\gamma$  represents the decay rate of the perturbed potential. The column % discrepancy represents the percentage error from the measured values in table 4.1. It is found that in the best case, the formula can be within 7% of the value calculated from the Nonlinear Fluid Code. When the density profile is not similar to a step function, the formula is less accurate. The percent discrepancy in the computation with  $\beta = 16$  may be caused by inaccuracies in the fluid code, where the finite grid resolution does not accurately represent the sharp transition in density at  $r = b$ .

$\beta$	$b$	$\gamma$	$\frac{\omega_r}{\gamma}$	% discrepancy in $\frac{\omega_r}{\gamma}$
2	0.550	0.199	4.37	168%
4	0.515	0.0462	19.8	47.5%
6	0.507	0.0134	72.9	27.6%
8	0.504	0.00352	288	16.3%
10	0.503	$8.39 \times 10^{-4}$	1230	8.94%
12	0.502	$1.87 \times 10^{-4}$	5560	6.29%
14	0.501	$3.96 \times 10^{-5}$	26400	7.58%
16	0.501	$8.12 \times 10^{-6}$	129000	27.1%

Table 4.2: Comparison with Briggs decay rate for various profiles. For density profiles which deviate strongly from a step function, the Briggs decay formula is not very accurate.

## 4.3 Density Perturbations

The previous section discussed the damping in time of the perturbed electric field at the wall for a variety of different unperturbed density profiles. This section will attempt to relate the mechanism for this damping to the time dependence of the density perturbations in the plasma.

The density perturbations are small and can not be observed in images of the total density. Therefore, the average density at each radius is subtracted, leaving only the perturbations in density. In the following images, the white areas represent regions of positive density perturbation, while the black regions represent regions of negative density perturbation. The various shades of grey represent a linear scale of density perturbations.

### 4.3.1 Fast Decay Profile

As mentioned in the previous section, the density profile  $n_0(r) = n_0(0)\{1 - 3(\frac{r}{\alpha})^2 + 3(\frac{r}{\alpha})^4 - (\frac{r}{\alpha})^6\}$  with  $\alpha = 0.8$  exhibits a strong damping of the perturbed electric field at the wall. A Gaussian pulse in time is applied to the wall with  $m = 2$  azimuthal symmetry. Figure 4.10 illustrates the resulting perturbed density for six successive times.

As is seen from the figure, the initial density perturbation due to the applied

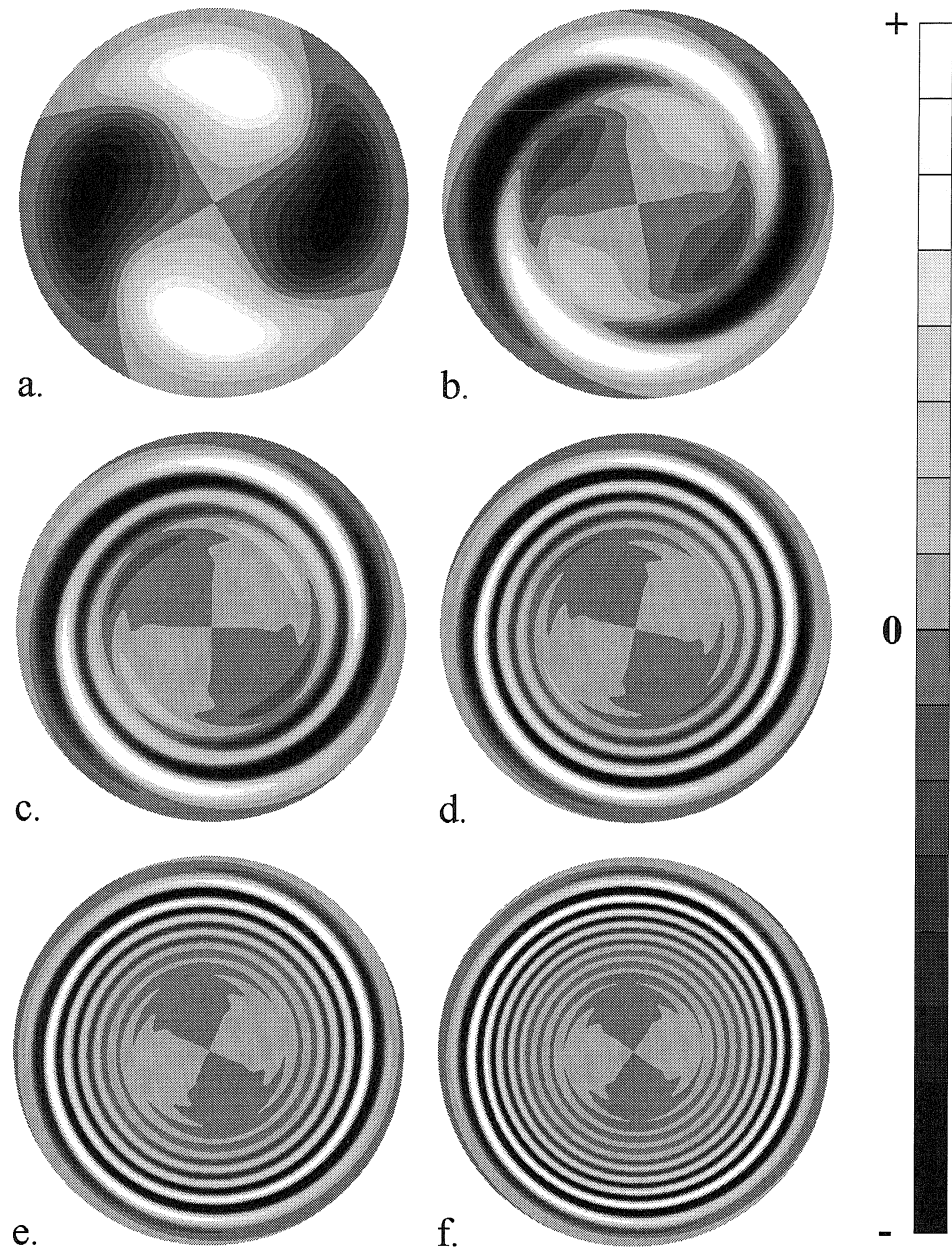


Figure 4.10: Density perturbations at six successive times for the Fast Decay Profile  $n_0(r) = n_0(0)\{1 - 3(\frac{r}{\alpha})^2 + 3(\frac{r}{\alpha})^4 - (\frac{r}{\alpha})^6\}$  with  $\alpha = 0.8$ . The white represents a high positive perturbation, while black represents an equal magnitude negative perturbation. Each successive shade represents an equal change in perturbed density, with lines between shades representing constant perturbed density contours. Between frames, the plasma rotates clockwise slightly more than half a revolution. As the perturbation phase mixes, the contribution to the perturbed electric field at the wall decays exponentially.

pulse is convected in the theta direction at different rates for different radii. This shearing causes the density perturbation at each radius to become out of phase. As time progresses, alternating bands of positive and negative density perturbation become thinner and more evenly distributed, and thus the collective contribution to the perturbed electric field at the wall rapidly decays away in time. The density perturbations persist, even though the perturbed electric field at the wall decays because of this phase mixing.

It should be noted that there are density perturbations which remain in phase, visible near the central region of the plasma. Even though it is difficult to see, there is a coherent mode extending throughout the plasma. The outer region that is mixing has a perturbed magnitude that varies with the same phase as this coherent mode. The positive and negative density perturbations are slightly stronger in the areas in phase with the wave, even though the perturbation is being mixed. As time progresses, the coherent central region does slowly mix.

For comparison to the results from the computation, figure 4.11 is a plot of the density perturbations for different times if the layers merely convected in the theta direction at their unperturbed angular velocity,  $\omega_0(r) = \omega_0(0)\{1 - \frac{3}{2}(\frac{r}{\alpha})^2 + (\frac{r}{\alpha})^4 - \frac{1}{4}(\frac{r}{\alpha})^6\}$ . This ignores the requirement for a self consistent perturbed electric field, and thus this figure does not display a collective coherent effect. Comparing the two figures, the coherent portion of figure 4.10 should be clear. Further discussion of the coherent portion versus the shearing portion of the density perturbation will be left to a later section in this chapter.

### 4.3.2 Slow Decay Profile

Figure 4.12 illustrates the density perturbations due to an  $m = 2$  Gaussian pulse of voltage on the wall for six successive times for the Slow Decay Profile,  $n_0(r) = n_0(0)\{1 - 6(\frac{r}{\alpha})^4 + 8(\frac{r}{\alpha})^6 - 3(\frac{r}{\alpha})^8\}$  with  $\alpha = 0.8$ .

In comparing figure 4.12 with figure 4.10 for the Fast Decay Profile, it is clear that the collective coherent portion of the density perturbation is much stronger for

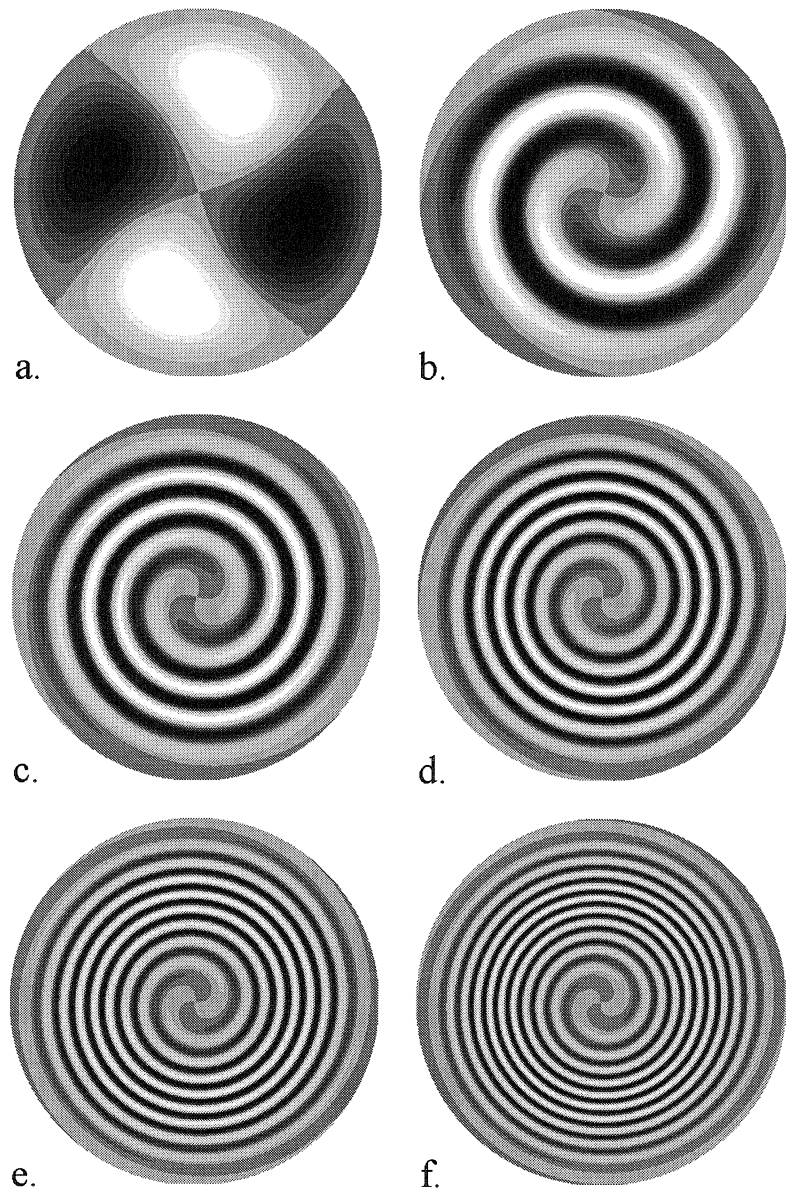


Figure 4.11: Density perturbations at six successive times for the Fast Decay Profile  $n_0(r) = n_0(0)\{1 - 3(\frac{r}{\alpha})^2 + 3(\frac{r}{\alpha})^4 - (\frac{r}{\alpha})^6\}$  with  $\alpha = 0.8$ , assuming the plasma convected in the theta direction at the unperturbed angular velocity, ignoring the self consistent perturbed electric field.

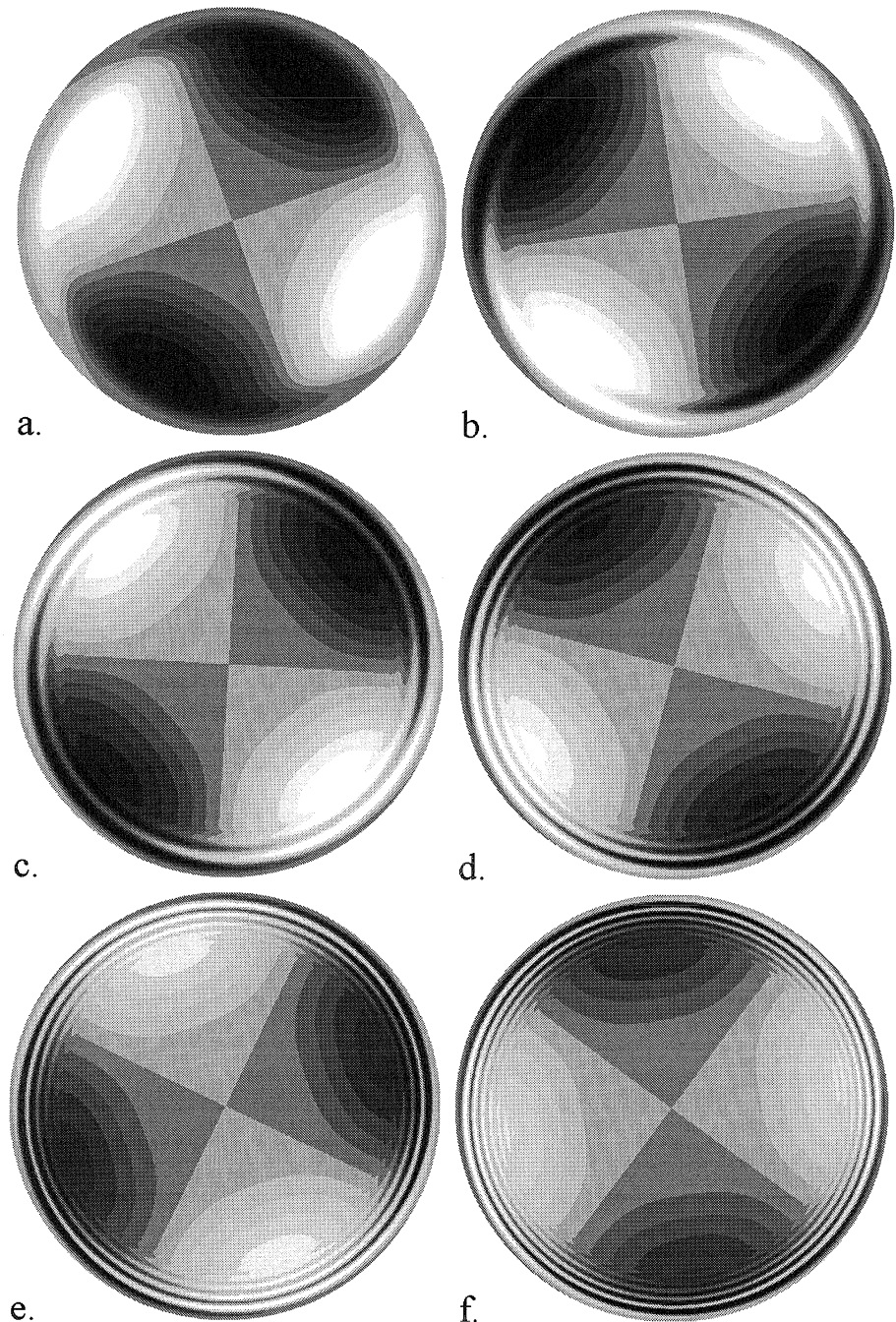


Figure 4.12: Density perturbations at six successive times for the Slow Decay Profile  $n_0(r) = n_0(0)\{1 - 6(\frac{r}{\alpha})^4 + 8(\frac{r}{\alpha})^6 - 3(\frac{r}{\alpha})^8\}$  with  $\alpha = 0.8$ . The white represents a high positive perturbation, while black represents an equal magnitude negative perturbation. Each successive shade represents an equal change in perturbed density, with lines between shades representing constant perturbed density contours.

the Slow Decay Profile than for the Fast Decay Profile. As time progresses, the coherent density perturbation slowly decays, and the shearing component becomes more evident, slowly progressing towards the center of the plasma.

### 4.3.3 No Decay Profile

As a final comparison, figure 4.13 illustrates the time evolution of density perturbations for the No Decay Profile,  $n_0(r) = n_0(0)\{1 - 10(\frac{r}{\alpha})^6 + 15(\frac{r}{\alpha})^8 - 6(\frac{r}{\alpha})^{10}\}$  with  $\alpha = 0.8$  after application of an  $m = 2$  Gaussian pulse of voltage applied to the wall.

For this profile, the coherent collective density perturbation does not decay in time. However, the shearing component still has an observable effect in the plasma. The shearing mode does break the density perturbations into filaments, but the collective mode does not allow these filaments to wrap around and mix as with the previous two density profiles.

## 4.4 Linear Model

This section presents a simple approximation based on two exponentials which helps understand the behavior of the perturbed density as a function of time. In section 4.2, the perturbed electric field at the wall was found to decay exponentially in time after excitation from an externally applied pulse. This exponential decay after the applied pulse can be modeled in the transformed space as a simple pole in the complex plane [19]. This pole is located at

$$\omega^* = \omega_r - i\gamma$$

where  $\omega^*$  is the complex pole,  $\omega_r$  is the real resonant frequency, and  $\gamma$  is the decay rate. Rewriting the linearized fluid equations 2.14 and 2.15 from Chapter 2 we have

$$\tilde{n}_{1,m}(r, \omega) = \frac{m}{r(m\omega_0(r) - \omega)} \frac{dn_0(r)}{dr} \tilde{\phi}_1 \quad (4.2)$$

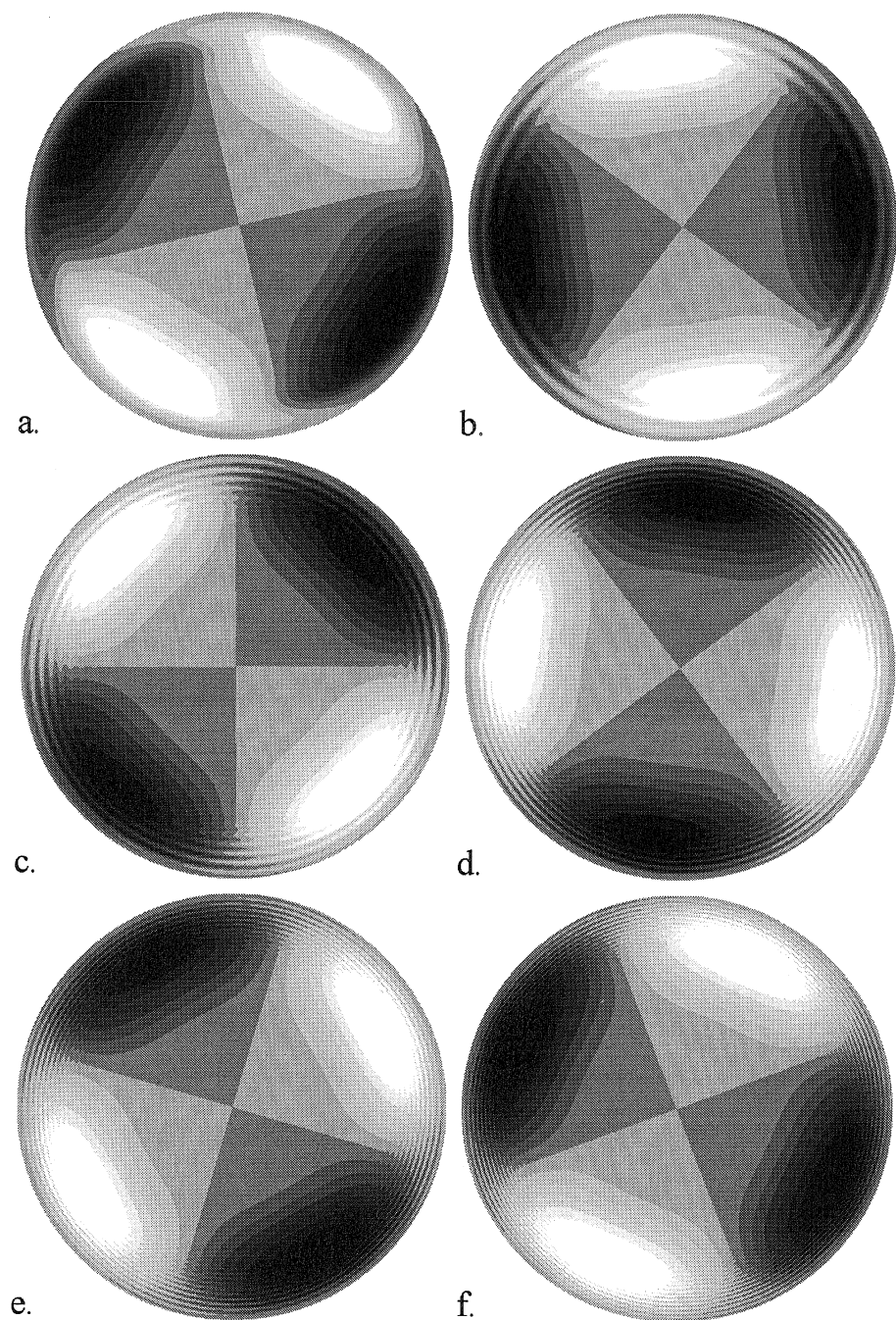


Figure 4.13: Density perturbations at six successive times for the No Decay Profile  $n_0(r) = n_0(0)\{1 - 10(\frac{r}{\alpha})^6 + 15(\frac{r}{\alpha})^8 - 6(\frac{r}{\alpha})^{10}\}$  with  $\alpha = 0.8$ . The white represents a high positive perturbation, while black represents an equal magnitude negative perturbation. Each successive shade represents an equal change in perturbed density, with lines between shades representing constant perturbed density contours.

$$\frac{d^2\tilde{\phi}_{1,m}}{dr^2} + \frac{1}{r} \frac{d\tilde{\phi}_{1,m}}{dr} - \left[ \frac{m^2}{r^2} + \frac{m}{r(m\omega_0(r) - \omega)} \frac{dn_0(r)}{dr} \right] \tilde{\phi}_{1,m} = 0$$

which can be solved for the transformed perturbed density  $\tilde{n}_{1,m}(r, \omega)$  and potential  $\tilde{\phi}_{1,m}(r, \omega)$ . Using the simple pole approximation for the transformed perturbed potential, the approximate solution takes the form

$$\tilde{\phi}_{1,m}(r, \omega) = \frac{A_m(r, \omega)}{\omega - \omega^*}. \quad (4.3)$$

This approximation is useful after the applied pulse has been turned off, and during the time the decay is exponential. The function  $A_m(r, \omega)$  is the solution to the equation with the simple pole at  $\omega^*$  removed. It is assumed that the pole is the dominant feature, and the features of the function  $A_m(r, \omega)$  are small compared to this pole.

Inserting this form for the perturbed potential 4.3 into the equation for the perturbed density 4.2 we get

$$\tilde{n}_{1,m}(r, \omega) = \frac{m}{r(m\omega_0(r) - \omega)} \frac{dn_0(r)}{dr} \frac{A_m(r, \omega)}{\omega - \omega^*}$$

or absorbing some of the constants and functions of  $r$  into a new function  $C(r, \omega)$  we obtain

$$\tilde{n}_{1,m}(r, \omega) = C(r, \omega) \frac{1}{\omega - \omega^*} \frac{1}{\omega - m\omega_0(r)}.$$

Performing an inverse Laplace transform on the perturbed density results in

$$n_{1,m}(r, t) = D_q(r) e^{-i\omega^* t} + D_c(r) e^{-im\omega_0(r)t}$$

which can also be written as

$$n_{1,m}(r, t) = D_q(r) e^{-\gamma t} e^{-i\omega_r t} + D_c(r) e^{-im\omega_0(r)t}. \quad (4.4)$$

This form for the perturbed density is comprised of two components. The first term is a collective coherent mode with resonant frequency  $\omega_r$  which decays exponentially. This collective coherent mode which decays will be taken as the *quasimode* [15][19]. The radial dependence of the quasimode has been lumped into the coefficient  $D_q(r)$ . The second term does not decay in time. It is also not coherent, but rather has a frequency that is a function of the radius, and therefore a resulting shear. Since the frequency is a continuous function of the radius, this term describes the *continuum modes*. The radial dependence of the continuum modes has been incorporated into the coefficient  $D_c(r)$ .

This model contains several features. If the quasimode term is larger than the continuum term, the quasimode will dominate the perturbed density early in time. However, as the quasimode decays, the continuum modes will become more apparent in the perturbed density. At some time and at some radius, the two terms should be comparable, and an interference pattern should be visible. Looking back at figure 4.10 and figure 4.12, there is a visible interference between these two modes occurring near the radius that separates region that is sheared and region that is coherent.

To further illustrate the interference between the two modes, figure 4.14 plots the magnitude of the  $m = 2$  density perturbations versus radius for the computation using the Fast Decay Profile. The frames (a)-(f) represent the same times used in figure 4.10.

From this plot, the interference pattern is clearly visible. Additionally, the decay of the quasimode is also visible as the maximum amplitude decays from frame (a) to frame (f). After the quasimode has decayed, the remaining contribution is from the continuum modes, which do not decay in time. In frame (f), the quasimode has nearly decayed away. Figure 4.15 is the same plot of the perturbed density magnitude versus radius, but for a time much later than frame (f), where the quasimode has completely decayed away.

Figure 4.15 shows the form of the continuum mode as a function of radius, and figure 4.14(a) shows the sum of the quasimode and continuum mode early in time. It is therefore possible to use the function of figure 4.15 for the continuum term  $D_c(r)$

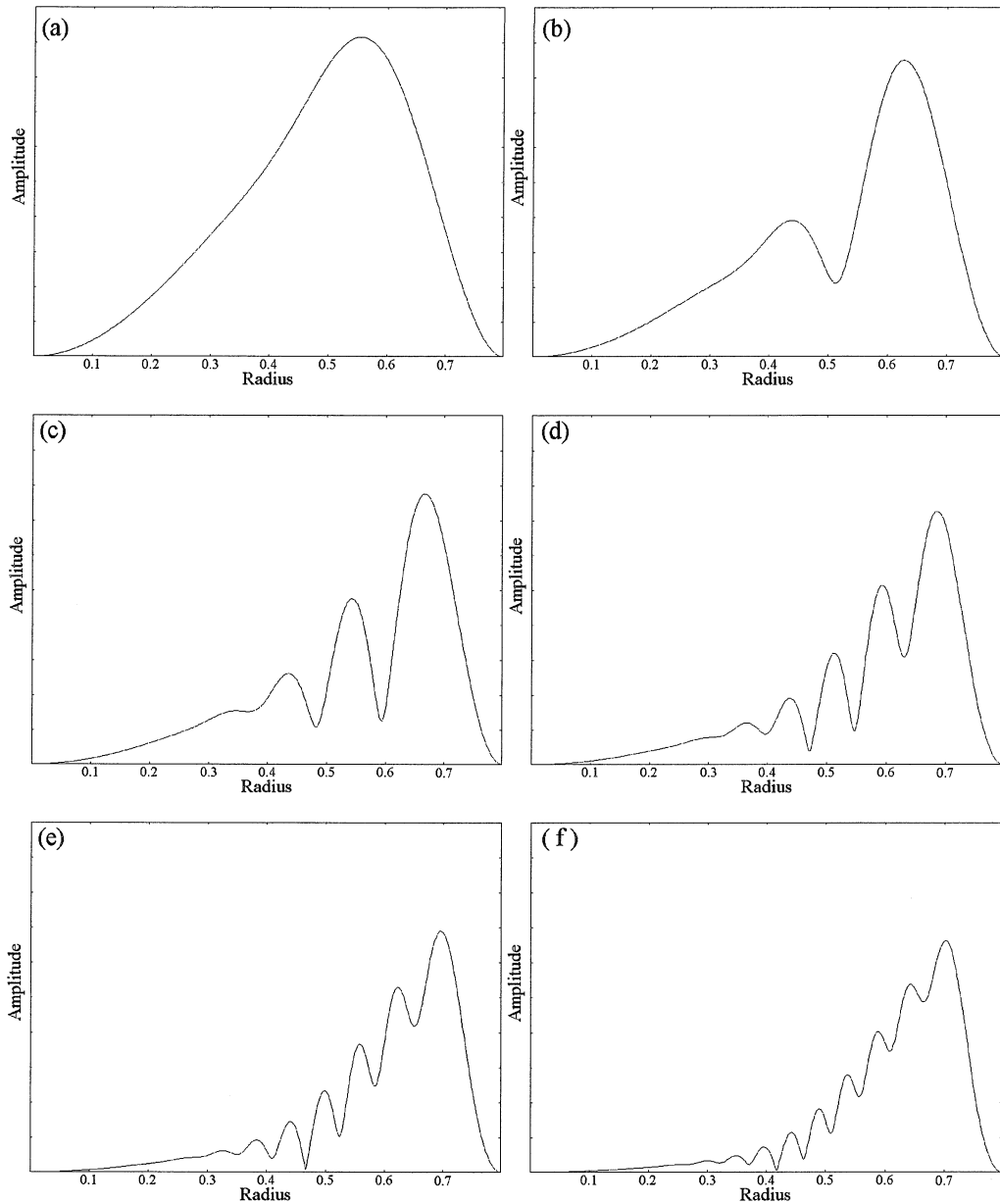


Figure 4.14: Magnitude of density perturbations versus radius at six successive times for the Fast Decay Profile. As time progresses, an interference can be seen between the quasimode and the continuum modes.

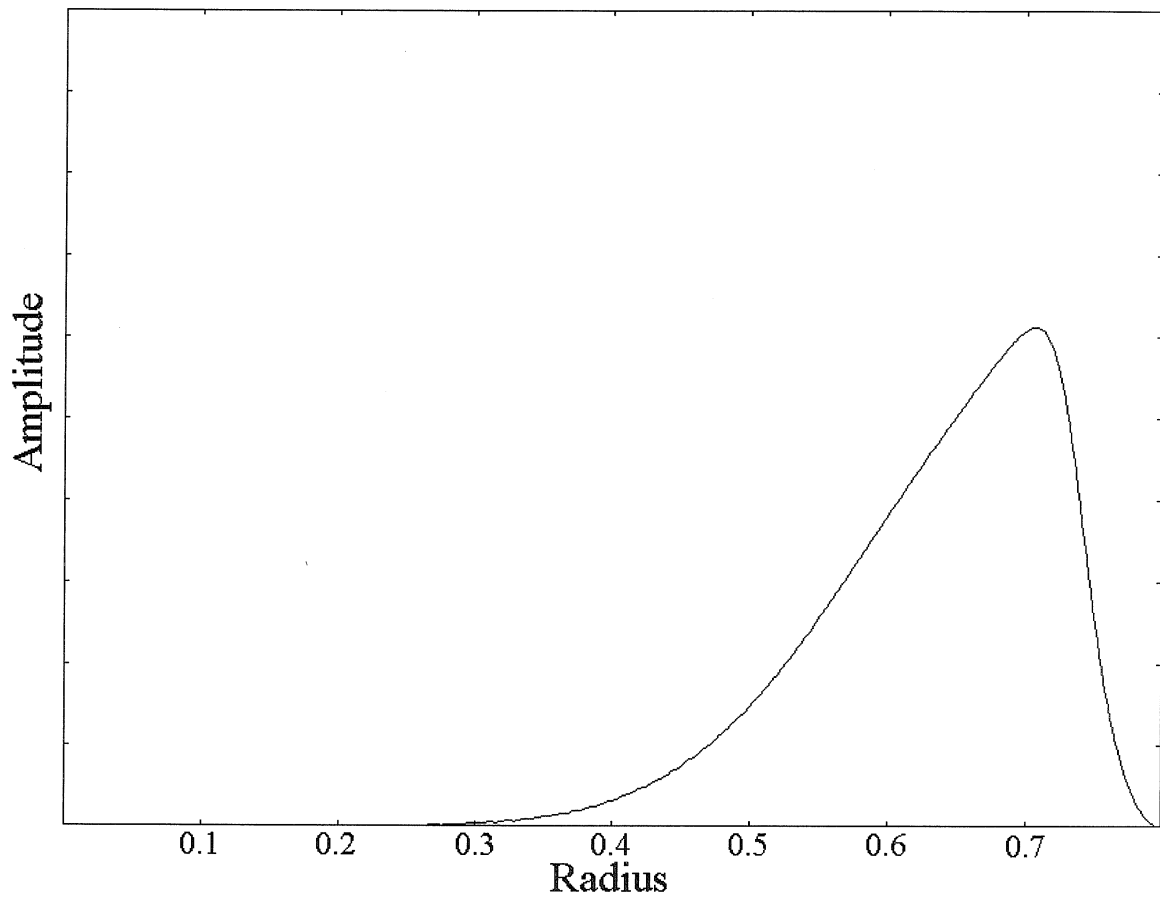


Figure 4.15: Magnitude of continuum density perturbations versus radius for the Fast Decay Profile obtained after the quasimode has decayed away.

in the linear model. Additionally, the function of figure 4.15 subtracted from the function of figure 4.14(a) can be used for the quasimode term  $D_q(r)$ . Figure 4.16 shows the resulting density perturbations at six successive times from using these two terms in the linear model. A good qualitative agreement is seen by comparing figure 4.16 to the results from the full computation in figure 4.10.

This approximate two-exponential solution for the perturbed density is successful at reproducing images of the perturbed density that agree with the results from the code. However, the decay rate of the quasimode term depends on the phase mixing caused by the continuum modes, and can not be determined for an arbitrary density profile without performing a numerical computation.

## 4.5 Conclusion

This chapter examined the response of a pure electron plasma to a small amplitude pulse applied at the wall. The response of the perturbed electric field at the wall is found to decay exponentially. The decay rate is a strong function of the unperturbed density profile, and roughly matches the approximate decay rate expression derived by Briggs, Daugherty, and Levy. However, their expression for the decay rate can not predict the decay rate for a given profile since it requires values that are not known before a computation is performed. Their expression does not agree well with the computation for density profiles which strongly deviate from a step function. For a certain class of power law profiles, Corngold has found an analytical expression for the decay rate [15].

Images of the perturbed density illustrate that the density perturbation undergoes shear. The shear in the plasma flow causes the density perturbations to become out of phase at different radii. This phase mixing causes the perturbed electric field at the wall to decay exponentially.

Application of a linear model suggests that the perturbed density can be separated into a coherent quasimode term, and a shearing continuum mode term. However, the parameters for this model must still be obtained from a complete linear calculation.

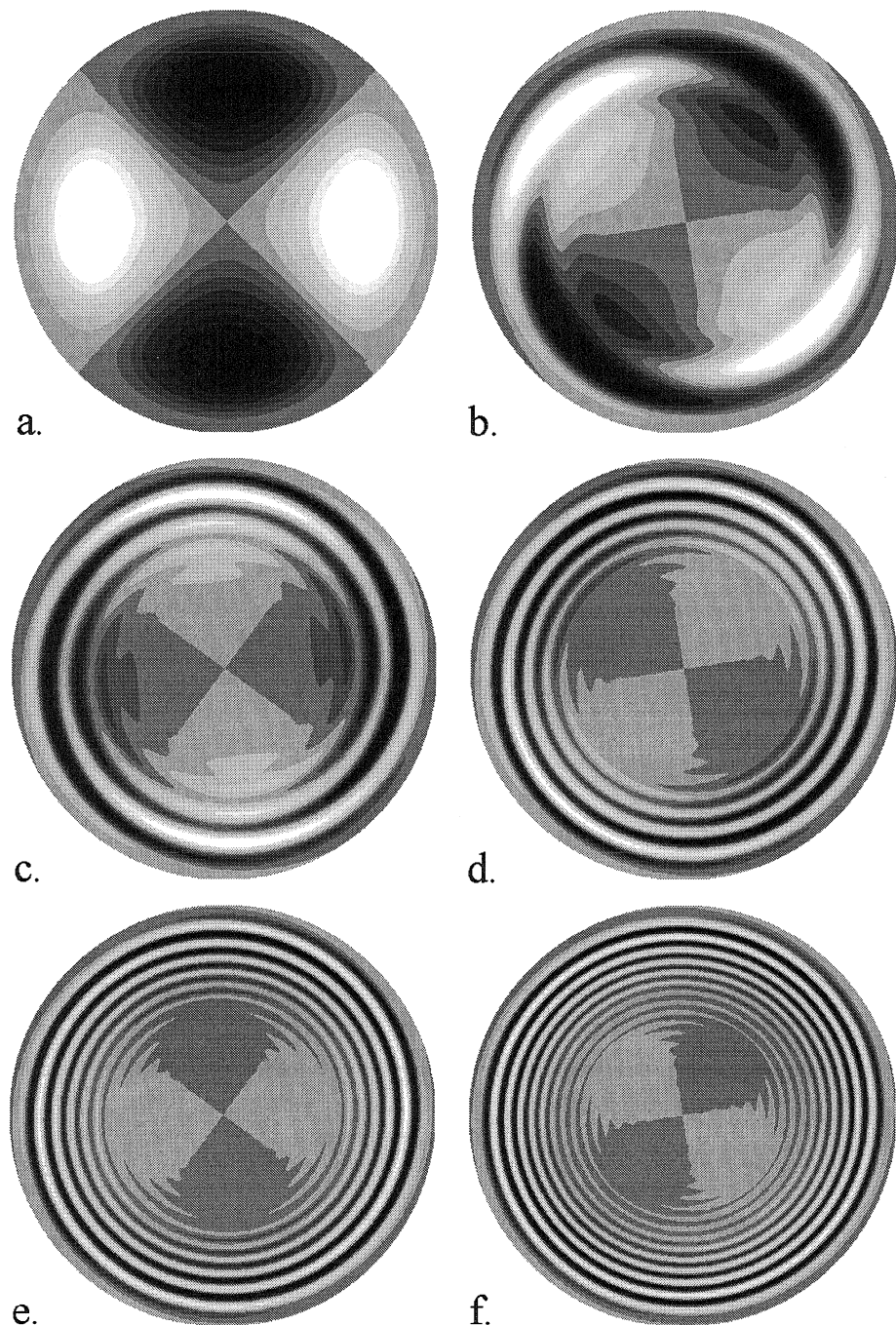


Figure 4.16: Resulting density perturbations for six different times for the Fast Decay Profile using the Quasimode and Continuum mode linear model.

Using the parameters from the linear calculation in this model enables the images of the perturbed density to be reproduced.

The Nonlinear Fluid Code successfully reproduced the results from the Linear Fluid Code for small amplitude disturbances. This provides verification of the Nonlinear Fluid Code method. This chapter studied several different density profiles. However, a systematic study of the effect of profiles on the plasma response has not been completed. The next chapter will examine the plasma response to larger amplitude pulses, where nonlinear effects become important.

# Chapter 5 Fluid Trapping

## 5.1 Introduction

Chapter 4 examined the effect of a low amplitude externally applied pulse on a pure electron plasma. The response in the perturbed electric field at the wall due to this applied pulse was found to decay exponentially. This decay was explained using linear theory, which described a phase mixing process for the perturbed density. This chapter will examine the effects of single, larger amplitude pulses, where the linear theory is no longer valid and nonlinear self-interactions become important.

Briggs, Daugherty, and Levy [10] predicted that with higher amplitude perturbations, fluid elements might be trapped in the large amplitude excited wave. Such trapping would cause a quasi-periodic modulation of the decaying amplitude of the perturbed electric field at the wall as the trapped fluid elements bounce within the potential well of the wave. According to Briggs, Daugherty, and Levy, the quasi-periodic modulation should have a bounce frequency proportional to the square root of the amplitude of the perturbed potential.

Pillai's [19] experimental data, showing the envelope of the oscillating electric field at the wall versus time on a semilog scale, is reproduced in figure 5.1. He found that for small amplitude applied pulses, the perturbed electric field at the wall decayed approximately exponentially. For higher amplitude pulses, a modulation of the decay envelope occurred with a bounce frequency dependence proportional to the square root of the amplitude, agreeing with the bounce frequency dependence on wave amplitude predicted by Briggs, Daugherty, and Levy [10]. Because of this agreement with the Briggs prediction, Pillai attributed the envelope modulation to trapping of fluid elements. Since there was no diagnostic in the experiment to measure the density distribution directly, these trapped fluid elements could not be directly observed.

In order to show that trapped fluid elements are responsible for the modulation

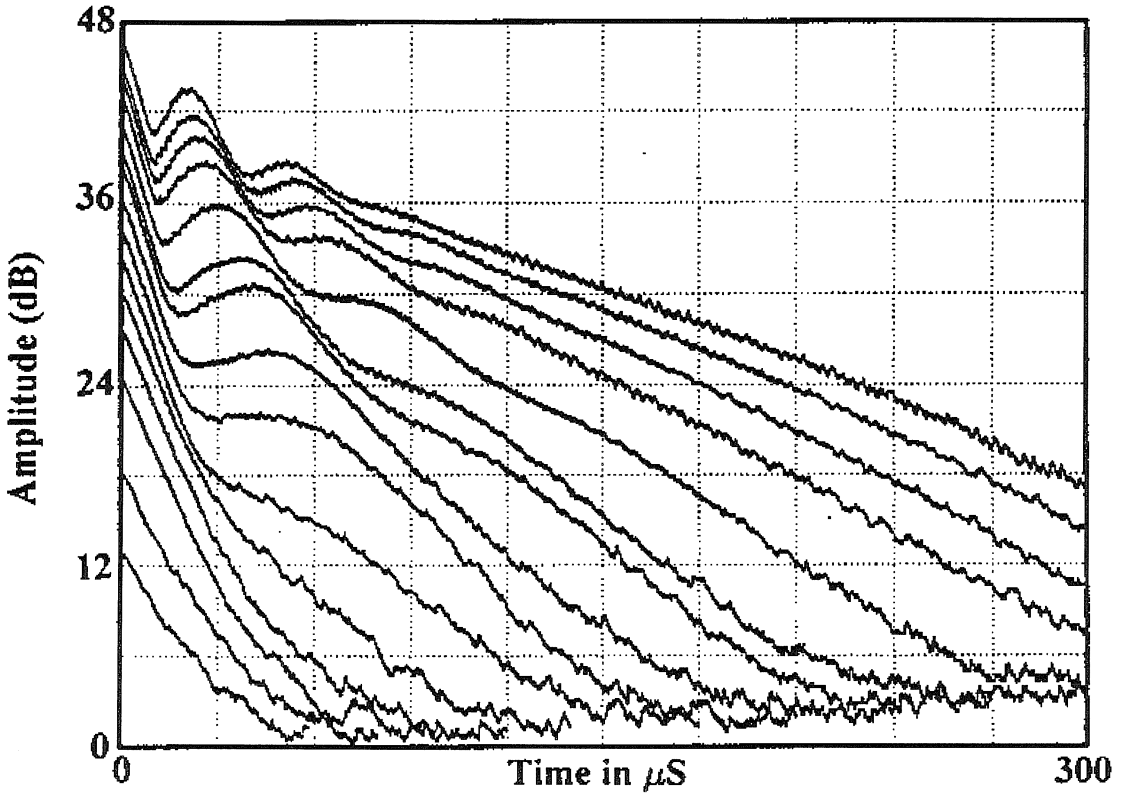


Figure 5.1: Plot of the envelope of the perturbed electric field at the wall versus time on a semilog scale for the experimental data collected by N. Sateesh Pillai. The applied  $m = 2$  excitation voltage ranges from 10 mV for the lowest amplitude pulse, to 1000 mV for the highest amplitude trace. The vertical scale is calibrated in dB.

of the decay envelope, the nonlinear 2-D cylindrical fluid code is used to study the response of a pure electron plasma to higher amplitude pulses. The results from the fluid code qualitatively agree with the experimental results. For low amplitude perturbations, the envelope of the oscillating electric field at the wall decays exponentially. For larger perturbations, a bounce oscillation is observed in the decaying envelope. The bounce modulation is caused by fluid elements that are trapped in the wave. The trapped fluid elements are directly observed in images of the perturbed density. For a perturbation that is slowly applied to the wall, a non-decaying wave without bounce oscillations is excited, which is similar to a BGK mode [20]. A BGK mode is a large amplitude mode that contains regions of plasma trapped within the

excited wave, and is stationary in a frame rotating with the wave.

## 5.2 Fluid Code Results

This section describes results from the Nonlinear Fluid Code for pulses applied to the Slow Decay Profile. The results are observed in the perturbed electric field at the wall, and in images of the perturbed density. The Slow Decay Profile,  $n_0(r) = n_0(0)\{1 - 6(\frac{r}{\alpha})^4 + 8(\frac{r}{\alpha})^6 - 3(\frac{r}{\alpha})^8\}$ , with  $\alpha = 0.8$ , previously discussed in Chapter 4, was chosen because its decay rate closely matches the experiment above for small amplitude applied pulses. This density profile may resemble the density profile in the experiment. This profile has a central electric potential of  $\phi_0 = -0.142696\frac{e}{\epsilon_0}n_0(0)r_w^2$ , and an unperturbed electric field at the wall of  $-0.128\frac{e}{\epsilon_0}n_0(0)r_w$ .

### 5.2.1 Perturbed Electric Field

This section describes the perturbed electric field at the wall resulting from pulses applied to the slow decay profile. The electric field at the wall is systematically studied as a function of applied pulse amplitude.

The 2-D cylindrical fluid code is used to study the response of a pure electron plasma to an externally applied pulse. A low amplitude sinusoidal pulse was applied for three cycles with an amplitude of  $4.28 \times 10^{-5}\phi_0$ . The resulting perturbed electric field at the wall reaches a maximum amplitude of 0.00421% of the unperturbed electric field at the wall and decays exponentially in time. The perturbed electric field at the wall versus time is plotted in figure 5.2.

As seen in the figure, the response from this applied pulse decays exponentially. The pulse amplitude is in the linear regime, so that the results of Chapter 4 are valid for an applied pulse with this amplitude. This computation is similar to a computation in Chapter 4, where a semilog plot of the envelope of the perturbed electric field versus time for this computation was shown in figure 4.6.

For comparison, figure 5.3 is a plot of the perturbed electric field at the wall versus time for an applied pulse amplitude that is 200 times higher, with a three cycle pulse

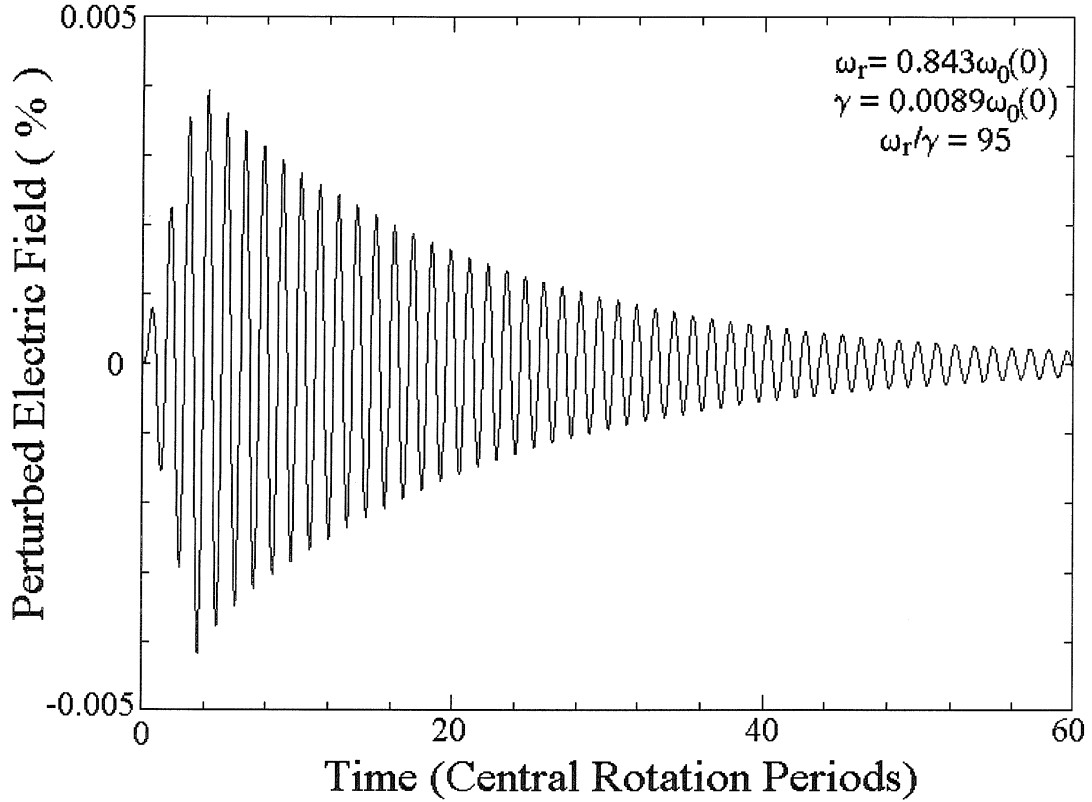


Figure 5.2: Plot of the perturbed electric field at the wall for the Slow Decay Profile, using an applied three cycle pulse amplitude of  $4.28 \times 10^{-5} \phi_0$ . The perturbed electric field at the wall reaches a maximum amplitude of 0.00421% of the unperturbed electric field at the wall and decays exponentially in time.

amplitude of  $8.55 \times 10^{-3} \phi_0$ . For this applied pulse, the perturbed electric field reaches a maximum amplitude of 0.851% of the unperturbed electric field at the wall.

The plasma response at the wall is quite different from the previous lower amplitude example. For this higher amplitude applied pulse, the decay rate has been reduced. Also, a bounce modulation of the decay envelope is evident.

A systematic study of the dependence on amplitude was made for this profile, varying the amplitude of the initial three cycle pulse. The highest amplitude case has an applied pulse amplitude of  $0.0214 \phi_0$  causing a perturbation in the electric field at the wall of 2.07%. The lowest has an applied pulse amplitude of  $1.07 \times 10^{-4} \phi_0$

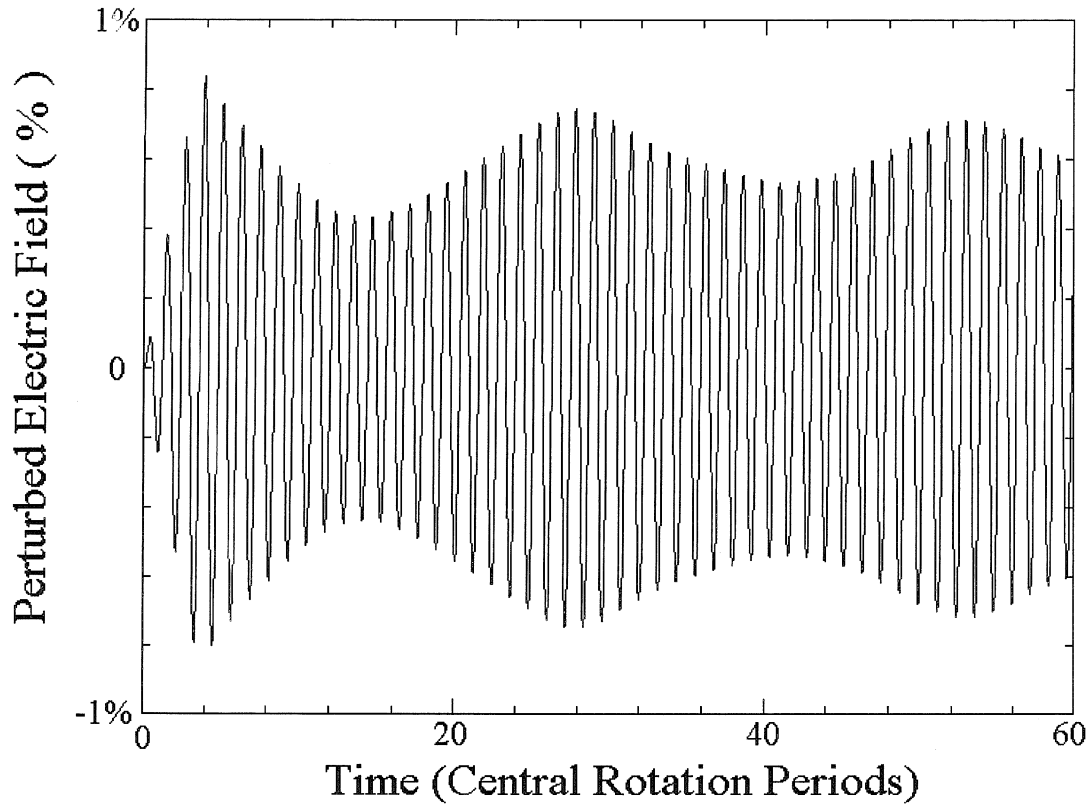


Figure 5.3: Plot of the perturbed electric field at the wall demonstrating bounce oscillations. A three cycle pulse with an amplitude of  $8.55 \times 10^{-3} \phi_0$  is applied to the Slow Decay Profile. The perturbed electric field reaches a maximum amplitude of 0.851% of the unperturbed electric field at the wall.

leading to a maximum response of 0.0105% of the unperturbed electric field at the wall. The logarithm of the envelope of the perturbed electric field of the wall versus time is plotted in figure 5.4.

As seen in the figure, the lower amplitude traces decay exponentially. At higher amplitudes, the perturbed electric field at the wall has a lower decay rate. Additionally, a modulation of the decay envelope occurs. The time scale for this plot was chosen for easy comparison with the experimental data in figure 5.1. The calculation is terminated after 60 central rotations because of computational time and accumulation of errors.

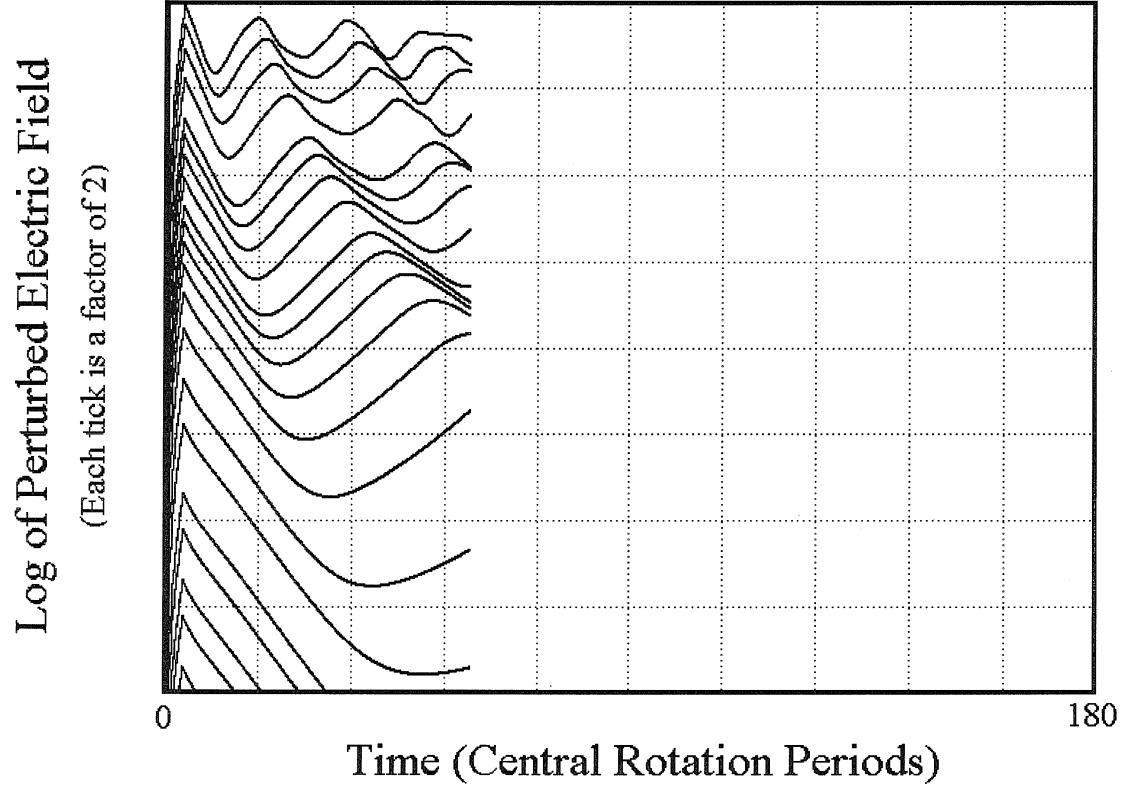


Figure 5.4: Plot of the envelope of the perturbed electric field versus time on a semilog scale for various amplitude pulses applied to the Slow Decay Profile. The highest amplitude case has an applied three cycle pulse amplitude of  $0.0214\phi_0$  causing a perturbation in the electric field at the wall of 2.07%. The lowest has an applied pulse amplitude of  $1.07 \times 10^{-4}\phi_0$  leading to a maximum response of 0.0105% of the unperturbed electric field at the wall. The lower amplitude traces show an exponential decay, while the higher amplitude traces show a modulation of the decay envelope. The computations were terminated after 60 central rotations due to computational time and accumulation of errors.

In comparing the computational data of figure 5.4 to the experimental data of figure 5.1, these two figures exhibit remarkable similarities. Both traces have the same low amplitude decay rate. This is expected as the slow decay density profile was chosen to have the same low amplitude decay rate as the experiment. As the amplitude is increased, both the experimental data and the computation show a decrease in the decay rate and a modulation of the decay envelope.

The modulation frequency does, however, differ between the results from the computation and the results from the experiment. Additionally, the decay rates differ at higher amplitudes. The difference is probably due to imperfect knowledge of the experimental density profile. In the experiment, no direct measurement could be made of the radial dependence of the density. The Slow Decay Profile was chosen to match the experimental decay rate at low amplitudes, but this profile is not unique. Additionally, other effects such as viscosity which are not included in the fluid code may also be responsible for the discrepancy.

Since there is a good qualitative agreement between the experiment and computation, it is expected that the fluid code contains the physics responsible for the bounce oscillation found in the experimental data.

### 5.2.2 Bounce Frequency Dependence

According to Briggs, Daugherty, and Levy [10], the quasi-periodic modulation should have an angular frequency given by the formula

$$\omega_b^2 = m^2 \frac{\phi_1(r_s)}{r_s} \left. \frac{d\omega_0(r)}{dr} \right|_{r=r_s} \quad (5.1)$$

where  $\omega_b$  is the bounce oscillation angular frequency,  $m$  is the azimuthal symmetry eigenvalue,  $r_s$  is the resonant radius,  $\phi_1(r)$  is the perturbed electric potential, and  $\omega_0(r)$  is the unperturbed angular velocity profile. This formula predicts that the bounce frequency should be proportional to the square root of the amplitude of the perturbed potential. As with their linear decay formula, the other factors are difficult to determine, but they are assumed not to change when the potential is varied.

Some features of this bounce formula may be easily understood by considering a one dimensional model of a particle in a potential  $\phi = \phi_0 \cos(m\theta)$ . The electric field  $E = -m\phi_0 \sin(m\theta)$ , and the force  $F = qE$ , where  $q$  is the electric charge of the particle. Using Newton's second law, linearizing around  $\theta = 0$ , and solving the differential equation results in periodic motion with a frequency  $\omega_b \sim m\sqrt{\phi_0}$ .

In figure 5.4, the 12 higher amplitude plots complete at least one half period of bounce oscillation. From these plots, a bounce angular frequency can be determined, which can then be compared to the square root relationship above.

Some care must be taken when calculating the bounce frequency. The modulation of the decay envelope is imposed on a decaying exponential. To obtain the maxima and minima of the oscillation, a straight line was fit to the logarithm of the perturbed electric field at the wall for each trace to obtain a decay rate. Then this exponential decay was subtracted from the data, leaving the modulating envelope. The time between the first minimum and the next maximum, corresponding to half a bounce period, was used to calculate the bounce frequency.

Additionally, the perturbed potential used for each trace is calculated in a specific manner. Equation 5.1 requires the electric potential at the resonant radius. The perturbed potential is assumed to be proportional to the perturbed electric field at the wall. During a bounce oscillation, the perturbed electric field at the wall decays exponentially. Therefore, the perturbed electric field used for comparison to equation 5.1 was averaged over the time of the half bounce period between the first minimum and the next maximum.

Using the calculated bounce angular frequency and the averaged perturbed potential during this bounce oscillation, a plot was made on a log-log scale of the bounce frequency versus perturbed amplitude for the 12 high amplitude traces of figure 5.4. This plot is shown in figure 5.5.

On this log-log scale, the points fall along a straight line. The dashed line has a slope of 0.5. A least squares fit through the data points gives a slope of  $0.493 \pm 0.008$ . This indicates that the bounce frequency is proportional to the square root of the perturbed electric field at the wall.

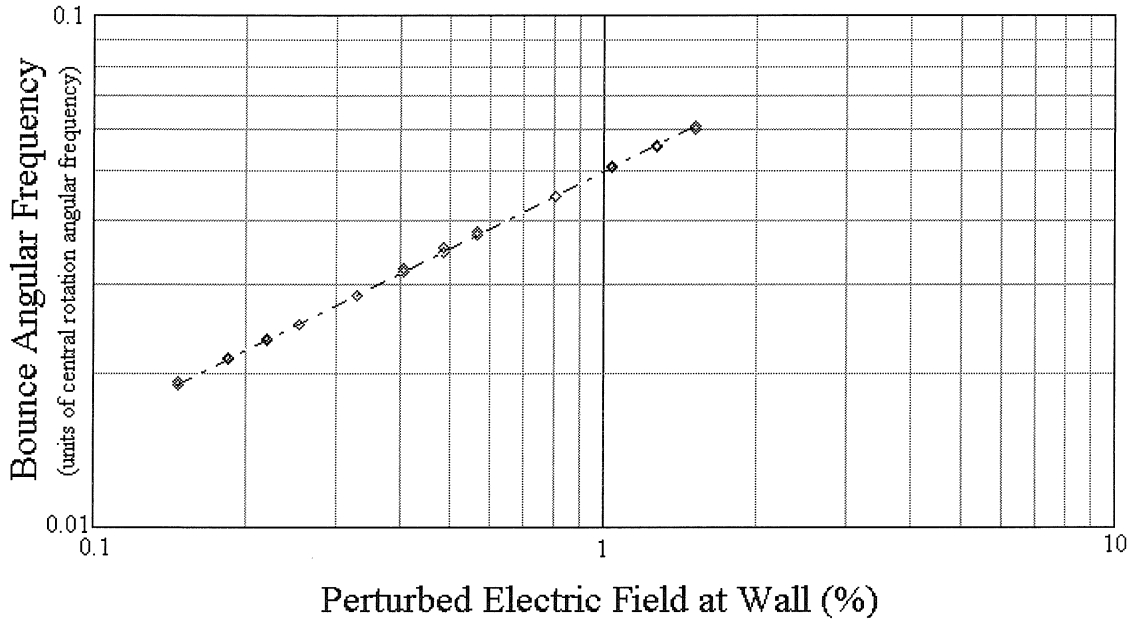


Figure 5.5: Plot of the angular bounce frequency versus the perturbed electric field at the wall for 12 high amplitude traces. The dashed line has a slope of 0.5, indicating that the bounce frequency is proportional to the square root of the perturbed electric field at the wall.

Agreement of the computation with the square root relationship suggests that the modulation of the decay envelope is due to the trapping of fluid elements. The next section will describe a search for these trapped fluid elements directly by observing images of the perturbed density.

### 5.2.3 Density Perturbations

This section describes images of the density and perturbed density resulting from application of an external pulse to the Slow Decay Profile. The pulse has an amplitude sufficiently large to cause a modulation of the decay envelope.

A slightly different external pulse is applied to the Slow Decay Profile. A Gaussian pulse shape is applied in the frame moving with the wave, having an  $m = 2$  resonant frequency of  $0.851\omega_0(0)$ . The applied pulse has a maximum amplitude of  $0.005\phi_0$ , and a FWHM of  $1.06t_{cr}$ . The resulting perturbed electric field at the wall reaches a

maximum perturbed amplitude of 1.18% of the unperturbed electric field at the wall. A plot of the envelope of the perturbed electric field at the wall for this computation is shown in figure 5.6.

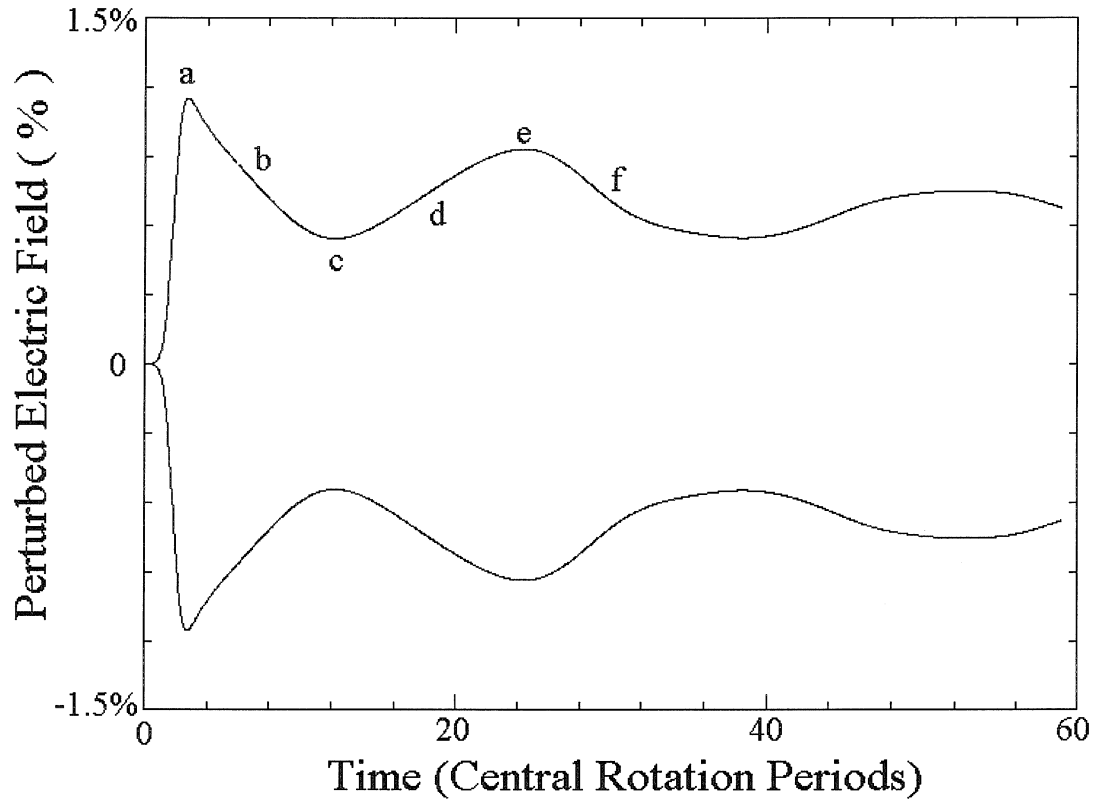


Figure 5.6: Plot of the envelope of the perturbed electric field at the wall for a typical computation displaying bounce oscillations. The applied pulse has a Gaussian pulse shape, reaching a maximum amplitude of  $0.005\phi_0$ , and a FWHM of  $1.06t_{cr}$ . The letters (a)-(f) correspond to times  $2.65t_{cr}$ ,  $7.36t_{cr}$ ,  $12.1t_{cr}$ ,  $18.3t_{cr}$ ,  $24.4t_{cr}$ , and  $31.5t_{cr}$ , respectively. The perturbed field reaches a maximum amplitude of 1.18% of the unperturbed electric field at the wall. The bounce oscillation has an angular frequency of  $\omega_b = 0.0407\omega_0(0)$ .

As seen from the figure, the perturbed electric field at the wall exhibits a strong bounce oscillation. The bounce oscillation modulates the decay envelope with a maximum modulation of 52.9% at an angular frequency of  $\omega_b = 0.0407\omega_0(0)$ . The next section will look at images of the density to see if this modulation can be observed.

## Total Density

This section describes images of the density resulting from the application of the pulse described in the above section. In the described computation, the perturbation is large enough for nonlinear effects to occur. The perturbed electric field at the wall is greater than 1%, and nonlinear bounce oscillations are observed. It might be expected that an observable effect could be seen in the total density of the plasma. Figure 5.7 shows images of the total density of the plasma at six different times in the reference frame that is rotating with the wave.

Images (a) - (f) in figure 5.7 correspond to the total density at times  $2.65t_{cr}$ ,  $7.36t_{cr}$ ,  $12.1t_{cr}$ ,  $18.3t_{cr}$ ,  $24.4t_{cr}$ , and  $31.5t_{cr}$ , respectively. These times correspond to covering the duration of the first bounce cycle, labeled (a)-(f) in figure 5.6.

As seen in the figure, very little difference can be seen between the different frames for the total density picture. Even the initial strong perturbation is barely visible, giving the total density a very slight elliptical shape. This indicates that even though nonlinear bounce oscillations are observed, the amplitude of the perturbation is not so high as to significantly distort the shape of the plasma from the unperturbed configuration. In other words, nonlinear effects may occur at amplitudes that hardly distort the plasma.

## Perturbed Density

Since the density perturbation is too small to be seen in the total density, images of the perturbed density are plotted in figure 5.8. These images are generated by subtracting the unperturbed density, revealing the difference of the density from the unperturbed density. The times for each frames are the same times used in figure 5.7.

The perturbed density in figure 5.8 shows structure and variation that could not be seen in images of the total density. Some of the structure is similar to that found in figure 4.12 from Chapter 4, which shows images of the perturbed density (without the gap to the wall) at different times after excitation from a low amplitude applied pulse. This similarity in structure is due to the same decay mechanism that exists

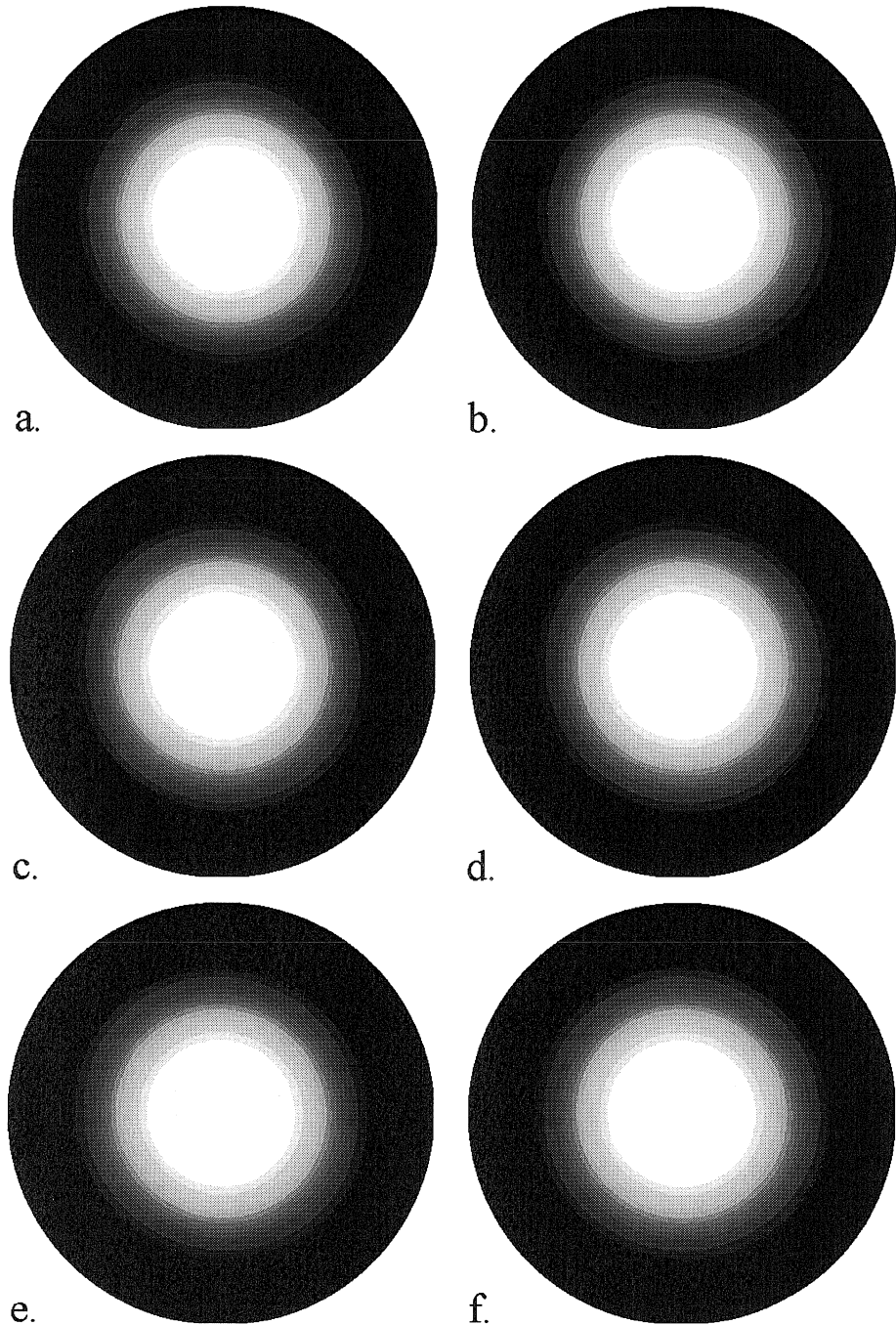


Figure 5.7: Images of the total density at six different times. An external Gaussian pulse with a maximum amplitude of  $0.005\phi_0$ , and a FWHM of  $1.06t_{cr}$  is applied to the Slow Decay Profile. The resulting perturbed electric field at the wall exhibits strong bounce oscillations. Figures (a)-(f) correspond to times  $2.65t_{cr}$ ,  $7.36t_{cr}$ ,  $12.1t_{cr}$ ,  $18.3t_{cr}$ ,  $24.4t_{cr}$  and  $31.5t_{cr}$ , respectively. The white region represents an area of high density, and the black area represents a region of low density. Very little change is visible in the total density pictures.

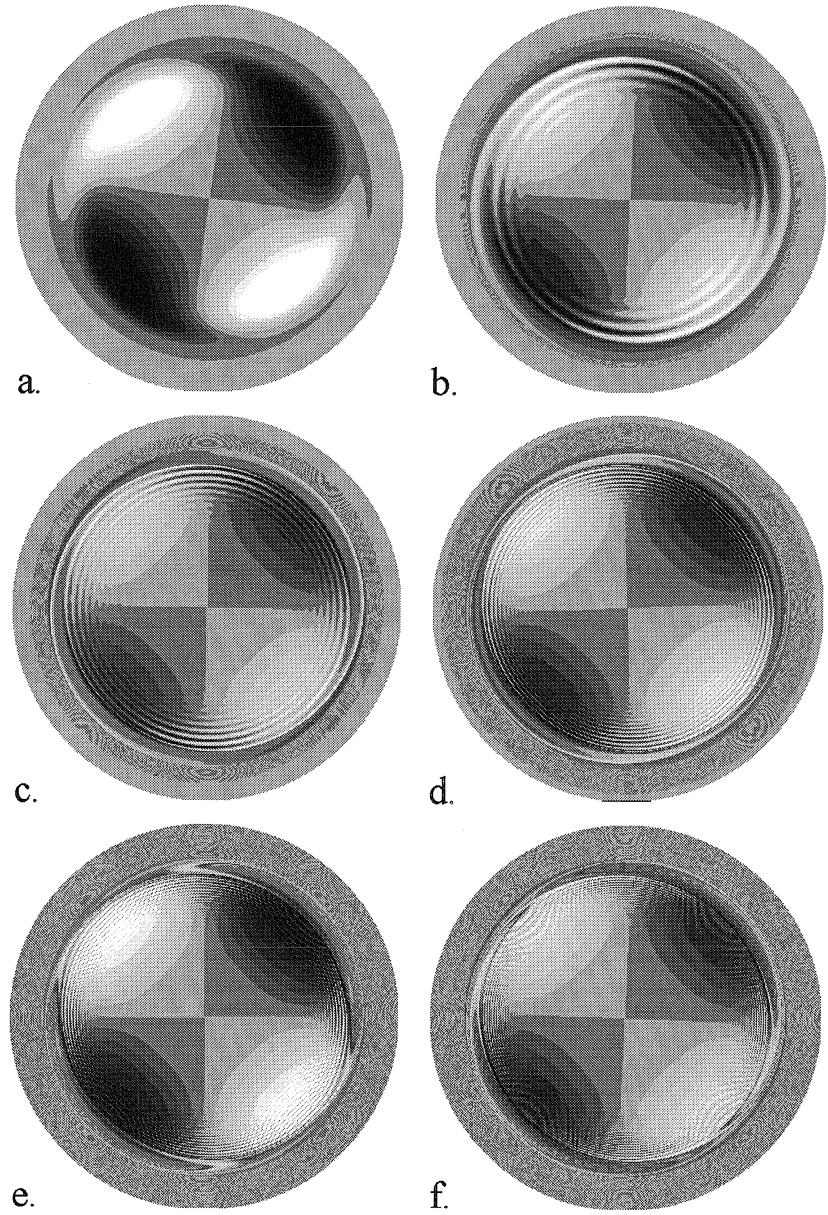


Figure 5.8: Images of the perturbed density at six different times for an external Gaussian pulse with a maximum amplitude of  $0.005\phi_0$ , and a FWHM of  $1.06t_{cr}$  applied to the Slow Decay Profile. The resulting perturbed electric field at the wall exhibits strong bounce oscillations. Figures (a)-(f) correspond to times  $2.65t_{cr}$ ,  $7.36t_{cr}$ ,  $12.1t_{cr}$ ,  $18.3t_{cr}$ ,  $24.4t_{cr}$  and  $31.5t_{cr}$ , respectively. The white area represents an area of positive density perturbation, where the black region indicates an area of negative perturbation. Near the edge of the plasma, two lobes of plasma form. These lobes are regions where fluid elements are trapped in the wave. The oscillation of the trapped fluid elements in the potential wall causes the bounce modulation of the perturbed electric field at the wall.

in both computations, which causes the perturbed electric field at the wall to decay exponentially. However, the mixing seen in figure 5.8 is less than in figure 4.12. This decrease in the mixing at higher amplitudes accounts for the corresponding lower decay rate at higher amplitudes. Essentially, the fields from the higher amplitude perturbation, caused by the higher amplitude applied pulse, are better able to hold the density perturbations in phase, causing the fluid elements to follow nonlinear orbits which do not mix as much at different radii. This leads to the lower decay rate in the perturbed electric field at the wall for higher amplitude applied pulses.

Another significant difference is visible in the images of the perturbed density. Near the outer region of the plasma, a tail of plasma is left behind. As time progresses, this tail stretches past the region of negative perturbation, and joins the other lobe of positive perturbation.

To see this effect still more clearly, an annulus containing the outer edge of the plasma was magnified and stretched flat for each of the images in figure 5.8. These strips of perturbed density are shown in figure 5.9.

These strips displaying the perturbed density are a magnification of the outer plasma edge. The vertical axis represents the radial direction of the previous figure, while the horizontal axis represents the theta direction.

In figure 5.9, one can actually see the trapped fluid elements oscillating in a potential well. The oscillation of the trapped fluid elements is the cause of the bounce oscillation seen in the perturbed electric field at the wall. The perturbed electric field at the wall is found to be minimum during the time the trapped fluid elements are traversing the region of negative density perturbation. The perturbed electric field at the wall is maximum when the trapped fluid elements are bunched up near the region of positive density perturbation. Some fluid elements near the outer edge are observed not being trapped, but instead are passing fluid elements. The figure is displaying a physical space image of Kelvin's "cat's eyes" [29] for trapped orbit fluid flow.

A final observation is that the density perturbation throughout the entire plasma oscillates with the trapped fluid elements. This feature is visible by comparing image

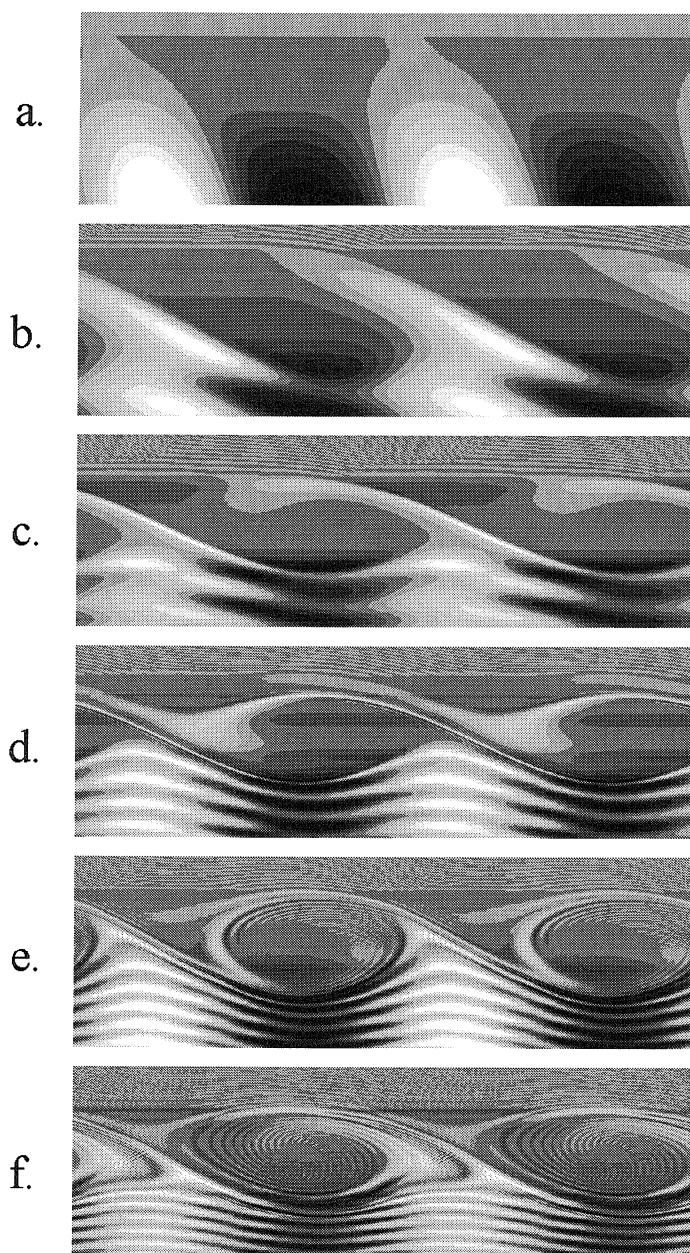


Figure 5.9: Magnification of the trapped fluid elements causing bounce oscillations. The images shown in this figure are a magnification of the edge of the plasma in figure 5.8, stretched flat. The vertical axis represents radius, while the horizontal axis represents theta. As time progresses from frame (a) to frame (f), the nonlinear orbits of trapped fluid elements are visible. The oscillation of the fluid elements within the potential well cause the modulation in the perturbed electric field at the wall. The image is suggestive of Kelvin's “cat's eyes” for trapped orbit fluid flow.

(c) and (e) of the figure 5.8. The coherent positive density perturbation region of image (e) is brighter than the coherent positive density perturbation region of image (c). Thus a type of feedback mechanism exists. As the trapped fluid elements approach the region of positive density perturbation, the field due to the trapped fluid elements add to the field due to the coherent density perturbation. The increase in the perturbed electric field increases the perturbed density of the coherent density perturbation, again amplifying the perturbed field. Thus the trapped fluid elements do not oscillate independently within the potential well, but are coupled to the amplitude of the well by the corresponding fields.

#### 5.2.4 BGK-Like Modes

This section describes a pulse that is slowly applied to the plasma. The plasma response has features resembling a BGK mode [20]. In the wave frame, a BGK mode is a steady nonlinear wave that is supported by a small class of particles trapped in the wave. A BGK mode would create an oscillating perturbed electric field at the wall that does not decay in time. In the wave frame, the perturbed density would not change in time, and the density is a function of the potential.

A high amplitude, short duration applied pulse is found to cause a decrease in the decay rate of the perturbed electric field at the wall and a bounce oscillation in the decay envelope. The bounce oscillation of the perturbed electric field is caused by discrete trapped fluid elements bouncing back and forth in the potential well of the wave. If the potential well was instead filled with fluid elements distributed evenly throughout the well, there would not be a bounce oscillation of the envelope of the perturbed electric field at the wall.

The discreteness of the trapped fluid elements is believed to be caused by the short time duration of the applied pulse. Such a short, high amplitude pulse perturbs the plasma in a manner that does not allow enough time to fill the potential well with fluid. Exciting the plasma with a smaller amplitude pulse for a longer duration in time may allow the plasma to distribute itself evenly throughout the potential well,

and eliminate the bounce oscillations, resulting in a perturbation resembling a BGK mode.

A long duration low amplitude external pulse is applied to the Slow Decay Profile. The external pulse has a Gaussian pulse shape and is applied in the frame moving with the wave with  $m = 2$  azimuthal symmetry. The pulse has a maximum amplitude of  $2.755 \times 10^{-4} \phi_0$ , and a full width at half maximum of  $31.8t_{cr}$ . Note that the applied pulse has a duration that is 30 times as long as the pulse in the previous section. To obtain the same amplitude for the perturbed electric field at the wall, the applied pulse amplitude is greater than  $\frac{1}{30}$  the amplitude of the pulse from the previous section. This is necessary because of the linear decay mechanism discussed in Chapter 4. Over the longer duration of this applied pulse, the decay mechanism prevents the perturbed electric field at the wall from reaching the same amplitude. Therefore the applied pulse amplitude is increased to compensate for the decay. The resulting maximum perturbed electric field at the wall is the same in both computations. However, in this computation, the energy is focused into a smaller frequency spectrum, centered around the  $m = 2$  resonant frequency. A plot of the envelope of the resulting perturbed electric field at the wall is shown in figure 5.10.

The perturbed electric field at the wall reaches a maximum amplitude of 1.18% of the unperturbed electric field at the wall. By using a slowly applied pulse, the bounce oscillations have been nearly eliminated. The decay of the perturbed electric field at the wall has also been greatly reduced compared to the decay rate for a small amplitude applied pulse that was shown in figure 5.2.

Figure 5.11(a) is a plot of the perturbed density at time  $147.2t_{cr}$ , and Figure 5.11(b) is a magnification of the outer plasma edge. The region of trapped fluid is visible near the plasma edge, and more evenly distributed for this slowly applied pulse, forming very distinctive “cat’s eyes.” With the plasma in the potential well evenly distributed, there is no bounce oscillation in the perturbed electric field at the wall. Additionally, the flow within the potential well appears to be sheared, causing the perturbed density within the well to form a spiral structure.

For an ideal BGK mode, the perturbed density in figure 5.11 would be independent

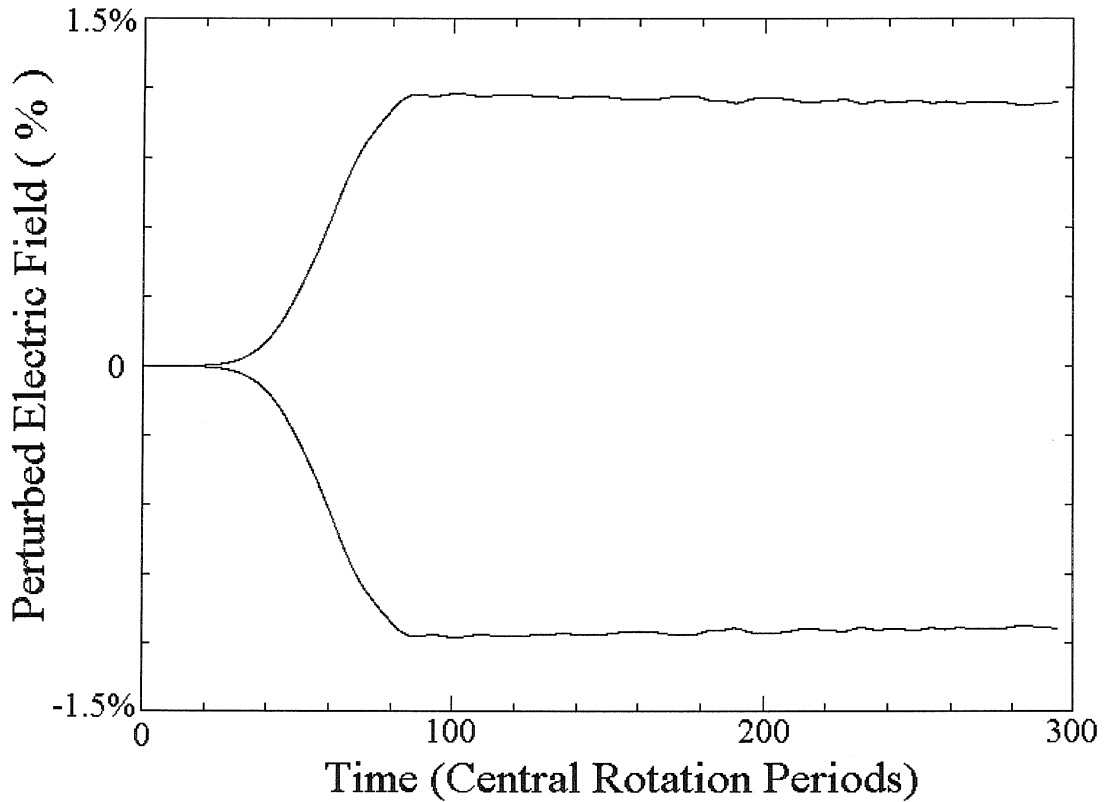


Figure 5.10: Plot of the envelope of the perturbed electric field at the wall resulting from a slow Gaussian pulse applied to the Slow Decay Profile and exciting a BGK-like mode. The applied pulse has a maximum amplitude of  $2.755 \times 10^{-4} \phi_0$ , and a FWHM of  $31.8 t_{cr}$ . The perturbed field reaches a maximum amplitude of 1.18% of the unperturbed electric field at the wall. By using a slowly applied pulse, the bounce oscillation has been nearly eliminated.

of time. For this computation, the perturbed density is steady, with the exception of slight motion of trapped fluid elements within the well forming a spiral structure. It should also be noted that this computation is pushing the limits of the fluid code by computing to a time of nearly  $300t_{cr}$ , and may have more accumulated error than other computations in this thesis.

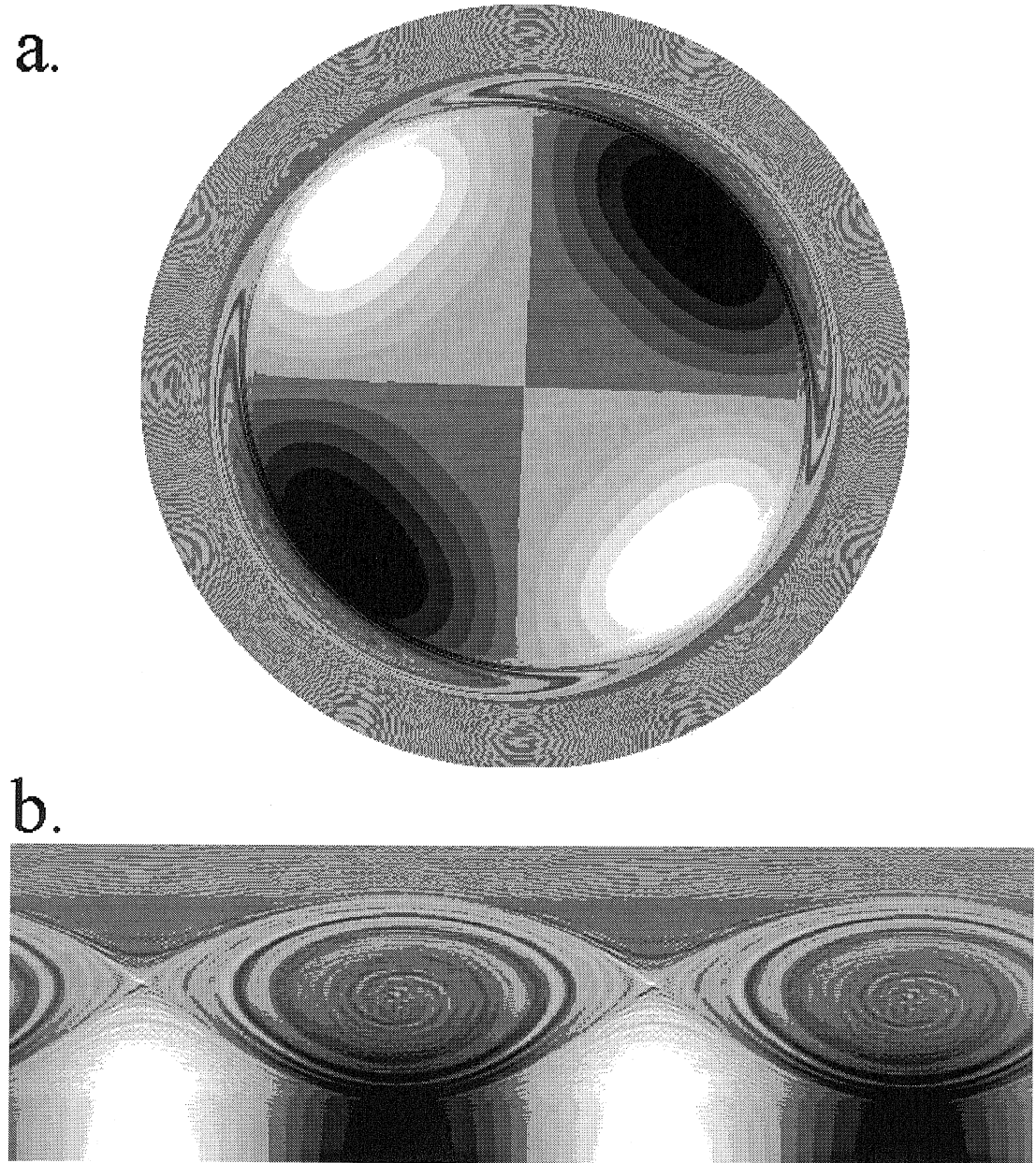


Figure 5.11: (a) Perturbed density resulting from a slowly applied Gaussian pulse exciting a BGK-like mode perturbation on the Slow Decay Profile. The applied pulse has a maximum amplitude of  $2.755 \times 10^{-4} \phi_0$ , and a FWHM of  $31.8t_{cr}$ . Near the edge of the plasma, two lobes of plasma form. These lobes are regions where fluid elements are trapped in the wave. Image (b) is a magnification of the outer plasma edge where trapping occurs, stretched out flat. The “cat’s eyes” are clearly visible in (b). The flow within the potential well appears sheared, causing the perturbed density within the well to form a spiral structure. The density within the potential well is evenly distributed, thus there is no bounce oscillation in the perturbed electric field at the wall.

### 5.3 Conclusion

In Chapter 4, low amplitude applied pulses were shown to result in an exponentially decaying perturbed electric field at the wall. This chapter showed that for higher amplitude pulses, a modulation of the envelope of the perturbed electric field is observed numerically, consistent with the experiment [19] and the Briggs prediction [10]. The modulation frequency is proportional to the square root of the amplitude of the perturbed electric field at the wall. The modulation of the decay envelope is caused by trapped fluid elements which are directly observable in successive images of the perturbed density. The oscillation of the fluid elements within the well corresponds to the bounce oscillations in the perturbed electric field. The bounce oscillations can be minimized by producing the same magnitude density perturbation with a lower amplitude external pulse applied over a longer period of time, exciting a perturbation within the plasma that resembles a BGK mode.

Even though nonlinear effects are occurring at the applied amplitudes discussed in this chapter, the total perturbations are not large, and can not be easily seen in images of the total density. Chapter 7 will look at nonlinear effects that can occur with very large applied amplitudes, where the perturbations can be seen in images of the total density.

# Chapter 6 Echoes in a Pure Electron Plasma

## 6.1 Introduction

Chapter 4 examined the response of the plasma to low amplitude applied pulses. The perturbed electric field at the wall was found to decay due to phase mixing of various radial layers of the perturbed density. This phase evolution of the perturbed density can be reversed by a nonlinear interaction with a second applied pulse. Application of a second pulse results in a subsequent reappearance of a perturbed electric field at the wall, many damping periods after the application of the second pulse. This reappearance of the perturbed electric field at the wall is referred to as an echo.

Echoes occur in systems where perturbations decay by a non-dissipative process, and many different echo phenomena have been observed [30][31][32][33]. In neutral plasmas, the plasma wave echo has been studied theoretically [34], and observed experimentally [35]. Since the perturbed electric field at the wall decays by a collisionless process in a non-neutral plasma, it is reasonable to expect that this system might also exhibit echoes. At this time, echoes have not been experimentally observed in non-neutral plasmas. Echoes in non-neutral plasmas have been analyzed by an extension of the linear analysis of Chapters 2, 3, and 4 [21], but those results are restricted to small amplitudes. A similar quasi-linear argument is presented in section 5.2. The Nonlinear Fluid Code is not restricted to small amplitudes and can be used to study echo phenomena.

This chapter will examine the effects of applying two pulses which are separated in time to a pure electron plasma. The first section presents a rough argument for the interaction of the two pulses. The argument describes the angular dependence of the echo, the time when the echo occurs, and the dependence of the echo amplitude

on the two applied pulse amplitudes and as a function of the time separation between the two applied pulses.

The next section describes echo calculations using the Nonlinear Fluid Code. Two external pulses, separated in time, are applied to a pure electron plasma. An echo response is found to occur long after the responses from the two applied pulses have decayed away. For small applied pulses, the echo is found to have a time and amplitude dependence that agrees with the rough argument for the echo. For higher amplitude pulses, the echo amplitude saturates, and higher order echoes caused by the interaction with harmonics of the applied pulses are observed. Echoes of echoes are also found to occur.

## 6.2 Echo Concept

This section presents a simplified analysis for the interaction of two applied pulses generating an echo. The echo occurs from a nonlinear interaction between the two applied pulses, where the second pulse partially unmixes the first pulse. The two applied pulses are treated in the linear approximation discussed in Chapter 2, and the echo is generated by a nonlinear interaction between pulses that is second order in amplitude. This quasi-linear description will lead to the following approximate results: symmetry requirements for an echo to occur, the angular symmetry of the echo, the time the echo occurs, and the amplitude dependence of the echo. These results are analogous to the results for the plasma wave echo [34]. Since this is a quasi-linear argument, the results are limited to small applied pulses. The results from the Nonlinear Fluid Code, presented in the next section, contain the full nonlinear effects and are not limited to small pulses.

The following argument is similar to the treatment presented by Gould [21]. Using the fluid model presented in Chapter 2, we will take the density  $n(r, \theta, t)$  and electric potential  $\phi(r, \theta, t)$  and divide them into steady-state quantities and perturbed quantities

$$n(r, \theta, t) = n_0(r) + n_1(r, \theta, t) + n_2(r, \theta, t) + n_3(r, \theta, t) + \dots \quad (6.1)$$

$$\phi(r, \theta, t) = \phi_0(r) + \phi_1(r, \theta, t) + \phi_2(r, \theta, t) + \phi_3(r, \theta, t) + \dots \quad (6.2)$$

The quantities  $n_0(r)$  and  $\phi_0(r)$  are steady-state quantities with no angular dependence. Subscript 1 corresponds to the perturbation due to the applied pulse 1 at time  $t = 0$ , and is first order in amplitude. Subscript 2 corresponds to the perturbation due to the applied pulse 2 at time  $t = \tau$ , and is first order in amplitude. Subscript 3 represents the echo perturbation from the nonlinear interaction between pulse 1 and pulse 2, and is second order in amplitude. Higher order terms exist, which could be included to form a theory on higher order echoes. In this argument, these higher order terms will be neglected. The response for the first and second pulse will be considered to first order in amplitude, and the echo will be considered to second order in amplitude.

Equation 6.1 and equation 6.2 for the density and potential are inserted into the equation 3.2 for the time derivative of the density in cylindrical coordinates. Keeping terms to first order for pulse 1 and pulse 2, and terms to second order for the echo results in

$$\frac{\partial n_1}{\partial t} = \frac{1}{r} \left( \frac{\partial n_0}{\partial r} \frac{\partial \phi_1}{\partial \theta} - \frac{\partial n_1}{\partial \theta} \frac{\partial \phi_0}{\partial r} \right) \quad (6.3)$$

$$\frac{\partial n_2}{\partial t} = \frac{1}{r} \left( \frac{\partial n_0}{\partial r} \frac{\partial \phi_2}{\partial \theta} - \frac{\partial n_2}{\partial \theta} \frac{\partial \phi_0}{\partial r} \right) \quad (6.4)$$

$$\frac{\partial n_3}{\partial t} = \frac{1}{r} \left( \frac{\partial n_0}{\partial r} \frac{\partial \phi_3}{\partial \theta} - \frac{\partial n_3}{\partial \theta} \frac{\partial \phi_0}{\partial r} \right) + S_3(r, \theta, t) \quad (6.5)$$

where

$$S_3(r, \theta, t) = \frac{1}{r} \left( \frac{\partial n_1}{\partial r} \frac{\partial \phi_2}{\partial \theta} - \frac{\partial n_1}{\partial \theta} \frac{\partial \phi_2}{\partial r} + \frac{\partial n_2}{\partial r} \frac{\partial \phi_1}{\partial \theta} - \frac{\partial n_2}{\partial \theta} \frac{\partial \phi_1}{\partial r} \right). \quad (6.6)$$

Equation 6.3 and 6.4 are the same linearizations discussed in Chapter 2 and describe two independent small amplitude pulses that will undergo mixing and decay exponentially in time. Equation 6.5 describes a third echo response that will undergo mixing and decay exponentially in time, with an additional source term  $S_3$  from the nonlinear interaction of pulse 1 and pulse 2.

If the time between the two applied pulses  $\tau$  is much greater than the decay time of the response to these pulses, it can be shown that the first term of equation 6.6 will dominate the other terms. This is because  $\phi_1$ , the perturbed potential due to pulse 1 decays exponentially in time, but  $n_1$ , the perturbed density due to pulse 1 has a term that persists and does not decay in time. Additionally, the radial derivative of the perturbed density of pulse 1,  $\frac{\partial n_1}{\partial r}$ , has a term that is proportional to  $t$ , and so it will dominate for a large time separation between applied pulses. Other terms exist, but these smaller terms will not be considered here. For  $\tau$  large compared to the decay time, the dominant component of the source term may be written as

$$S_3(r, \theta, t) \approx \frac{1}{r} \frac{\partial n_1}{\partial r} \frac{\partial \phi_2}{\partial \theta}. \quad (6.7)$$

Thus, source term is proportional to the radial density derivative of pulse 1, and the angular potential derivative of pulse 2. The real form for the perturbations rather than the complex exponential notation will be used since the source term involves the multiplication of two perturbed quantities.

We first give an approximate expression for the density perturbation caused by the first pulse. Pulse 1 is applied to the wall at time  $t = 0$ , and is approximated by  $V_1 \cos(m_1 \theta) \delta(t)$ , where  $V_1$  is the amplitude of pulse 1, and  $\delta(t)$  is the Dirac delta function. Treating the applied potentials as a delta function is a convenient approximation which is not too bad if the pulse separation is much greater than the decay times. At time  $t = 0$ , the impulse at the wall causes a density perturbation which begins to mix. The time dependent form of the density perturbation is given by

$$n_1(r, \theta, t) = V_1 D_c(r) \cos[m_1(\theta - \omega_0(r)t)] + \dots \quad (6.8)$$

where only the term that does not decay in time is considered. The variable  $D_c(r)$  describes the radial dependence of the perturbed density, and its exact form is not important for this discussion. This phase mixing process for the perturbed density was described in Chapter 4, and is due to the radial dependence of the angular velocity. Pulse 2 is applied to the wall at time  $t = \tau$ , and will be approximated by  $V_2 \cos(m_2\theta)\delta(t - \tau)$ , where  $V_2$  is the amplitude of pulse 2. The resulting perturbed potential is given by

$$\phi_2(r, \theta, t) = V_2 A_2(r) \cos(m_2\theta)\delta(t - \tau). \quad (6.9)$$

The radial dependence of the perturbed potential is included in  $A_2(r)$ . The exact form of  $A_2(r)$  is also not important for this discussion. The interaction between pulse 1 and pulse 2 is assumed to occur at the time  $t = \tau$  for simplicity. After this interaction, the plasma evolves in time by the phase mixing process. The source term is proportional to the derivatives of  $n_1$  and  $\phi_2$ . The radial derivative of  $n_1$  is given by

$$\frac{\partial n_1}{\partial r} = V_1 \tau D_c(r) m_1 \frac{\partial \omega_0(r)}{\partial r} \sin[m_1(\theta - \omega_0(r)t)] + \dots \quad (6.10)$$

where only the most important term is shown. The angular derivative of  $\phi_2$  is given by

$$\frac{\partial \phi_2}{\partial \theta} = V_2 A_2(r) m_2 \sin(m_2\theta)\delta(t - \tau). \quad (6.11)$$

Inserting equation 6.10 and equation 6.11 into equation 6.7, the source term  $S_3$  is approximated by

$$\begin{aligned} S_3(r, \theta, \tau) \approx & \frac{1}{r} V_1 V_2 \tau D_c(r) A_2(r) m_1 m_2 \frac{\partial \omega_0(r)}{\partial r} \frac{1}{2} \{ \cos[(m_1 - m_2)\theta - m_1 \omega_0(r)t] \\ & - \cos[(m_1 + m_2)\theta - m_1 \omega_0(r)t] \} \delta(t - \tau). \end{aligned}$$

The source term  $S_3$  exists only at time  $t = \tau$ . This term creates a density perturbation  $n_3$  which evolves in time due to phase mixing, and is given by

$$\begin{aligned}
n_3(r, \theta, t) \approx & \frac{1}{r} V_1 V_2 \tau D_c(r) A_2(r) m_1 m_2 \frac{\partial \omega_0(r)}{\partial r} \\
& \cdot \frac{1}{2} \{ \cos[(m_1 - m_2)\theta - m_1 \omega_0(r)\tau - (m_1 - m_2)\omega_0(r)(t - \tau)] \\
& - \cos[(m_1 + m_2)\theta - m_1 \omega_0(r)\tau - (m_1 + m_2)\omega_0(r)(t - \tau)] \}
\end{aligned}$$

for time  $t > \tau$ . This is the resulting density perturbation which generates the echo, due to the nonlinear interaction of pulse 1 and pulse 2. After the interaction at time  $t = \tau$ , the plasma phase mixes due to the radial dependence of the angular velocity.

The next step is to examine the time dependent phase for the two terms in  $n_3$ . It is expected that the echo will reach its maximum amplitude when the phase is independent of radius and the perturbation is aligned to give the maximum contribution to the electric field at the wall. When the perturbation is aligned, the second applied pulse has partially unmixed the first pulse. The time dependent phase is independent of radius when

$$[-m_1\tau - m_1t + m_2t + m_1\tau - m_2\tau]\omega_0(r) = 0$$

for the  $\cos[(m_1 - m_2)\theta]$  terms and

$$[-m_1\tau - m_1t - m_2t + m_1\tau + m_2\tau]\omega_0(r) = 0$$

for the  $\cos[(m_1 + m_2)\theta]$  terms. Solving the equation for the  $m_1 - m_2$  terms for  $t$  leads to

$$t = \frac{m_2}{m_2 - m_1}\tau.$$

In this case, the echo occurs after the second pulse as long as  $m_2 > m_1$ , and has azimuthal symmetry  $m_2 - m_1$ . At this time, the density perturbations at different radii are aligned, and the echo has a maximum contribution to the perturbed electric

field at the wall. If  $m_1 > m_2$ , then the echo would occur before both pulses. This violates causality, and therefore an echo does not occur when  $m_1 > m_2$ .

Solving the equation for the  $m_1 + m_2$  terms for  $t$  leads to

$$t = \frac{m_2}{m_2 + m_1} \tau.$$

This is a non-physical result, since this equation states that the echo would occur at a time  $t < \tau$ , since  $m_2 + m_1 > m_2$ . The echo obviously can not occur before the second pulse. We can conclude that the  $m_2 + m_1$  terms do not contribute to form an echo.

An echo can only occur when  $m_2 > m_1$ . Since only the  $m_1 - m_2$  terms contribute, the density perturbation term that generates the echo is given by

$$\begin{aligned} n_3(r, \theta, t) \approx & V_1 V_2 \tau D_c(r) A_2(r) \frac{m_1 m_2}{2r} \frac{\partial \omega_0(r)}{\partial r} \cos[(m_2 - m_1)\theta] \\ & + m_2 \omega_0(r) \tau - (m_2 - m_1) \omega_0(r) t. \end{aligned} \quad (6.12)$$

The density perturbation evolves in time from phase mixing, with different radial layers rotating at different rates. At time  $t = \frac{m_2}{m_2 - m_1} \tau$ , the density perturbations at different radial layers will align, producing a coherent electric field in the plasma that can be measured at the wall. In equation 6.12, the perturbed density is proportional to  $V_1, V_2$ , and  $\tau$ . Therefore, the echo is proportional to the amplitude of pulse 1, the amplitude of pulse 2, and the interpulse spacing  $\tau$ .

To summarize, there are six important conclusions from this argument describing the echo.

- An echo can only occur if the azimuthal symmetry number of the second pulse is greater than the azimuthal symmetry number of the first pulse, i.e.,  $m_2 > m_1$ .
- The echo will have azimuthal symmetry  $m_3 = m_2 - m_1$ .
- The echo will reach a maximum amplitude at the time  $t = \frac{m_2}{m_2 - m_1} \tau$ .
- The echo amplitude is proportional to amplitude of the first applied pulse,  $V_1$ .
- The echo amplitude is proportional to amplitude of the second applied pulse,  $V_2$ .

- The echo amplitude is proportional to the time between the two pulses,  $\tau$ .

The next section will look at results from the Nonlinear Fluid Code for two applied pulses. These results will be compared to the results of the argument presented in this section.

## 6.3 Echo Results

The previous argument suggests that an echo should occur if two pulses are applied to a pure electron plasma, separated in time, with the azimuthal symmetry number of the second pulse greater than for the azimuthal symmetry number of the first pulse. The Nonlinear Fluid Code is used to study the echo phenomena, and confirm the results of the argument presented in the previous section.

For these computations, the Fast Decay Profile,  $n_0(r) = n_0(0)\{1 - 3(\frac{r}{\alpha})^2 + 3(\frac{r}{\alpha})^4 - (\frac{r}{\alpha})^6\}$ , with  $\alpha = 0.8$ , was chosen. The reason for this choice is that the perturbed electric field at the wall due to an applied perturbation will quickly decay away in time. Therefore, the response to the first pulse and the response to the second pulse will have essentially vanished at the time of the echo, allowing the echo to be clearly observed.

### 6.3.1 Demonstration of the Echo

This section presents the results of the Nonlinear Fluid Code for a computation that satisfies the requirements to produce an echo. Two pulses, separated in time, are applied to the plasma, with the azimuthal symmetry number of the second pulse greater than the azimuthal symmetry number of the first pulse.

A one cycle sinusoidal pulse with a frequency of  $\omega_r = 0.62\omega_0(0)$  is applied at time  $t = 0$  with  $m_1 = 2$  azimuthal symmetry and an amplitude of  $1.0 \times 10^{-3}\phi_0$ . A second one cycle sinusoidal pulse at twice this frequency is applied at time  $\tau = 25t_{cr}$  with  $m_2 = 4$  azimuthal symmetry and an amplitude of  $2.0 \times 10^{-3}\phi_0$ . An echo is expected to occur at time  $t = \frac{m_2}{m_2 - m_1}\tau = \frac{4}{4-2}(25t_{cr}) = 50t_{cr}$  and have  $m_3 = m_2 - m_1 = 4 - 2 = 2$

azimuthal symmetry. The resulting perturbed electric field at the wall is shown in figure 6.1.

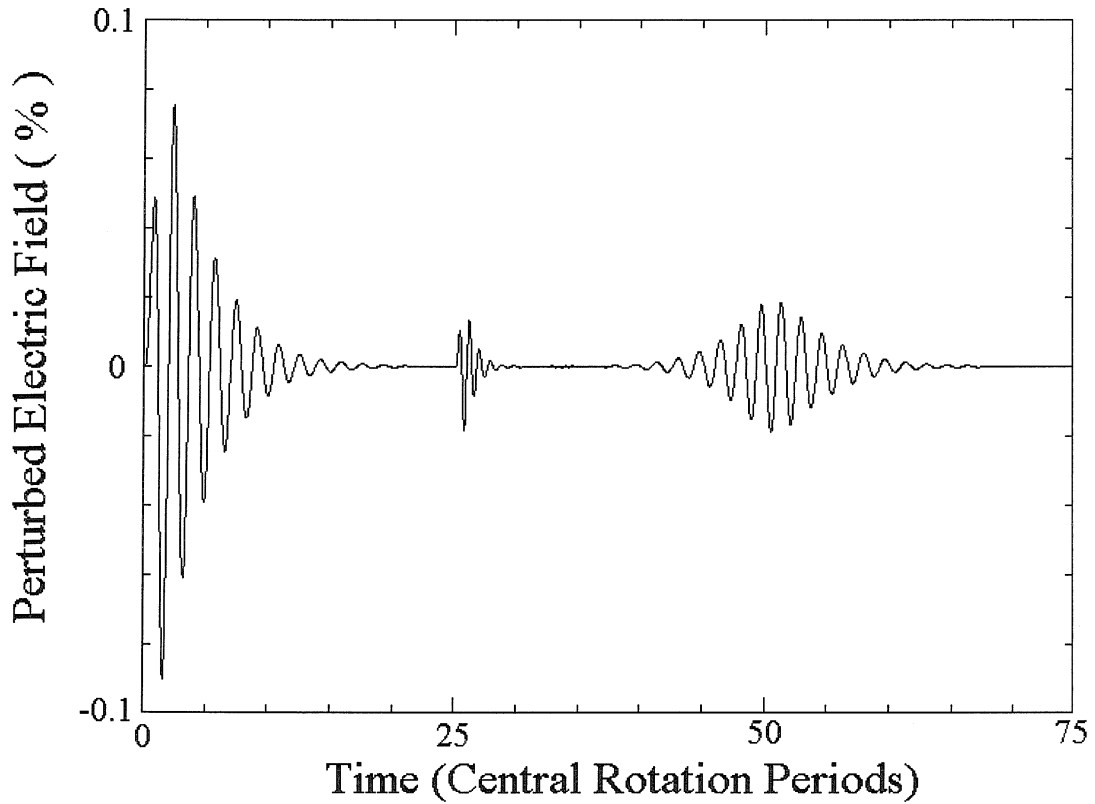


Figure 6.1: Plot of the perturbed electric field at the wall versus time for a calculation which demonstrates the echo. A one cycle pulse with  $m_1 = 2$  azimuthal symmetry and amplitude  $1.0 \times 10^{-3}\phi_0$  at time  $t = 0$  is applied to the Fast Decay Profile. A second one cycle pulse with  $m_2 = 4$  azimuthal symmetry and amplitude  $2.0 \times 10^{-3}\phi_0$  is applied at time  $\tau = 25t_{cr}$ . An echo then occurs at time  $t = 50t_{cr}$  with  $m_3 = 2$  azimuthal symmetry, obtaining a maximum amplitude of 0.0192% of the unperturbed electric field at the wall.

As seen in figure 6.1, the first  $m_1 = 2$  pulse at  $t = 0$  excites a response which decays exponentially. The second  $m_2 = 4$  pulse at time  $\tau = 25t_{cr}$  also excites a response which decays exponentially. A nonlinear interaction between these two applied pulses causes an  $m_3 = 2$  echo to occur at time  $t = 50t_{cr}$ . The echo reaches a maximum amplitude of 0.0192% of the unperturbed electric field at the wall.

As a second example, a one cycle sinusoidal pulse with a frequency of  $\omega_r = 0.62\omega_0(0)$  is applied at time  $t = 0$  with  $m_1 = 2$  azimuthal symmetry and an amplitude of  $1.0 \times 10^{-3}\phi_0$ . A second one cycle sinusoidal pulse at three times this frequency is applied at time  $\tau = 25t_{cr}$  with  $m_2 = 6$  azimuthal symmetry and an amplitude of  $3.0 \times 10^{-3}\phi_0$ . For these initial conditions, an echo is expected to occur at time  $t = 37.5t_{cr}$  with azimuthal symmetry  $m_3 = 4$ . The resulting perturbed electric field at the wall is shown in figure 6.2.

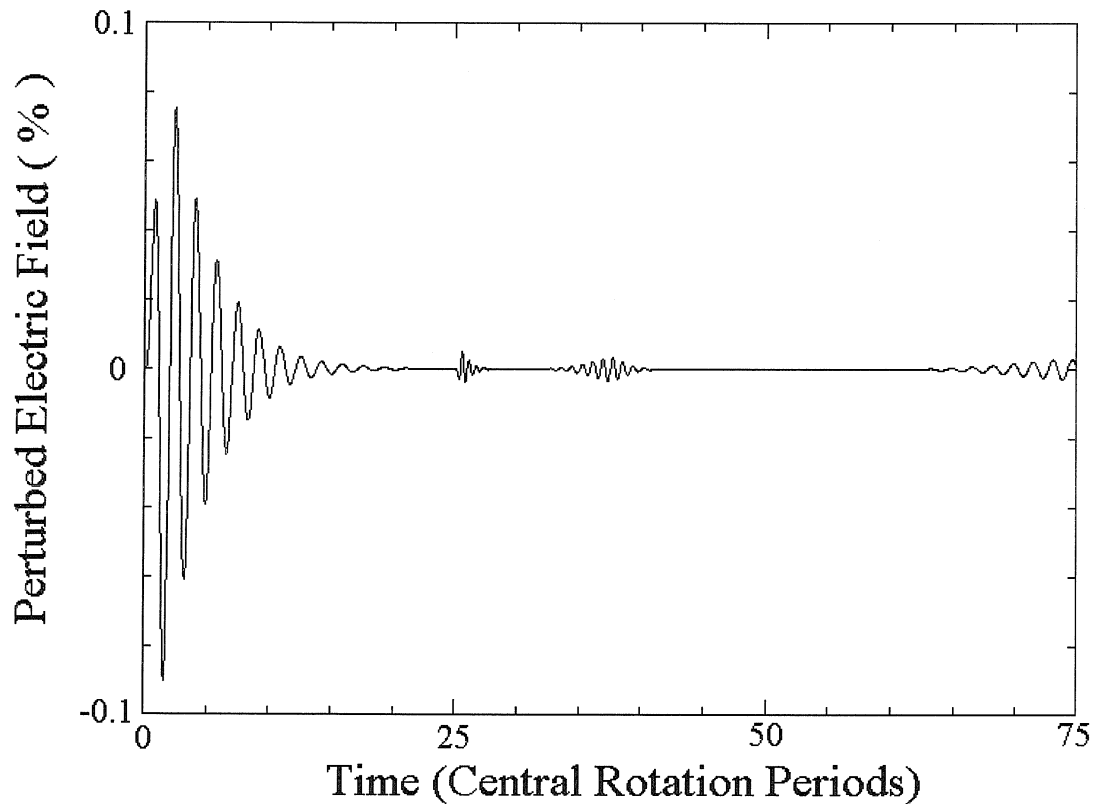


Figure 6.2: Plot of the perturbed electric field at the wall versus time for a one cycle  $m_1 = 2$  pulse with amplitude  $1.0 \times 10^{-3}\phi_0$  at time  $t = 0$ , and a one cycle  $m_2 = 6$  pulse with amplitude  $3.0 \times 10^{-3}\phi_0$  at time  $\tau = 25t_{cr}$  applied to the Fast Decay Profile. An echo occurs at time  $t = 37.5t_{cr}$  with  $m_3 = 4$  azimuthal symmetry and has a maximum amplitude of 0.00347% of the unperturbed electric field at the wall. Near time  $t = 75t_{cr}$ , a higher order echo occurs.

As seen in figure 6.2, an echo occurs at time  $t = 37.5t_{cr}$ . The echo has the expected

$m_3 = 4$  azimuthal symmetry, and reaches a maximum amplitude of 0.00347% of the unperturbed electric field at the wall.

There is also another echo occurring at a later time  $t = 75t_{cr}$ . This echo is actually a higher order echo of an echo, where the  $m_3 = 4$  echo is interacting with the  $m_1 = 2$  pulse at  $t = 0$  to produce an  $m = 2$  echo of an echo at time  $t = 75t_{cr}$ . Higher order effects will be discussed in more detail in a later section of this chapter.

The Nonlinear Fluid Code successfully demonstrates the phenomena of the echo. The echo has the correct azimuthal symmetry,  $m_3 = m_2 - m_1$ , and occurs at time  $t = \frac{m_2}{m_2 - m_1}\tau$ , in agreement with the argument of section 5.2. The next section provides a set of control cases, verifying that two pulses are required to produce an echo, with the mode number of the second pulse higher than the mode number of the first pulse.

### 6.3.2 Control Sets

This section provides the results from several control cases. These sets verify that the observed echo is not a numerical artifact, and that the echo only occurs when the azimuthal mode number of pulse 2 is higher than the azimuthal mode number of pulse 1.

#### Single Pulses

This section verifies that the response to a single applied pulse decays exponentially. For the amplitudes used in this section, no nonlinear effects such as bounce oscillations are observed. This is verified for the  $m = 2$ ,  $m = 4$ , and  $m = 6$  pulses that were used in the previous section.

A one cycle sinusoidal pulse with a frequency of  $\omega_r = 0.62\omega_0(0)$  is applied at time  $t = 0$  with  $m = 2$  azimuthal symmetry. The pulse is applied at the  $m = 2$  resonant frequency for this profile, with an amplitude of  $1.0 \times 10^{-3}\phi_0$  and a pulse length of  $1.613t_{cr}$ . The resulting perturbed electric field at the wall is plotted in figure 6.3.

This result is similar to the result of the previous chapter for this profile, shown in figure 4.2, but at a higher applied amplitude. The maximum perturbed electric

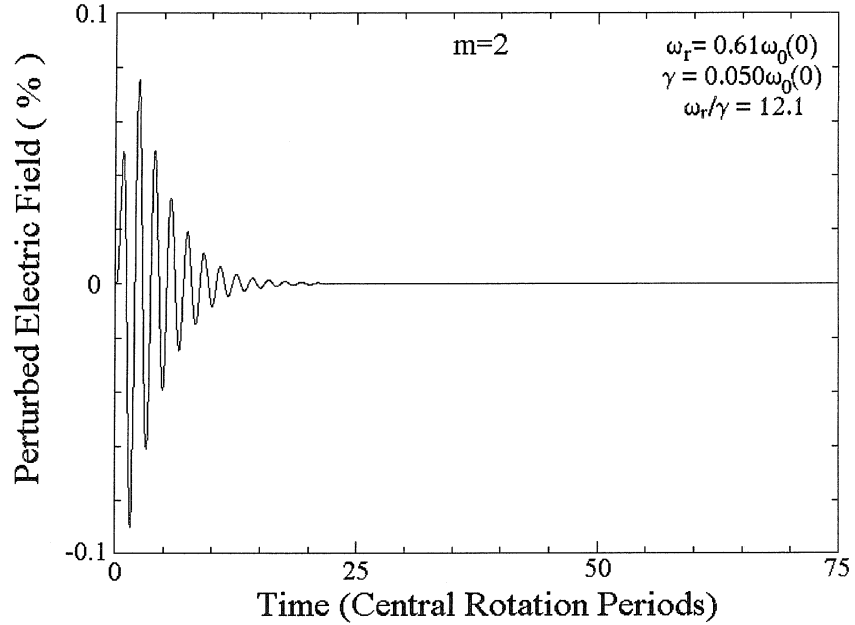


Figure 6.3: Perturbed electric field at the wall versus time for a one cycle pulse with  $m = 2$  azimuthal symmetry applied to the Fast Decay Profile. The pulse has an applied amplitude of  $1.0 \times 10^{-3} \phi_0$ , and the perturbed electric field at the wall reaches a maximum amplitude of 0.0916% of the unperturbed electric field at the wall. The plasma response decays exponentially.

field at the wall is found to be 0.0916% of the unperturbed electric field at the wall. The response to this applied pulse quickly decays in time.

A similar computation was performed using an applied pulse with  $m = 4$  symmetry. The  $m = 4$  pulse is applied at time  $t = 0$  for one cycle at a frequency of  $\omega = 1.24\omega_0(0)$ . The amplitude of this pulse is  $2.0 \times 10^{-3} \phi_0$ , with a pulse length of  $0.806t_{cr}$ . The resulting perturbed electric field at the wall for the  $m = 4$  pulse reaches a maximum amplitude of 0.0188%, and is shown in figure 6.4. Note that the scale for this figure has been increased by a factor of 5 compared to the figure for the  $m = 2$  pulse.

For the  $m = 6$  pulse, the applied frequency is  $\omega = 1.86\omega_0(0)$ , leading to a one cycle pulse length of  $0.538t_{cr}$ . The amplitude of the  $m = 6$  pulse is  $3.0 \times 10^{-3} \phi_0$ . The resulting perturbed electric field at the wall for the  $m = 6$  pulse reaches a maximum

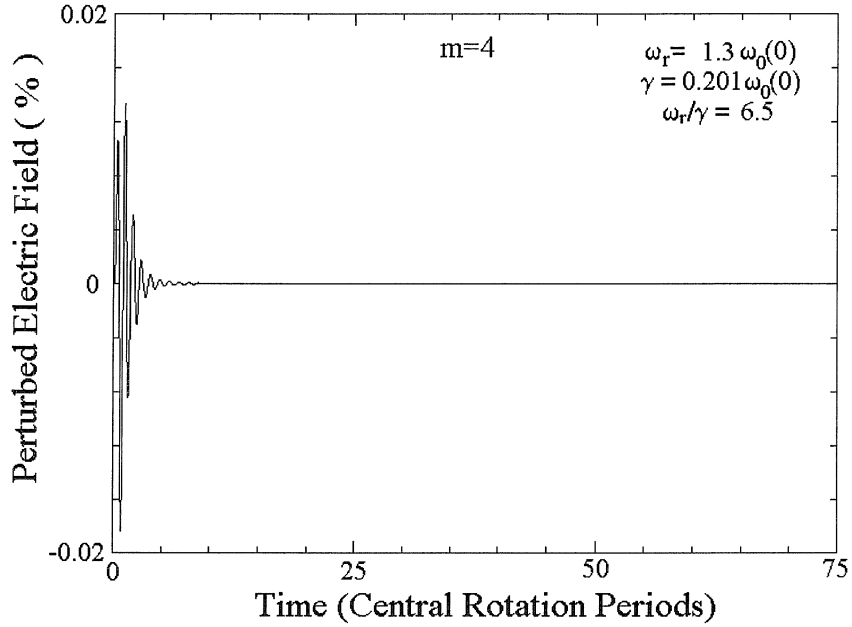


Figure 6.4: Perturbed electric field at the wall versus time for a one cycle pulse with  $m = 4$  azimuthal symmetry applied to the Fast Decay Profile. The pulse has an applied amplitude of  $2.0 \times 10^{-3} \phi_0$ , and the perturbed electric field at the wall reaches a maximum amplitude of 0.0188% of the unperturbed electric field at the wall. The plasma response decays exponentially.

amplitude of 0.00509% and is shown in figure 6.5. In this figure, the scale has been increased by a factor of 20 compared to the figure for the  $m = 2$  pulse.

The frequencies used for the  $m = 4$  and  $m = 6$  pulse are not the exact resonant frequencies, but rather twice and three times the resonant frequency for the  $m = 2$  pulse. However, since only a one cycle pulse is used, the frequency spectrum is quite broad, so it is unnecessary to apply the exact resonant frequency. Additionally, the applied amplitude for the  $m = 4$  and  $m = 6$  pulse has been increased by a factor of two and three, respectively, to compensate for the shorter pulse length, as compared to the  $m = 2$  pulse. Thus the total energy applied to the plasma in all three computations should be equal.

As can be seen from the figures, the single pulses behave as expected. The perturbed electric field at the wall rapidly decays away for each pulse, consistent with

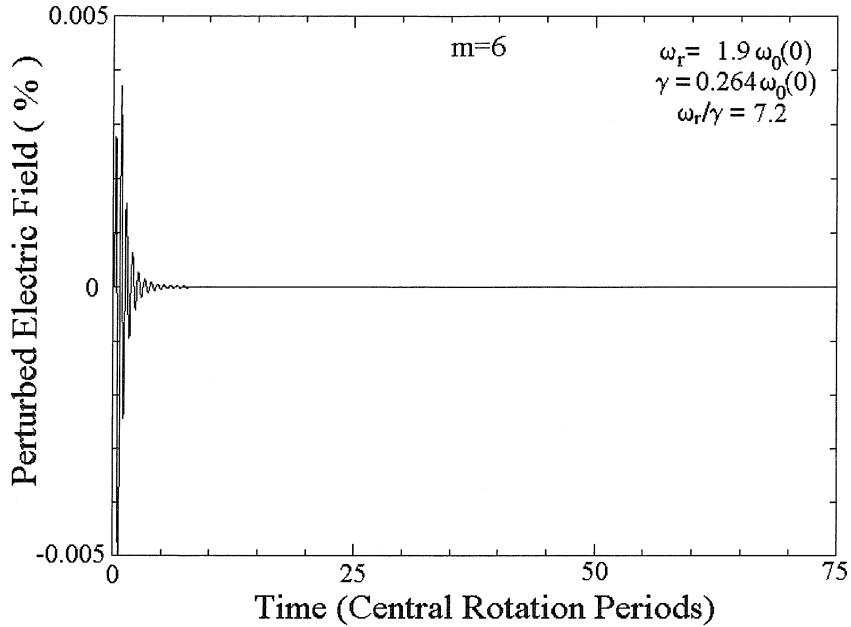


Figure 6.5: Perturbed electric field at the wall versus time for a one cycle pulse with  $m = 6$  azimuthal symmetry applied to the Fast Decay Profile. The pulse has an applied amplitude of  $3.0 \times 10^{-3} \phi_0$ , and the perturbed electric field at the wall reaches a maximum amplitude of 0.00509% of the unperturbed electric field at the wall. The plasma response decays exponentially.

the results of Chapter 4. No nonlinear phenomena such as bounce oscillations are observed at these amplitudes.

It should be noted that the resulting perturbed electric field at the wall is lower for the  $m = 4$  pulse and  $m = 6$  pulse, even though the total energy for each pulse is the same. The reason for this discrepancy is that for the applied pulse, the perturbed potential at the resonant radius  $r_s$  is proportional to  $(\frac{r_s}{r_w})^m$  where  $r_w$  is the wall radius. Thus for higher  $m$  values, the field falls off more rapidly as the plasma is further away from the wall sectors than for lower  $m$  values. Additionally, the resulting density perturbations at the resonant radius create a perturbed electric field at the wall that is also proportional to  $(\frac{r_s}{r_w})^m$ . Therefore, the perturbed electric field at the wall will be smaller for higher  $m$  valued density perturbations. The net effect is that an applied pulse of voltage at the wall will induce a response in the perturbed electric field at

the wall which will have an amplitude response that is proportional to  $(\frac{r_s}{r_w})^{2m}$ . Thus higher  $m$  valued applied pulses will have a lesser contribution in the perturbed electric field at the wall.

### Two Pulses with $m_1 > m_2$

An echo can only occur if the azimuthal mode number of the second pulse is higher than the azimuthal mode number of the first pulse. This section searches for a counter example by applying an  $m_1 = 4$  pulse followed by an  $m_2 = 2$  pulse. This computation uses the same pulses that were used in the echo computation above, but with the order of the two pulses reversed.

A one cycle pulse is applied at time  $t = 0$  with  $m_1 = 4$  symmetry and an amplitude of  $2.0 \times 10^{-3}\phi_0$ . A second one cycle pulse is applied at time  $\tau = 25t_{cr}$  with  $m_2 = 2$  symmetry and an amplitude of  $1.0 \times 10^{-3}\phi_0$ . The resulting perturbed electric field at the wall is shown in figure 6.6.

As seen in figure 6.6, a nonlinear interaction between these two pulses is not observed. The first pulse is applied, and it decays away. The second pulse is applied later, and it also decays away. No echo is generated. This result is consistent with the argument from section 5.2. The first pulse has an azimuthal symmetry eigenvalue greater than the azimuthal symmetry eigenvalue of the second pulse. In the argument presented in the previous section, no echo can occur if  $m_1 > m_2$ .

To summarize the results of this section, these computations using the Nonlinear Fluid Code verify the existence of the echo in non-neutral plasmas. The echo is found to only occur when  $m_2 > m_1$ . Additionally, the echo is found to have azimuthal symmetry of  $m_3 = m_2 - m_1$ , and occur at a time  $t = \frac{m_2}{m_2 - m_1}\tau$ . These results are consistent with the argument presented in section 5.2. The next section will explore the dependence of the echo amplitude on the amplitudes of the applied pulses and the interpulse separation.

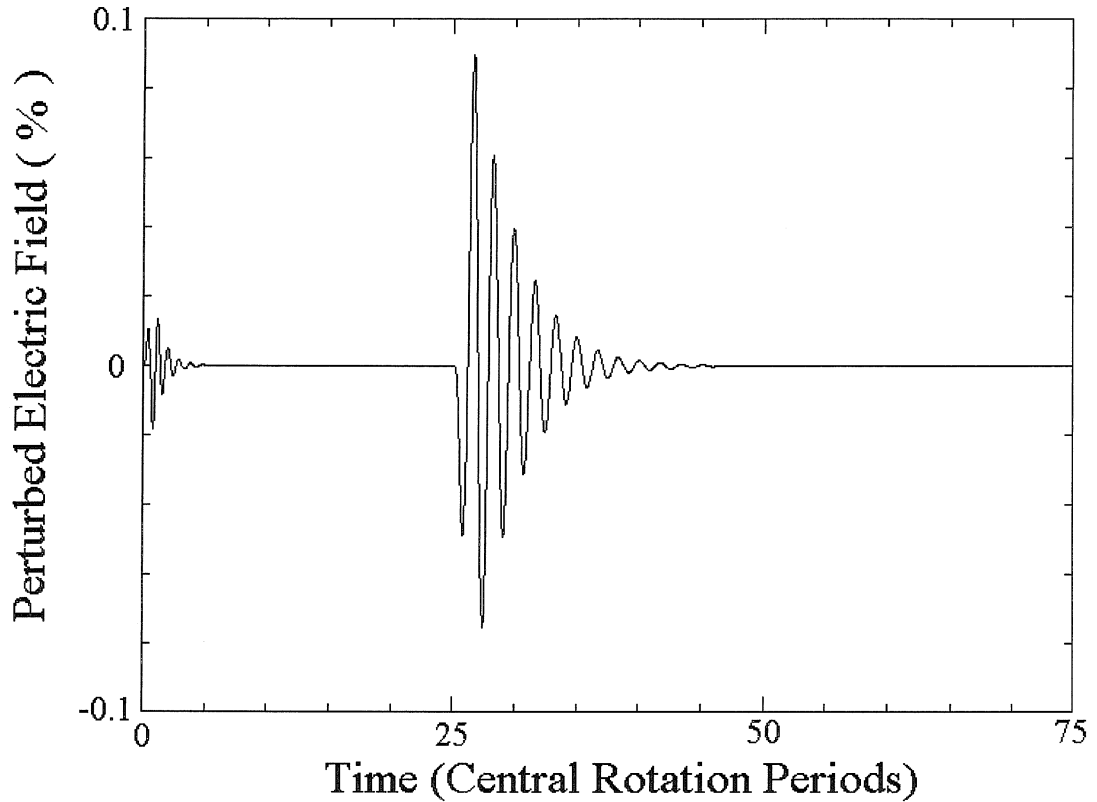


Figure 6.6: Perturbed electric field at wall for a one cycle  $m_1 = 4$  pulse at time  $t = 0$ , and a one cycle  $m_2 = 2$  pulse at time  $\tau = 25t_{cr}$  applied to the Fast Decay Profile. Both pulses decay away, with no echo produced.

### 6.3.3 Amplitude of the Echo

#### Dependence on First and Second Pulse Amplitudes

The previous section verified the existence of the echo, as well as the azimuthal symmetry of the echo and the time the echo occurs. This section will explore the amplitude of the echo in relation to the amplitude of the two applied pulses. For the following computations, a one cycle pulse with  $m_1 = 2$  azimuthal symmetry is applied at time  $t = 0$ , and a one cycle pulse with  $m_2 = 4$  azimuthal symmetry is applied at time  $\tau = 25t_{cr}$ . The amplitude of the two pulses is varied, and the resulting change in the echo amplitude is observed. The results are summarized in table 6.1.

Pulse 1 Amplitude	Pulse 2 Amplitude	Echo Amplitude
$1.0 \times 10^{-3} \phi_0$	$2.0 \times 10^{-3} \phi_0$	0.0192%
$1.0 \times 10^{-3} \phi_0$	$1.0 \times 10^{-3} \phi_0$	0.00972%
$5.0 \times 10^{-4} \phi_0$	$2.0 \times 10^{-3} \phi_0$	0.00959%
$5.0 \times 10^{-4} \phi_0$	$1.0 \times 10^{-3} \phi_0$	0.00485%

Table 6.1: Echo amplitude versus applied pulse 1 and pulse 2 amplitude. Pulse 1 is a one cycle pulse with  $m_1 = 2$  symmetry and is applied at time  $t = 0$ . Pulse 2 is a one cycle pulse that has  $m_2 = 4$  symmetry and is applied at time  $\tau = 25t_{cr}$ . The echo has  $m_3 = 2$  symmetry and occurs at time  $t = 50t_{cr}$ . The echo amplitude is given as a percentage of the unperturbed electric field at the wall.

With the amplitude of the second pulse halved, the echo amplitude is halved. For the amplitude of the first pulse halved, the echo amplitude is halved. With the amplitude of both applied pulses halved, the echo is reduced by a factor of 4. This is clearly illustrated by figure 6.7, which plots the perturbed electric field at the wall for these computations. The echo is proportional to the amplitude of the first pulse multiplied by the amplitude of the second pulse.

The amplitude of the echo is systematically studied as a function of the first  $m_1 = 2$  pulse amplitude, occurring at time  $t = 0$ . The amplitude of the  $m_2 = 4$  pulse at time  $\tau = 25t_{cr}$  is held fixed at  $2.0 \times 10^{-3} \phi_0$ . The echo amplitude versus applied pulse 1 amplitude is plotted on a log-log scale in figure 6.8.

The points of figure 6.8 lie along a straight line of slope one. This indicates that the echo amplitude is proportional to the amplitude of the first pulse.

The amplitude of the echo is also systematically studied as a function of the second  $m_2 = 4$  pulse amplitude, occurring at time  $\tau = 25t_{cr}$ . The amplitude of the  $m_1 = 2$  pulse at time  $t = 0$  is held fixed at  $1.0 \times 10^{-3} \phi_0$ . The echo amplitude versus applied pulse 2 amplitude is plotted on a log-log scale in figure 6.9.

The points of figure 6.9 lie along a straight line of slope one. This indicates that the echo amplitude is proportional to the amplitude of the second pulse.

The amplitude of the echo is proportional to the amplitude of the first applied pulse, multiplied by the amplitude of the second applied pulse. This amplitude dependence of the echo agrees with the results predicted by the argument of section 5.2. The next section will study the amplitude dependence of the echo as a function

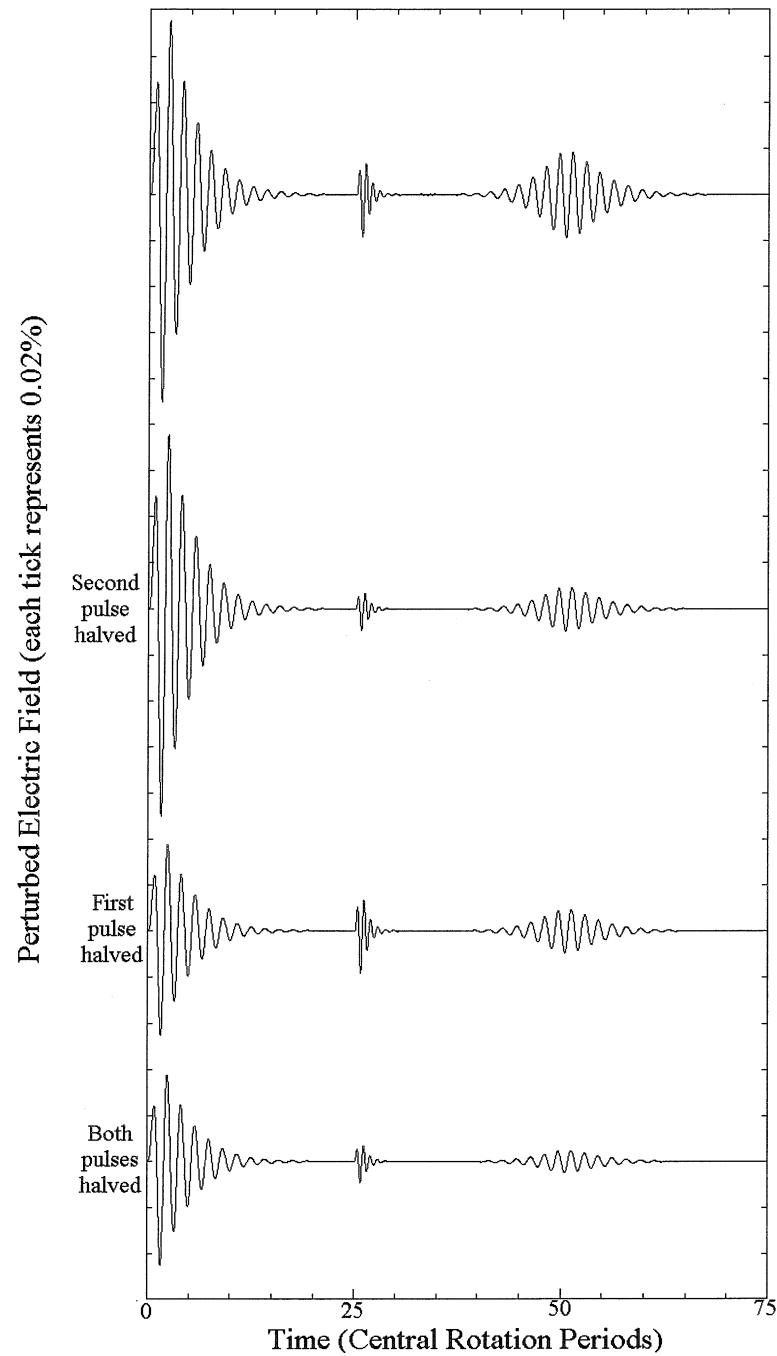


Figure 6.7: Perturbed electric field at wall for four echo computations varying in applied amplitude. The second trace has the amplitude of the second pulse halved. The third trace has the amplitude of the first pulse halved. In the fourth trace, the amplitude of both applied pulses are halved. The echo amplitude is found to be proportional to the amplitude of the first pulse, and proportional to the amplitude of the second pulse.

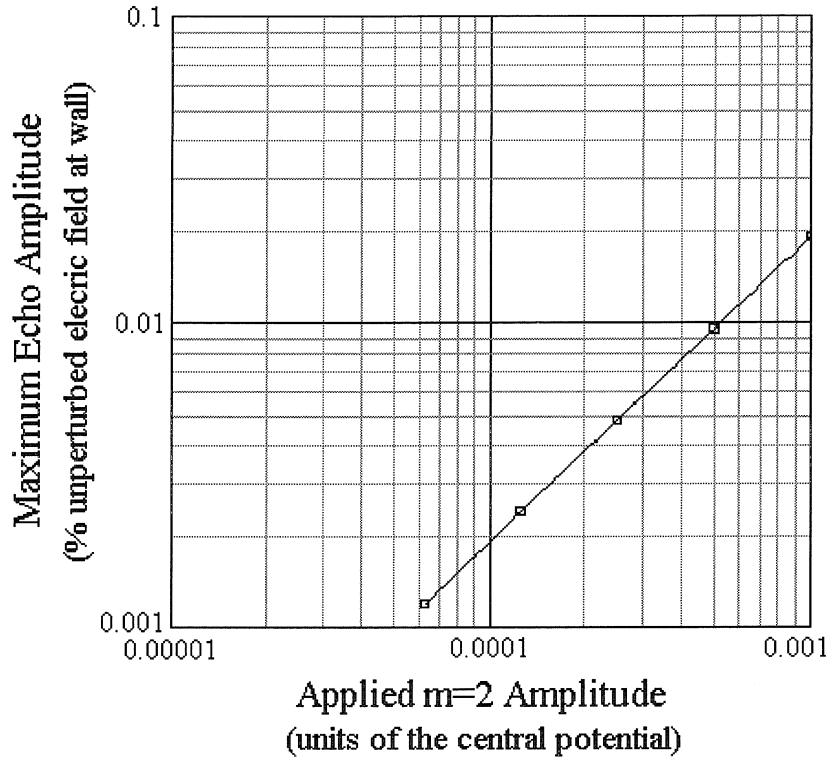


Figure 6.8: Plot of the maximum amplitude of the echo versus applied  $m_1 = 2$  amplitude of the first pulse on a log-log scale. The  $m_2 = 4$  amplitude is fixed at  $2.0 \times 10^{-3} \phi_0$ . The first pulse is excited with a one cycle burst at time  $t = 0$ , and the second pulse is excited with a one cycle burst at time  $\tau = 25t_{cr}$ . The solid line is a best fit with slope 1, indicating that the echo amplitude is proportional to the amplitude of the first pulse.

of the time between the two applied pulses.

### Dependence on Interpulse Spacing in Time

The previous section found the amplitude of the echo to be proportional to the amplitude of the first applied pulse, and proportional to the amplitude of the second applied pulse. This section will examine the amplitude of the echo with respect to the time between the two applied pulses,  $\tau$ . For the following computations, a one cycle pulse with  $m_1 = 2$  azimuthal symmetry is applied at time  $t = 0$  with an amplitude of  $1.0 \times 10^{-3} \phi_0$ . A second one cycle pulse with  $m_2 = 4$  symmetry is applied at a later time  $\tau$ , with an amplitude of  $2.0 \times 10^{-3} \phi_0$ . The time  $\tau$  for the second pulse is

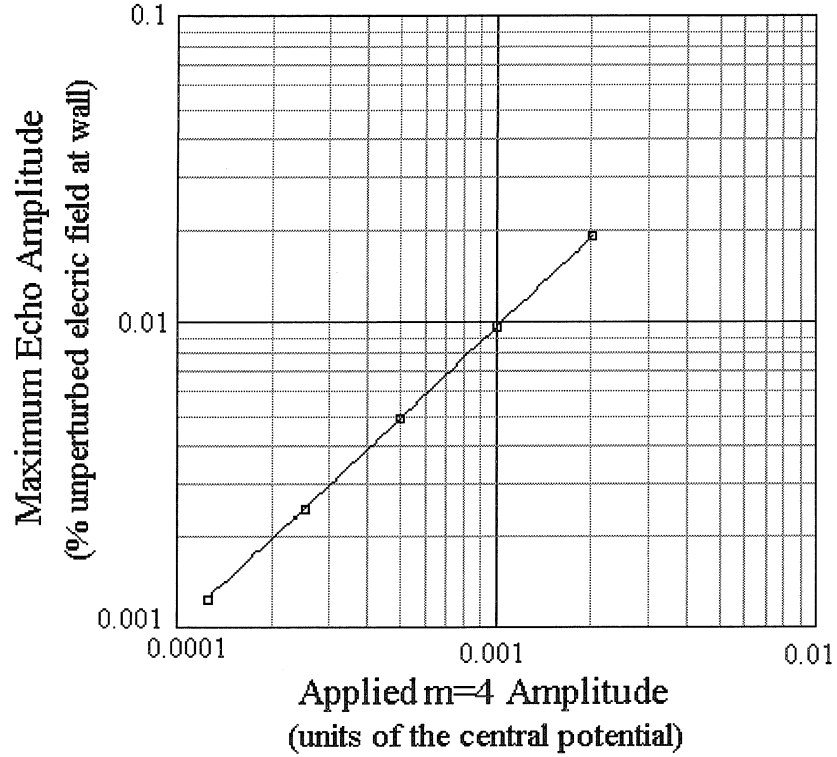


Figure 6.9: Plot of the maximum amplitude of the echo versus applied  $m_2 = 4$  amplitude of the second pulse on a log-log scale. The  $m_1 = 2$  amplitude is fixed at  $1.0 \times 10^{-3} \phi_0$ . The first pulse is excited with a one cycle burst at time  $t = 0$ , and the second pulse is excited with a one cycle burst at time  $\tau = 25t_{cr}$ . The solid line is a best fit with slope 1, indicating that the echo amplitude is proportional to the amplitude of the second pulse.

varied, and the resulting change in the echo amplitude is observed. The results are summarized in table 6.2.

As the time between pulses is increased, the amplitude of the echo increases. The perturbed electric field at the wall versus time for three cases is plotted in figure 6.10. The echo amplitude is found to be proportional to the temporal interpulse spacing,  $\tau$ . This result is also consistent with the echo argument presented above. The echo amplitude results of table 6.2 are plotted on a log-log scale in figure 6.11.

The straight line has slope one. For the first several points, the echo amplitude is proportional to the interpulse spacing. For the longer times between pulses, some saturation of the echo amplitude occurs. Saturation effects will be discussed in the

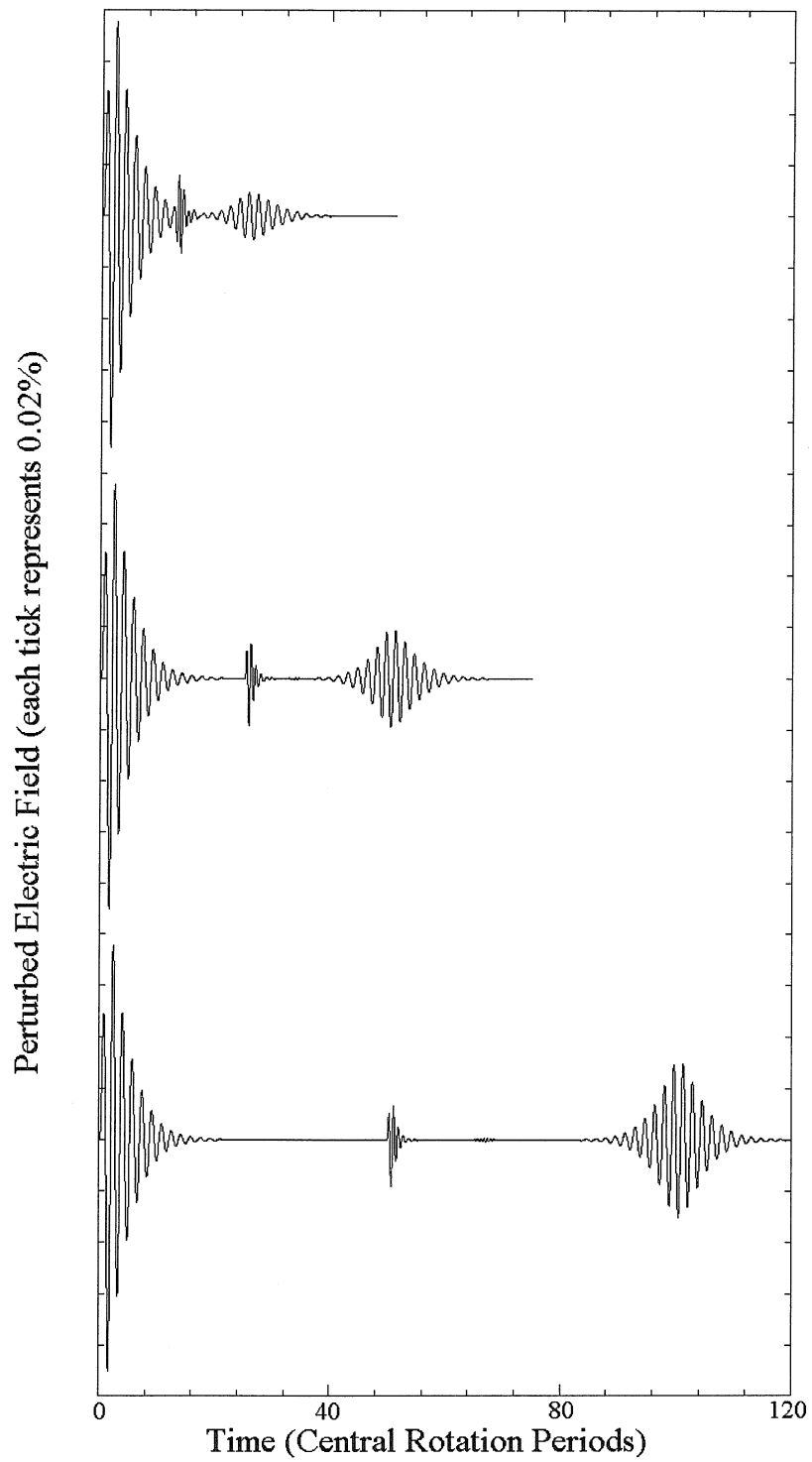


Figure 6.10: Perturbed electric field at wall for three echo computations, varying the interpulse spacing,  $\tau$ . The first trace has half the interpulse spacing of the second. The third trace has twice the interpulse spacing of the second. The echo amplitude is found to be proportional to the interpulse spacing.

Interpulse Spacing $\tau$	Echo Amplitude
$12.5t_{cr}$	0.00932%
$17.7t_{cr}$	0.0137%
$25t_{cr}$	0.0192%
$35.4t_{cr}$	0.0261%
$50t_{cr}$	0.0309%

Table 6.2: Echo amplitude as a function of interpulse spacing. A one cycle pulse with  $m_1 = 2$  symmetry and amplitude  $1.0 \times 10^{-3}\phi_0$  is applied at time  $t = 0$ . A second one cycle pulse with  $m_2 = 4$  symmetry and amplitude  $2.0 \times 10^{-3}\phi_0$  is applied at time  $t = \tau$ . The echo amplitude is measured as a percentage of the unperturbed electric field at the wall.

next section.

To summarize this section, for small amplitude pulses, the amplitude of the echo is proportional to the amplitude of the first pulse, multiplied by the amplitude of the second pulse. The echo amplitude is also proportional to the time between the two applied pulses. These results are consistent with the echo argument presented in section 5.2. The next section will describe the effect on the echo when larger amplitude pulses are applied to the plasma, and higher order terms become important.

### 6.3.4 Higher Amplitude Effects

#### Saturation at Higher Amplitudes

The previous section examined the effect of two small pulses interacting. In this low amplitude limit, the echo was found to be proportional to the amplitude of the first pulse multiplied by the amplitude of the second pulse, and also proportional to the interpulse spacing. This section will look at the effect larger amplitude pulses have on the echo. The effect from larger amplitude pulses is not contained in the echo argument presented in section 5.2 because higher order terms were neglected. The Nonlinear Fluid Code contains all the higher order terms, and therefore is not limited to studying low amplitude effects. For large applied pulses, the amplitude of the echo can saturate.

The amplitude of the echo was systematically studied as a function of pulse 1

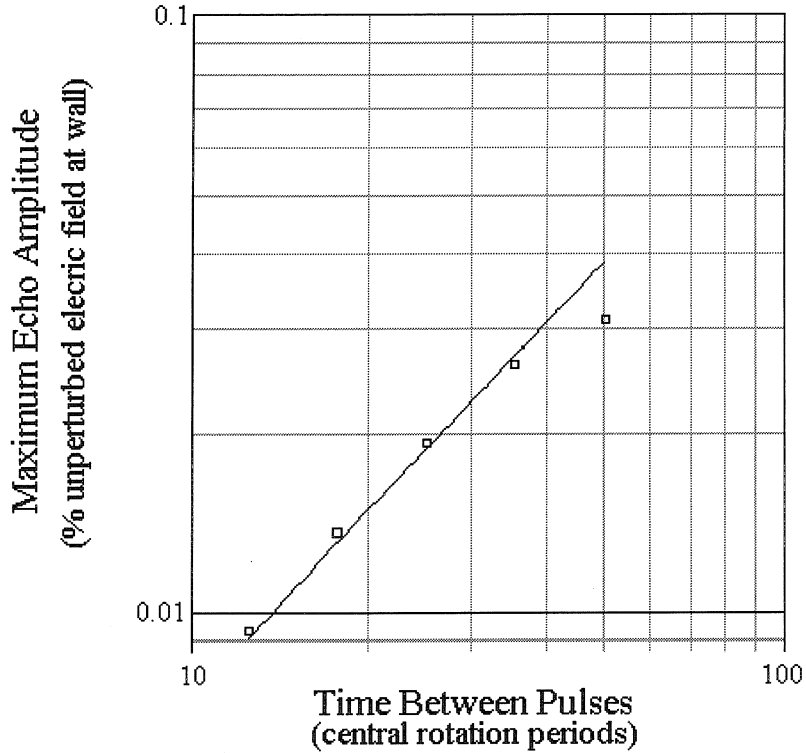


Figure 6.11: Plot of the amplitude of the echo versus interpulse spacing of the applied pulses on a log-log scale. The one cycle  $m_1 = 2$  pulse has a fixed amplitude of  $1.0 \times 10^{-3} \phi_0$ , and the one cycle  $m_2 = 4$  pulse has a fixed amplitude of  $2.0 \times 10^{-3} \phi_0$ . The straight line has slope one. For the first few points, the echo amplitude is proportional to the interpulse spacing. For longer spacings, the echo amplitude saturates.

amplitude and pulse 2 amplitude. Pulse 1 is excited by a one cycle sinusoidal burst with  $m_1 = 2$  azimuthal symmetry at time  $t = 0$ . Pulse 2 is excited by a one cycle sinusoidal burst with  $m_2 = 4$  symmetry at time  $\tau = 25t_{cr}$ . An echo with azimuthal symmetry  $m_3 = 2$  occurs at time  $t = 50t_{cr}$ . The amplitude of pulse 1 and the amplitude of pulse 2 were varied together.

The lowest amplitude case has a one cycle  $m_1 = 2$  applied pulse amplitude of  $1.25 \times 10^{-4} \phi_0$ , and a one cycle  $m_2 = 4$  applied pulse amplitude of  $2.5 \times 10^{-4} \phi_0$ . The echo reaches a maximum perturbed amplitude of 0.000305% of the unperturbed electric field at the wall. For each successive case, the applied pulse amplitude of the  $m_1 = 2$  pulse and the applied pulse amplitude of the  $m_2 = 4$  pulse was varied

together, increased by a factor of  $\sqrt{2}$ . The applied amplitude of the  $m_2 = 4$  pulse always has twice the applied amplitude and half of the pulse duration of the  $m_1 = 2$  pulse.

The response of the electric field at the wall for the first pulse is proportional to the applied amplitude of the first pulse. The response of the electric field at the wall for the second pulse is proportional to the applied amplitude of the second pulse. For the lower amplitude pulses, the echo amplitude is proportional to the amplitude of the first pulse multiplied by the amplitude of the second pulse. For higher amplitudes, the echo saturates. These results are summarized in figure 6.12. The response of the first pulse, response of the second pulse, and the echo response are plotted versus applied pulse 1 amplitude (also applied pulse 2 amplitude divided by 2) on a log-log scale in figure 6.12.

On this plot it is possible to see the heavy saturation occurring at the higher amplitudes. The slope is one for the response of the  $m_1 = 2$  pulse and for the  $m_2 = 4$  pulse, indicating that the response amplitude is still in the linear range for each individual pulse. For the lower amplitude points, the slope for the echo response is two, illustrating that the echo is proportional to the amplitude of the first pulse multiplied by the amplitude of the second pulse. For the larger applied amplitudes, higher order effects are dominating, limiting the response amplitude of the echo. The next section will examine higher order echoes that can occur at larger amplitudes.

### Higher Order Echoes

The approximate argument in section 5.2 describes the echo phenomena for small applied pulses. At larger amplitudes, higher order effects become important. Specifically, harmonics of the applied pulses can cause higher order echoes.

If we describe the harmonics with the harmonic number  $h$ , where  $h = 1$  is the fundamental,  $h = 2$  is the second harmonic, etc., the equations describing the property of the higher order echo are as follows. The higher order echo will have azimuthal symmetry described by

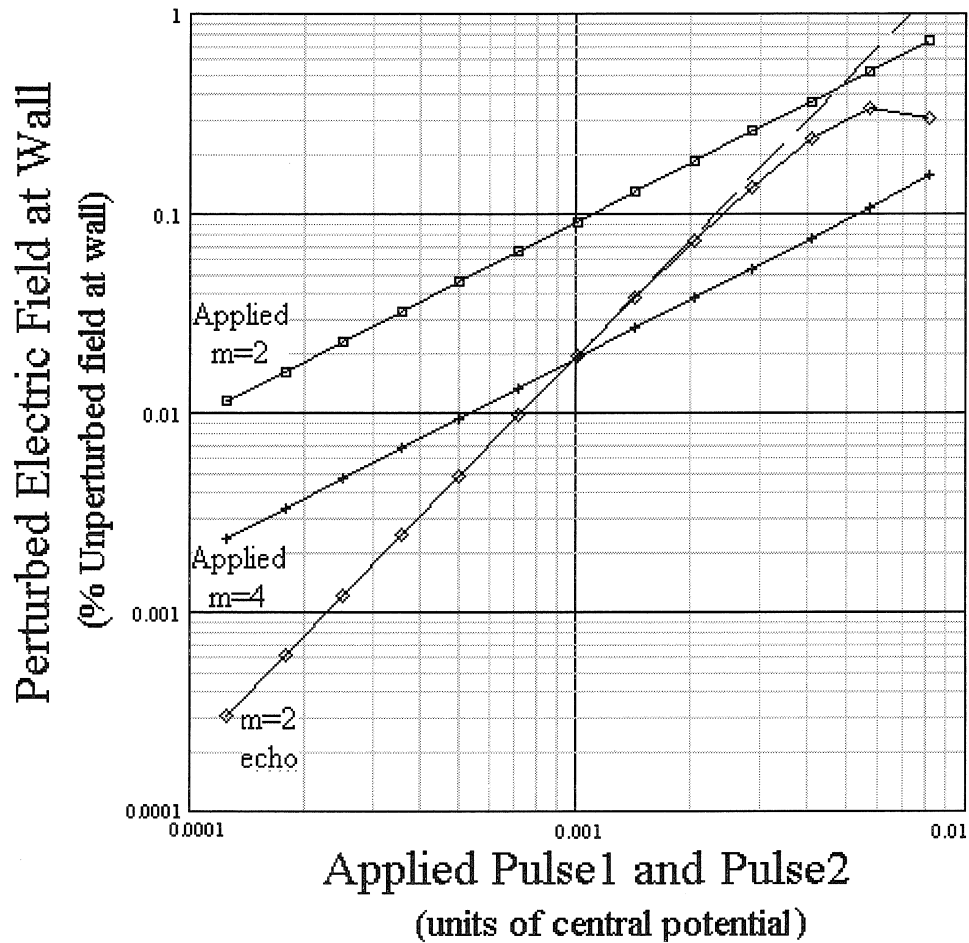


Figure 6.12: Response of the  $m_1 = 2$  pulse,  $m_2 = 4$  pulse, and  $m_3 = 2$  echo response as a function of pulse 1 amplitude (and pulse 2 amplitude divided by 2). For low amplitude pulses, the echo amplitude is proportional to the amplitude of pulse 1 multiplied by the amplitude of pulse 2. For larger pulses, the echo amplitude saturates. The applied amplitudes are varied together, with both amplitudes increased by a factor of  $\sqrt{2}$  from one point to the next. The applied amplitude of the  $m_2 = 4$  pulse always has twice the applied amplitude and half of the pulse duration of the  $m_1 = 2$  pulse. The dashed line has a slope of 2, indicating points that are proportional to the pulse 1 amplitude multiplied by the pulse 2 amplitude.

$$m_3 = h_2 m_2 - h_1 m_1$$

and will occur at time

$$t = \frac{h_2 m_2}{h_2 m_2 - h_1 m_1} \tau$$

where  $h_1$  is the harmonic number for pulse 1, and  $h_2$  is the harmonic number for pulse 2. The echo will have an amplitude dependence

$$A_3 \sim A_1^{h_1} A_2^{h_2} \tau$$

where  $A_3$  is the amplitude of the higher order echo, and  $A_1$  and  $A_2$  represent the amplitudes of pulse 1 and pulse 2. For large amplitudes, these higher order echoes are visible in the results from the Nonlinear Fluid Code.

Figure 6.13 is a plot of the perturbed electric field at the wall for a set of higher amplitude applied pulses. The gap from the plasma edge to the wall was changed for this computation, with  $\alpha = 0.95$ , so the higher  $m$  values could be more easily observed. The first one cycle  $m_1 = 2$  pulse occurs at time  $t = 0$  with an amplitude of  $4.95 \times 10^{-3} \phi_0$ . The second pulse has  $m_2 = 4$  symmetry, an amplitude of  $9.90 \times 10^{-3} \phi_0$ , and occurs at time  $\tau = 17.8t_{cr}$ . An echo occurs with  $m_3 = 2$  symmetry at time  $t = 35.6t_{cr}$ , and reaches a maximum amplitude of 0.384% of the unperturbed electric field at the wall.

An additional echo is also visible in this trace located between the second pulse at  $\tau = 17.8t_{cr}$  and the  $m_3 = 2$  echo at time  $t = 35.6t_{cr}$ . This echo has  $m = 6$  azimuthal symmetry and occurs at time  $t = 23.7t_{cr}$ . This response is a higher order echo caused by the interaction of the fundamental of the first  $m_1 = 2$  pulse,  $h_1 = 1$ , and the second harmonic of the  $m_2 = 4$  pulse,  $h_2 = 2$ . This interaction produces an echo with symmetry  $m_3 = h_2 m_2 - h_1 m_1 = 2 \cdot 4 - 1 \cdot 2 = 6$ , that should occur at time  $t = \frac{h_2 m_2}{h_2 m_2 - h_1 m_1} \tau = \frac{2 \cdot 4}{2 \cdot 4 - 1 \cdot 2} \tau = \frac{4}{3} \tau = 23.7t_{cr}$ .

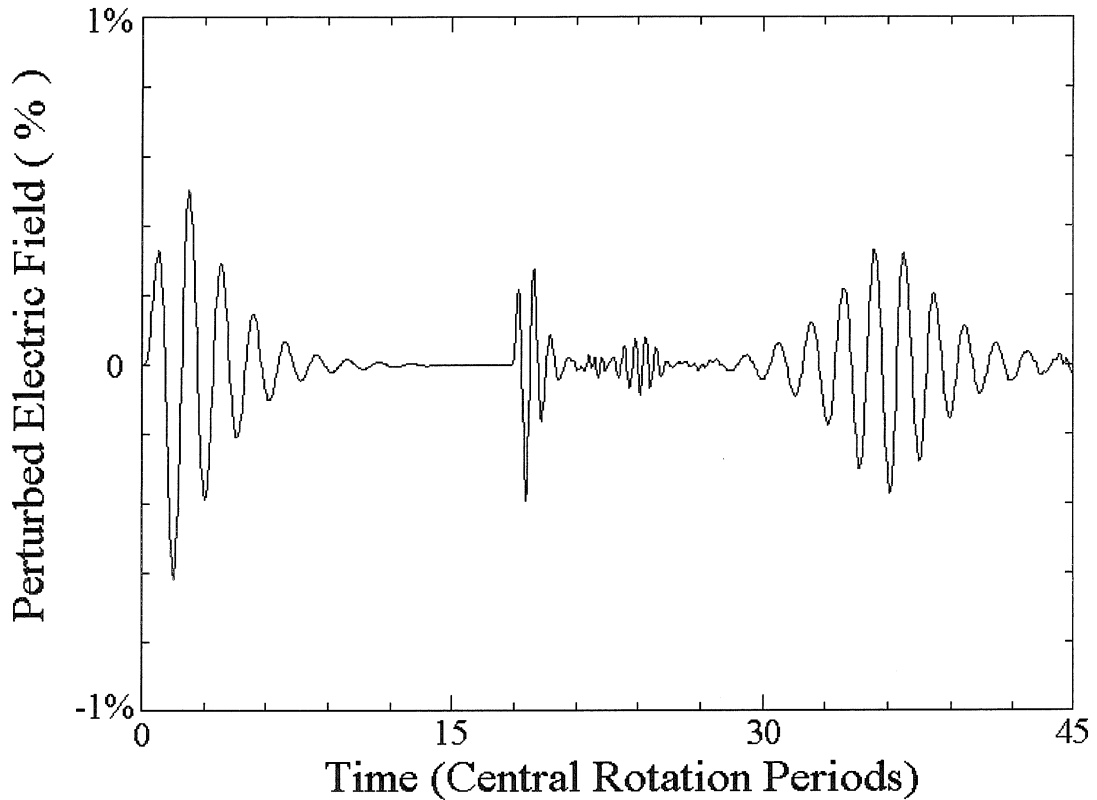


Figure 6.13: Perturbed electric field at the wall versus time for two high amplitude applied pulses. A one cycle  $m_1 = 2$  pulse is applied with amplitude  $4.95 \times 10^{-3} \phi_0$  at time  $t = 0$ , and a one cycle  $m_2 = 4$  pulse is applied with amplitude  $9.90 \times 10^{-3} \phi_0$  at time  $\tau = 17.8t_{cr}$ . An  $m_3 = 2$  echo occurs at time  $t = 35.6t_{cr}$  while a higher order  $m_3 = 6$  echo occurs at time  $t = 23.7t_{cr}$ .

Further higher order echoes are also observable. The Fourier components of the envelope of the perturbed electric field at the wall is plotted on a semilog scale in figure 6.14.

In this plot, the initial  $m_1 = 2$  pulse,  $m_2 = 4$  pulse, and corresponding  $m_3 = 2$  echo have the highest amplitude response in the perturbed electric field at the wall. Additionally, an  $h_1 = 3$  and  $h_1 = 2$  harmonic are visible from the first  $m_1 = 2$  pulse at time  $t = 0$ , and an  $h_2 = 2$  harmonic is visible from the second  $m_2 = 4$  pulse at  $\tau = 17.8$ .

These harmonics can interact to produce further echoes. The  $m_3 = 6$  echo at time

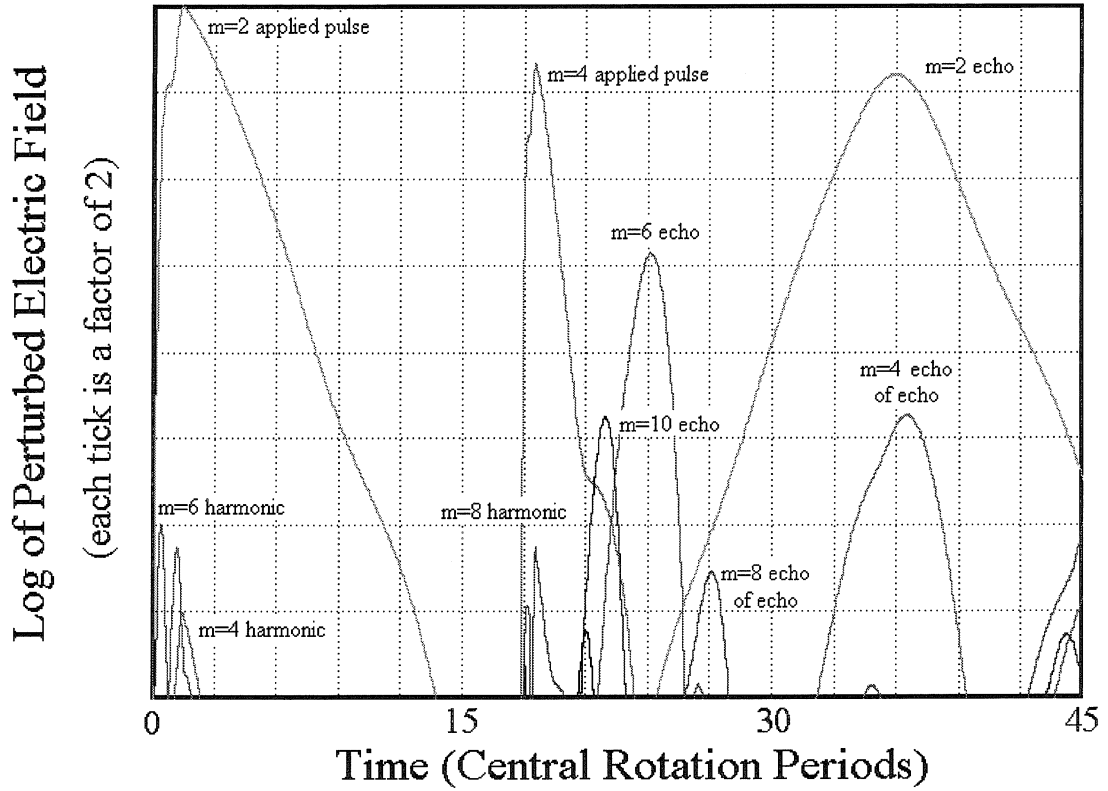


Figure 6.14: Semilog plot of a computation demonstrating higher order echoes. An  $m_1 = 2$  pulse is applied at time  $t = 0$ , and an  $m_2 = 4$  pulse is applied at time  $\tau = 17.8t_{cr}$ . Harmonics of these two pulses, and corresponding echoes are observed.

$t = 23.7t_{cr}$  is produced from the initial  $m_1 = 2$  pulse fundamental  $h_1 = 1$  interacting with the  $h_2 = 2$  harmonic of the second pulse. The  $m_3 = 10$  echo at time  $t = 21.4t_{cr}$  is caused by the initial  $m_1 = 2$  pulse fundamental  $h_1 = 1$  interacting with the  $h_2 = 3$  harmonic of the second pulse.

Echoes of echoes can also occur. The  $m_3 = 8$  response at time  $t = 26.8t_{cr}$  is caused by the initial  $m_1 = 2$  applied pulse fundamental  $h_1 = 1$  interacting with the  $m = 10$  echo at time  $t = 21.4t_{cr}$ . The  $m_3 = 4$  response at time  $t = 35.6t_{cr}$  is caused by the initial  $m_1 = 2$  applied pulse fundamental  $h_1 = 1$  interacting with the  $m = 6$  echo at time  $t = 23.7t_{cr}$ .

The idea of echoes of echoes explains the response occurring near time  $t = 75t_{cr}$

back in figure 6.2. This computation has been computed further in time to 90 central rotation periods, and replotted in figure 6.15.

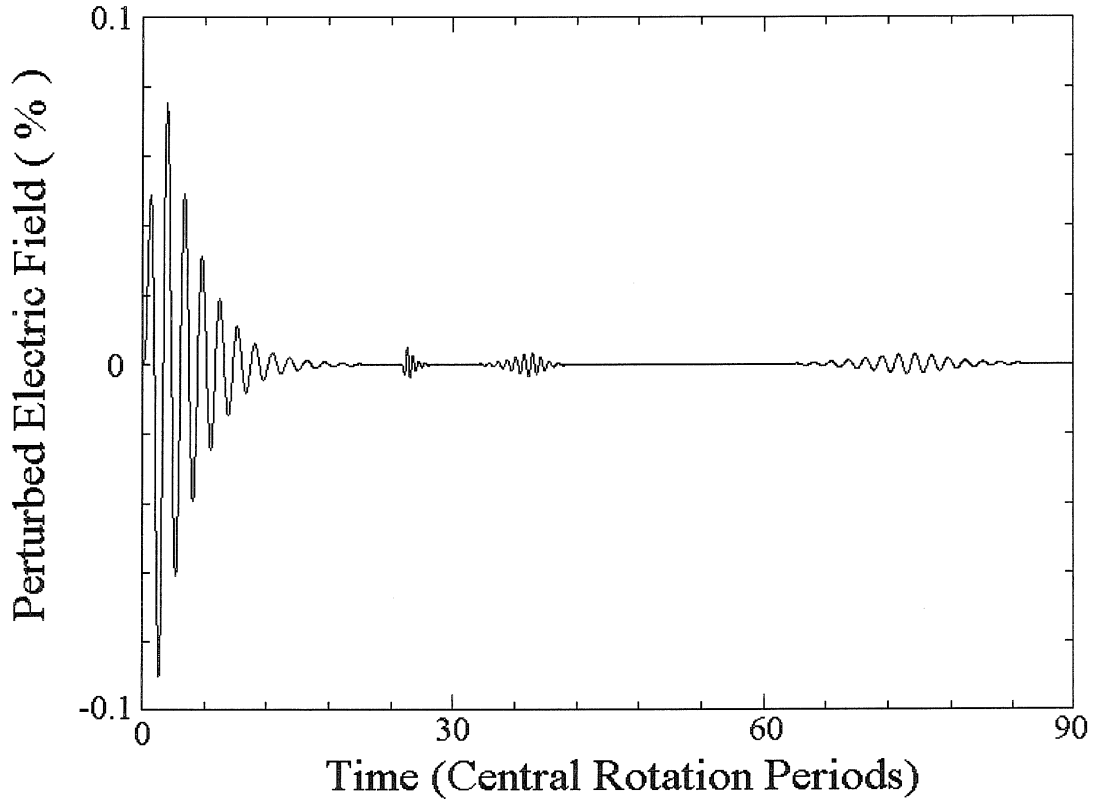


Figure 6.15: Plot of the perturbed electric field at the wall versus time for a one cycle  $m_1 = 2$  applied pulse with amplitude  $1.0 \times 10^{-3}\phi_0$  at time  $t = 0$ , and a one cycle  $m_2 = 6$  applied pulse with amplitude  $3.0 \times 10^{-3}\phi_0$  at time  $\tau = 25t_{cr}$ . An echo occurs at time  $t = 37.5t_{cr}$  with  $m_3 = 4$  azimuthal symmetry. A higher order  $m = 2$  echo occurs at time  $t = 75.0t_{cr}$ .

The applied one cycle  $m_1 = 2$  pulse occurs at time  $t = 0$  with an amplitude of  $1.0 \times 10^{-3}\phi_0$ , and the one cycle  $m_2 = 6$  applied pulse occurs at time  $\tau = 25t_{cr}$  with an amplitude of  $3.0 \times 10^{-3}\phi_0$ . The  $m_3 = 4$  echo occurs at time  $t = 37.5t_{cr}$ . The  $m_3 = 4$  echo then interacts with the  $m_1 = 2$  initial pulse to produce an  $m = 4$  echo of an echo at time  $t = 75.0t_{cr}$ .

The results from the Nonlinear Fluid Code exhibit higher order effects that were not contained in the quasi-linear argument presented in section 5.2. At higher ampli-

tudes, the amplitude of the echo will saturate. Higher order echoes due to harmonics of the applied pulses are also evident and echoes of echoes occur. The next section will briefly discuss the effects of using a different density profile.

### 6.3.5 Slow Decay Density Profile

The echo has been clearly demonstrated using the Fast Decay Profile,  $n_0(r) = n_0(0)\{1 - 3(\frac{r}{\alpha})^2 + 3(\frac{r}{\alpha})^4 - (\frac{r}{\alpha})^6\}$  with  $\alpha = 0.8$ . However, this profile may not be a good representative for density profiles found in a real experiment. The Slow Decay Profile,  $n_0(r) = n_0(0)\{1 - 6(\frac{r}{\alpha})^4 + 8(\frac{r}{\alpha})^6 - 3(\frac{r}{\alpha})^8\}$  with  $\alpha = 0.8$  has a linear decay rate much closer to the value found in the experiment, and is expected to more closely resemble an experimental density profile.

For a one cycle pulse with  $m_1 = 2$  azimuthal symmetry applied at time  $t = 0$  with an amplitude of  $2.14 \times 10^{-4}\phi_0$ , and a second one cycle pulse with  $m_2 = 4$  azimuthal symmetry applied at time  $\tau = 23.7t_{cr}$  with an amplitude of  $1.71 \times 10^{-3}\phi_0$ , an  $m_3 = 2$  echo occurs at time  $t = 47.4t_{cr}$ . The response of the perturbed electric field at the wall is plotted in figure 6.16.

As seen in this figure, an echo with  $m_3 = 2$  azimuthal symmetry occurs at time  $t = 47.4t_{cr}$ , with a perturbed response in the electric field at the wall of 0.00798% of the unperturbed electric field at the wall. Since the first pulse does not decay as quickly for this profile, the echo is not as clearly observed as in the computations using the Fast Decay Profile, but is still evident at time  $t = 47.4t_{cr}$ . The first pulse amplitude was chosen so that the response to the  $m_1 = 2$  pulse decays exponentially without observable nonlinear effects. The second  $m_2 = 4$  pulse was chosen with an applied amplitude 8 times higher than the applied amplitude of the first  $m_1 = 2$  pulse. The previous results involving the time and amplitude dependence of the echo using the Fast Decay Profile also hold for the Slow Decay Profile. Since an echo is also observed using this profile, it should be possible to produce an echo in any profile that has perturbations that decay.

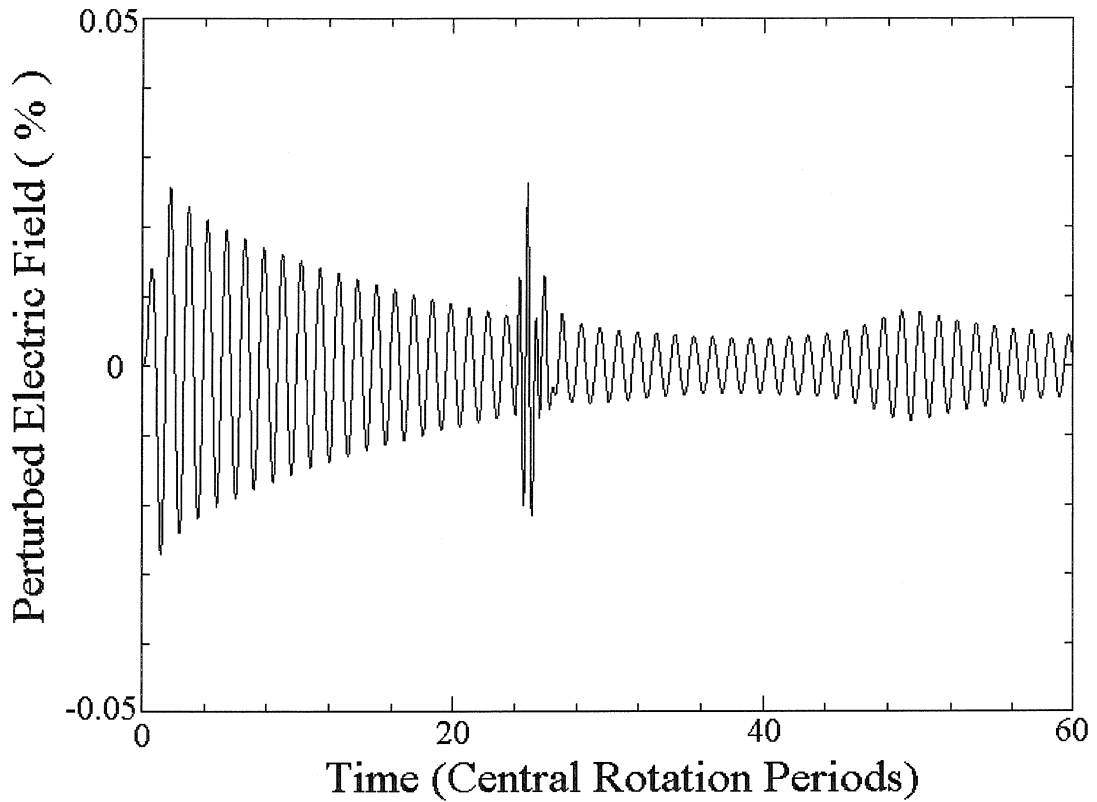


Figure 6.16: Plot of the perturbed electric field at the wall versus time for a computation demonstrating the echo while using the Slow Decay Profile. A one cycle  $m_1 = 2$  pulse with amplitude  $2.14 \times 10^{-4} \phi_0$  is applied at time  $t = 0$ , and a one cycle  $m_2 = 4$  pulse with amplitude  $1.71 \times 10^{-3} \phi_0$  is applied at time  $\tau = 23.7t_{cr}$ . An  $m_3 = 2$  echo occurs at time  $t = 47.4t_{cr}$  and reaches a maximum amplitude of 0.00798% of the unperturbed electric field at the wall.

## 6.4 Conclusion

A pure electron plasma under the fluid approximation can exhibit echoes. For an echo to occur, an applied pulse with  $m_1$  azimuthal symmetry must be followed by a second applied pulse with a higher azimuthal symmetry  $m_2$ . For the first pulse occurring at time  $t = 0$ , and the second pulse at time  $t = \tau$ , an echo will occur at time  $t = \frac{m_2}{m_2 - m_1} \tau$  with  $m_3 = m_2 - m_1$  azimuthal symmetry.

For small applied pulses, the amplitude of the echo is proportional to the amplitude

of the first pulse multiplied by the amplitude of the second pulse. The echo is also proportional to the temporal interpulse spacing of the two pulses,  $\tau$ . For larger applied pulses, the amplitude of the echo will saturate. Also at higher amplitudes, echoes due to harmonics of the two applied pulses and echoes of echoes become visible.

The echo can occur for a density profile which has perturbations that decay by a collisionless phase mixing process. The second applied pulse partially unmixes the density perturbations of the first pulse, producing an echo later in time. Echoes were found to occur for a density profile that should be similar to a profile found in the experiment. This suggests that an experimental search for echoes may be successful.

Nonideal fluid effects (transport phenomena) such as diffusion and viscosity are expected to dissipate the echo at later times. If echoes are found experimentally, measurement of the echo amplitude as a function of interpulse spacing may provide a diagnostic to measure these additional effects.

# Chapter 7 Beat-Wave Decay Instability

## 7.1 Introduction

This chapter presents preliminary results from the Nonlinear Fluid Code describing a decay instability that occurs at very large amplitudes of the applied pulse. This is quite a different phenomena from the results studied in the previous chapters, and presents another example where the Nonlinear Fluid Code can be used to study a phenomena that occurs in non-neutral plasmas.

In Chapter 5 we observed a modulation of the decay envelope caused by non-linear fluid trapping. Although nonlinear trapping of fluid occurred, these plasma perturbations were not visible in images of the total density. Only by subtracting out the average density could the plasma dynamics be observed. This chapter will discuss the response of the plasma to very high amplitude applied pulses. For these high amplitude pulses, the perturbation to the plasma is visible in images of the total density.

Such high amplitude perturbations in a pure electron plasma are subject to a decay instability. Mitchell and Driscoll [22] performed an experiment which demonstrated that a perturbation with azimuthal symmetry mode number  $m$  and angular frequency  $\omega_m$  could decay into a mode  $m - 1$  with angular frequency  $\omega_{m-1}$ , provided the beat frequency  $\omega_m - \omega_{m-1}$  exists in a frequency range associated with a resonant radius that is within the plasma. This decay is related to the three oscillator parametric instability, and a theoretical discussion of this decay mechanism may be found in [36].

Density and electric potential may be decomposed into a Fourier series with  $n(r, \theta) = \sum n_m(r)e^{im\theta}$ , and  $\phi(r, \theta) = \sum \phi_m(r)e^{im\theta}$ . The component of density  $n(r, \theta)$  with azimuthal symmetry  $m$  is given by

$$n_m(r) = \frac{1}{2\pi} \int_0^{2\pi} n(r, \theta) e^{-im\theta} d\theta$$

and the component of the electric potential  $\phi(r, \theta)$  with azimuthal symmetry  $m$  is given by

$$\phi_m(r) = \frac{1}{2\pi} \int_0^{2\pi} \phi(r, \theta) e^{-im\theta} d\theta.$$

A normalized density amplitude component  $A_m$  for a mode with azimuthal symmetry  $m$  was defined by Mitchell and Driscoll as

$$A_m^2 = \frac{\int_0^{r_w} r |n_m(r)|^2 dr}{\int_0^{r_w} r |n_0(r)|^2 dr} \quad (7.1)$$

where  $n_0(r)$  is the unperturbed density profile and  $r_w$  is the radius of the wall. They found the  $m - 1$  mode to grow at the expense of the mode  $m$ , with the rate of change given by

$$\frac{d}{dt} A_{m-1} = (-\gamma_{m-1} + \Gamma_{m,m-1} A_m^2) A_{m-1} \quad (7.2)$$

where  $\gamma_{m-1}$  is the linear decay rate for the mode  $m - 1$ , and  $\Gamma_{m,m-1}$  is the coupling rate between mode  $m$  and mode  $m - 1$  which is independent of amplitude  $A_m$  for small values of  $A_m$ . When  $\Gamma_{m,m-1} A_m^2 > \gamma_{m-1}$ , expression 7.2 leads to exponential growth.

Figure 7.1 is a reproduction of the main experimental results from Mitchell and Driscoll. The figure plots the daughter mode growth rate  $\gamma_{m-1}$  versus the normalized parent mode amplitude  $A_m$ , and shows the growth is approximately proportional to  $A_m^2$ .

Currently, the beat-wave decay instability is not well understood. Theoretical calculations of the mode coupling rates  $\Gamma_{i,j}$  do not agree well with the experiment [37]. In order to address this problem, the Nonlinear Fluid Code was used to study

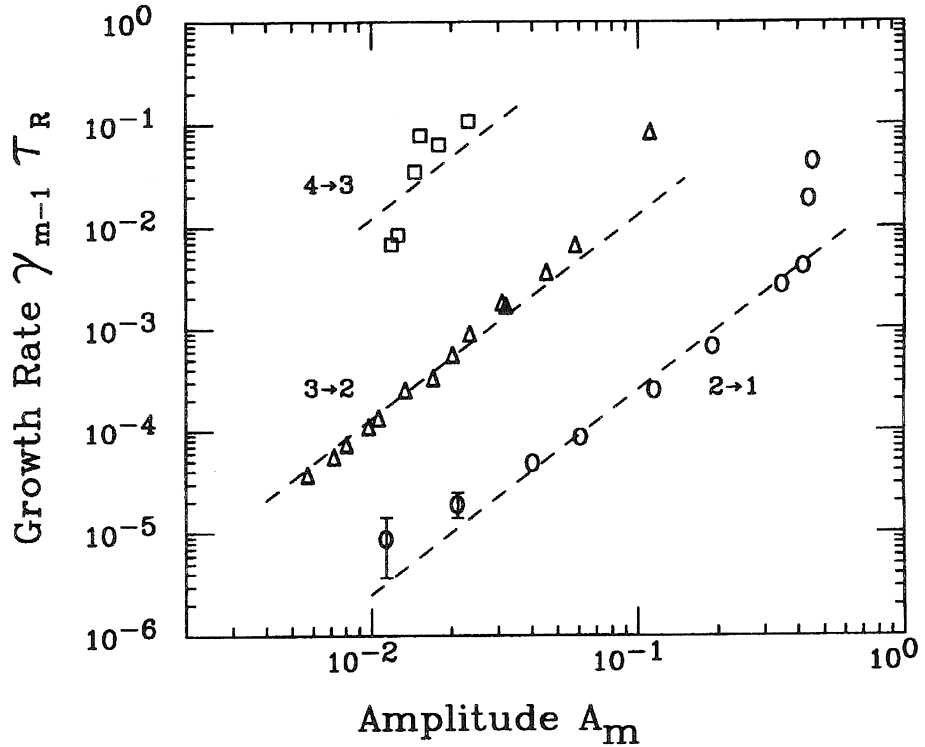


Figure 7.1: Experimental results of Mitchell and Driscoll on the beat-wave decay instability in a pure electron plasma. The measured growth rates  $\gamma_{m-1}$  for daughter mode  $m - 1$  versus normalized amplitude  $A_m$  of the parent mode, for  $m = 2, 3$ , and  $4$ . The growth rates are scaled by the central rotation time  $t_{cr} = 5.5\mu s$ . The dashed lines indicate  $\gamma_{m-1} = \Gamma_{m,m-1} A_m^2$ .

the beat-wave decay instability, and determine if the numerical results agree with the experiment. The Nonlinear Fluid Code results are presented in the next section.

## 7.2 Fluid Code Results

### 7.2.1 Choice of Density Profile

The density profile was chosen to approximate the experimental profile measured by Mitchell and Driscoll [22]. The normalized Fermi function density profile with the parameter  $\beta = 8$ , given by equation 4.1 in Chapter 4, is a close approximation to the density profile measured in the experiment. This density profile and the corresponding

angular velocity profile are shown in figure 7.2. In Chapter 4, this density profile was named the Beat Profile, and was found to have an  $m = 2$  resonant frequency of  $\omega_2 = 1.012\omega_0(0)$  corresponding to a resonant radius of  $r_s = 0.703r_w$  and a linear decay rate of  $\gamma_2 = 0.00302\omega_0(0)$ . A small amplitude computation with an  $m = 3$  perturbation was performed using this profile which resulted in an  $m = 3$  resonant frequency of  $\omega_3 = 1.858\omega_0(0)$  corresponding to a resonant radius of  $r_s = 0.635r_w$  and a linear decay rate of  $\gamma_3 = 0.0446\omega_0(0)$ . The  $m = 1$  resonant frequency is given by the angular velocity at the wall, and is equal to  $\omega_r = 0.250\omega_0(0)$ . The beat frequency between the  $m = 3$  resonance and the  $m = 2$  resonance is  $0.846\omega_0(0)$ , and occurs at radius  $0.534\omega_0(0)$ . This profile has a central electric potential of  $\phi_0 = -0.147522\frac{e}{\epsilon_0}n_0(0)r_w^2$ , and an unperturbed electric field at the wall of  $-0.125047\frac{e}{\epsilon_0}n_0(0)r_w$ .

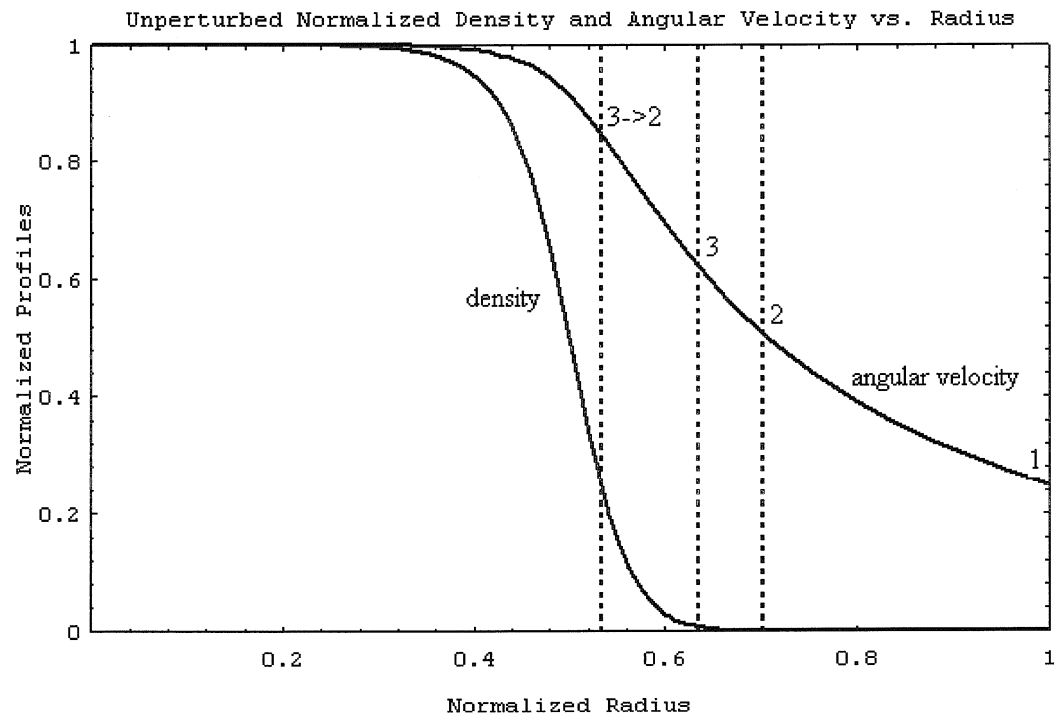


Figure 7.2: Plot of the normalized density and normalized angular velocity for the Beat Profile. The  $m = 2$  and  $m = 3$  resonant radius, and the radius for the beat frequency between these two modes are indicated by the dotted lines. The  $m = 1$  resonant frequency is given by the angular velocity at the wall.

### 7.2.2 Demonstration of the Decay Instability

This section presents results from the Nonlinear Fluid Code for a computation that demonstrates the beat-wave decay instability. A high amplitude  $m = 3$  perturbation is observed to decay into an  $m = 2$  perturbation through an interaction with the beat frequency between these two perturbations.

The Nonlinear Fluid code was used to study the response of a pure electron plasma to a large amplitude externally applied  $m = 3$  pulse. The plasma is first seeded with a weak one cycle burst of voltage with  $m = 2$  azimuthal symmetry and an amplitude of  $1.0 \times 10^{-3}\phi_0$ . Directly after the one cycle weak  $m = 2$  pulse, a one cycle burst of voltage with  $m = 3$  azimuthal symmetry and a large amplitude of  $0.25\phi_0$  is applied to the plasma. The electric field at the wall for the  $m = 3$  mode reaches a maximum amplitude of 5.68% of the unperturbed electric field at the wall.

A plot of the perturbed electric field at the wall versus time is plotted on a semilog scale in figure 7.3. In this figure, the decay of the  $m = 3$  mode and growth of the  $m = 2$  mode is clearly visible. Additional nonlinear effects, which may be bounce oscillations, are also observed. The  $m = 2$  mode is found to have a growth rate of  $\gamma_2 = 0.038\omega_0(0)$ .

The decay of the  $m = 3$  mode and growth of the  $m = 2$  mode is also visible in images of the total density. Figure 7.4 plots the total density for six successive times. A clear transition is seen from a mode with  $m = 3$  azimuthal symmetry to a mode with  $m = 2$  azimuthal symmetry. Images (a)-(f) correspond to the times  $2.47t_{cr}$ ,  $6.92t_{cr}$ ,  $11.4t_{cr}$ ,  $15.8t_{cr}$ ,  $20.3t_{cr}$ , and  $24.7t_{cr}$ , respectively.

### 7.2.3 Growth Rate Versus Amplitude

This section examines the growth rate of the  $m = 2$  daughter mode as a function of the  $m = 3$  parent mode amplitude. Five computations were performed, varying the amplitude of the applied  $m = 3$  pulse. Each computation is seeded with an initial one cycle pulse with  $m = 2$  symmetry and amplitude  $1.0 \times 10^{-3}\phi_0$ , directly followed by the larger  $m = 3$  pulse. The perturbed electric field at the wall for the computation

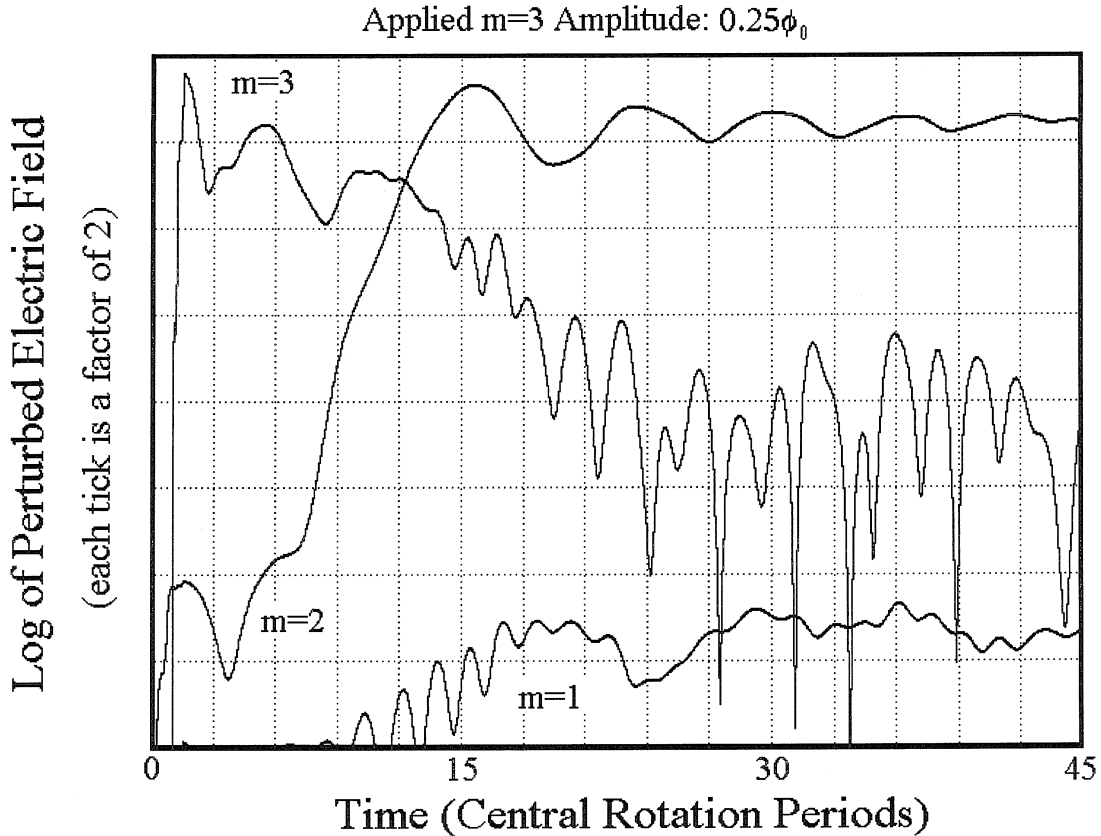


Figure 7.3: Plot of the envelope of the perturbed electric field at the wall versus time on a semilog scale for the  $m = 1, 2$  and  $3$  Fourier components due to a large applied pulse with  $m = 3$  azimuthal symmetry. The beat-wave decay instability causes the decay of the  $m = 3$  mode and growth of the  $m = 2$  mode.

using an applied  $m = 3$  amplitude of  $0.250\phi_0$  was shown in figure 7.3. The perturbed electric field at the wall for the remaining four computations using an applied  $m = 3$  amplitude of  $0.177\phi_0$ ,  $0.125\phi_0$ ,  $0.0884\phi_0$ , and  $0.0625\phi_0$  is shown in figure 7.5. The normalized amplitude  $A_3$  is proportional to the applied wall potential.

The initial  $m = 3$  density amplitude  $A_3$  is computed using equation 7.1, and the corresponding growth rate of the  $m = 2$  amplitude  $A_2$  is estimated. To determine an  $m = 2$  growth rate from the curves in figure 7.5 is difficult at best, so the growth rates are not very accurate. The results are summarized in table 7.1.

The first column is the amplitude of the one cycle applied  $m = 3$  pulse, and the

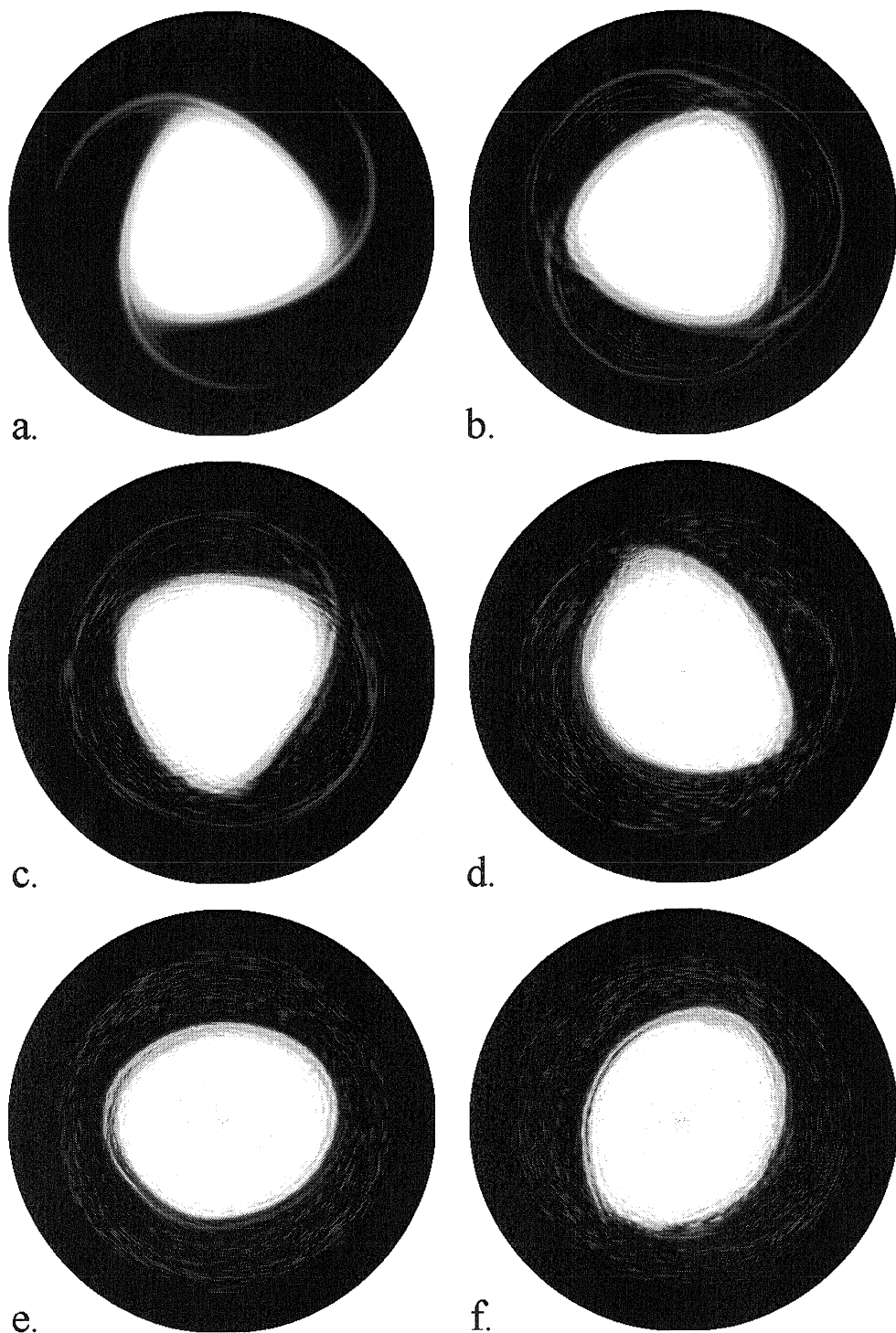


Figure 7.4: Images of the total density at times  $2.47t_{cr}$ ,  $6.92t_{cr}$ ,  $11.4t_{cr}$ ,  $15.8t_{cr}$ ,  $20.3t_{cr}$ , and  $24.7t_{cr}$ , after excitation from a large pulse with  $m = 3$  azimuthal symmetry. Due to beat-wave resonance damping, the  $m = 3$  mode decays into an  $m = 2$  mode.

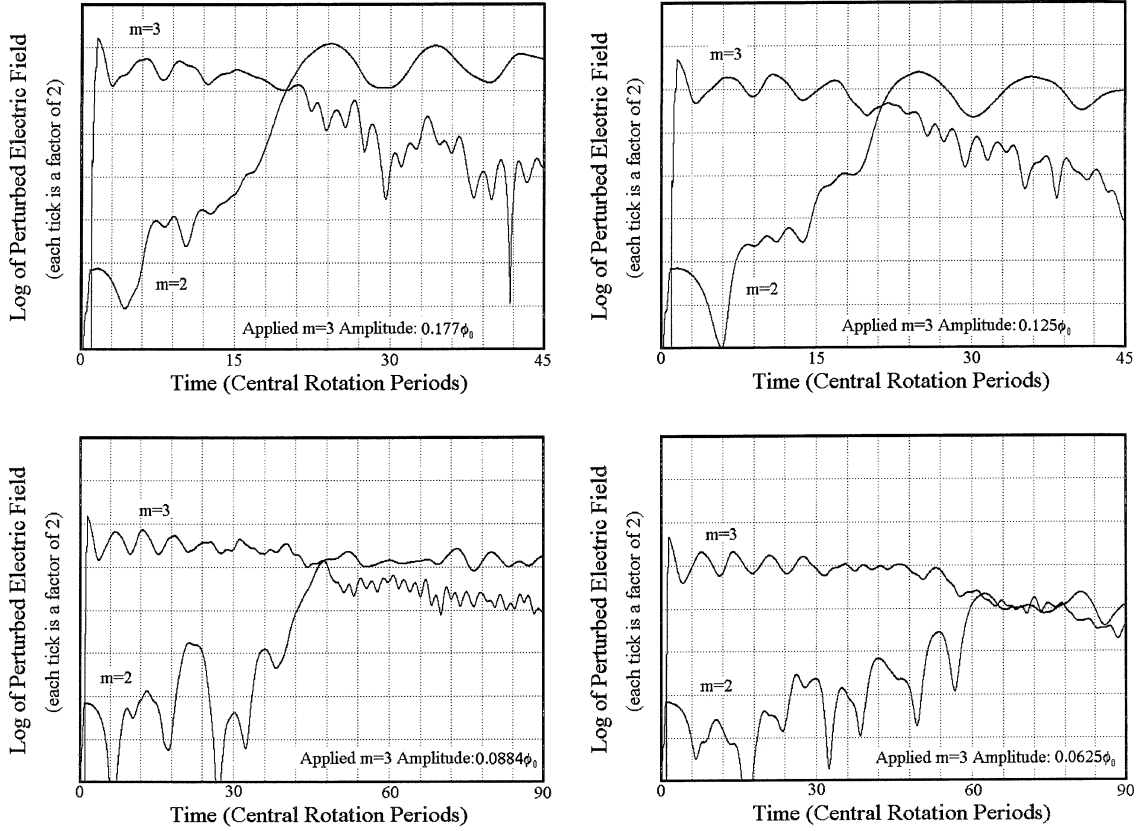


Figure 7.5: Plot of the envelope of the perturbed electric field at the wall for the  $m = 3$  and  $m = 2$  mode versus time on a semilog scale. The  $m = 2$  mode has an initial applied amplitude of  $0.001\phi_0$ , and the  $m = 3$  mode has an amplitude of  $0.177\phi_0$ ,  $0.125\phi_0$ ,  $0.0884\phi_0$ , and  $0.0625\phi_0$  in the four traces. The time scale has been doubled in the lower two figures.

second column is the resulting maximum perturbed electric field at the wall for the  $m = 3$  mode. The third column  $A_3$  is the maximum  $m = 3$  mode density amplitude given by equation 7.1.

The  $m = 2$  growth rate was computed using a least squares fit of a straight line to the logarithm of the perturbed electric field over the time just after the end of the  $m = 3$  pulse to the time of the maximum amplitude of the  $m = 2$  mode. As seen from figure 7.5, the perturbed electric field at the wall for the  $m = 2$  mode has many features and the logarithm of the perturbed field is not well fit by a straight line, so the computed growth rates are not very accurate. The fourth column of table

$m = 3$ Amplitude	Perturbed field	$A_3$	$\gamma_2$
$0.0625\phi_0$	1.32%	0.0505	$0.0045\omega_0(0) = 0.028\frac{1}{t_{cr}}$
$0.0884\phi_0$	1.88%	0.0703	$0.0078\omega_0(0) = 0.049\frac{1}{t_{cr}}$
$0.125\phi_0$	2.69%	0.105	$0.024\omega_0(0) = 0.15\frac{1}{t_{cr}}$
$0.177\phi_0$	3.87%	0.141	$0.026\omega_0(0) = 0.17\frac{1}{t_{cr}}$
$0.250\phi_0$	5.68%	0.184	$0.038\omega_0(0) = 0.24\frac{1}{t_{cr}}$

Table 7.1: Growth rate of the  $m = 2$  mode as a function of  $m = 3$  mode initial amplitude.

7.1 is the calculated  $m = 2$  mode growth rate normalized to the central rotation frequency and to the central rotation period, so an easy comparison can be made to the paper by Mitchell and Driscoll [22]. As the amplitude of the applied  $m = 3$  pulse is increased, the growth rate of the  $m = 2$  mode is found to increase, with the  $m = 2$  mode becoming the dominant mode earlier in time at higher amplitudes.

The  $m = 2$  growth rate  $\gamma_2$  versus  $m = 3$  mode amplitude  $A_3$  is plotted on a log-log scale in figure 7.6. The straight line in figure 7.6 has slope 2, indicating  $\gamma_2 = \Gamma_{3,2}A_3^2$ . A least squares fit to the points has a slope of  $1.7 \pm 0.1$ , but this error does not account for the large uncertainty in the estimated growth rates. Using the slope 2 fit, the coupling constant is calculated to be  $\Gamma_{3,2} = 10.5\frac{1}{t_{cr}} \pm 2.4\frac{1}{t_{cr}}$ .

#### 7.2.4 Comparison to Experimental Results

Comparing the amplitudes of the  $m = 3$  mode with the amplitudes used in the experiment by Mitchell and Driscoll, it is found that the amplitudes used in the computation are near the highest amplitude experimental runs. The experimental coupling constant is  $\Gamma_{3,2} = 1.3\frac{1}{t_{cr}}$ , while the numerical results give a coupling constant and growth rates that are 8 times higher. The experimental data has a single point that does not fall along the trend line of the other experimental points. This highest amplitude experimental result has an amplitude of  $A_3 = 0.11$ , and a corresponding  $m = 2$  growth rate of  $\gamma_2 = 0.09\frac{1}{t_{cr}}$  which differs by less than a factor of two from the computation with amplitude  $A_3 = 0.105$  and a corresponding  $m = 2$  growth rate of  $\gamma_2 = 0.15\frac{1}{t_{cr}}$ . At these amplitudes, the coupling constant may not be independent

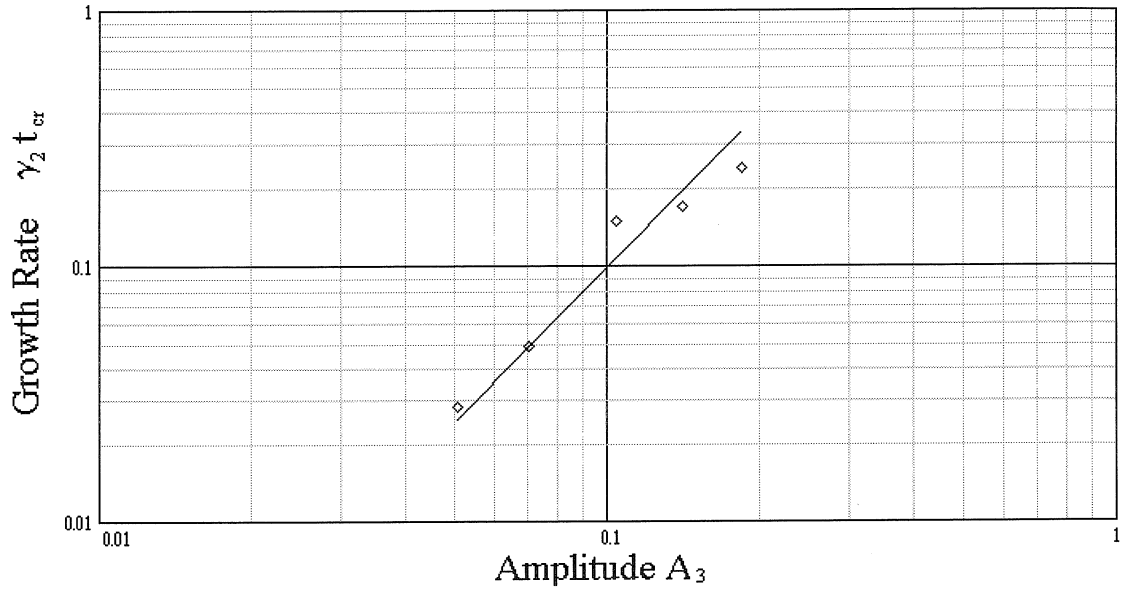


Figure 7.6: Estimated growth rates  $\gamma_2$  for daughter mode  $m = 2$  normalized to the central rotation time versus normalized amplitude  $A_3$  of parent mode  $m = 3$ . The straight line indicates  $\gamma_2 = \Gamma_{3,2} A_3^2$ .

of amplitude. The computational growth rates and experimental growth rates are plotted versus parent amplitude on the same scale in figure 7.7.

In the experiment it was found for high applied  $m = 3$  amplitudes, the  $m = 2$  mode grows faster than  $A_3^2$ . However, for the amplitudes used in the computation, the  $m = 2$  mode was found to grow slower than  $A_3^2$ .

Some differences exist between the experiment and the computation. First, the exact density profile of the experiment was not used in the computation, but rather a smooth Fermi function approximation of it. The growth rate is expected to be sensitive to  $\frac{dn_0}{dr}$  at the beat resonant radius. Second, the  $m = 2$  mode was seeded with a moderate amplitude in the computation, whereas in the experiment, the  $m = 2$  mode must grow from noise. These factors may account for the differences in the results between the computation and the experiment. Additionally, the  $m = 2$  mode growth is not very smooth in this high amplitude range, so the estimation of the growth rates is not very accurate. It is not possible to use lower applied amplitudes in the computation since the slower growth rates would require computing further in

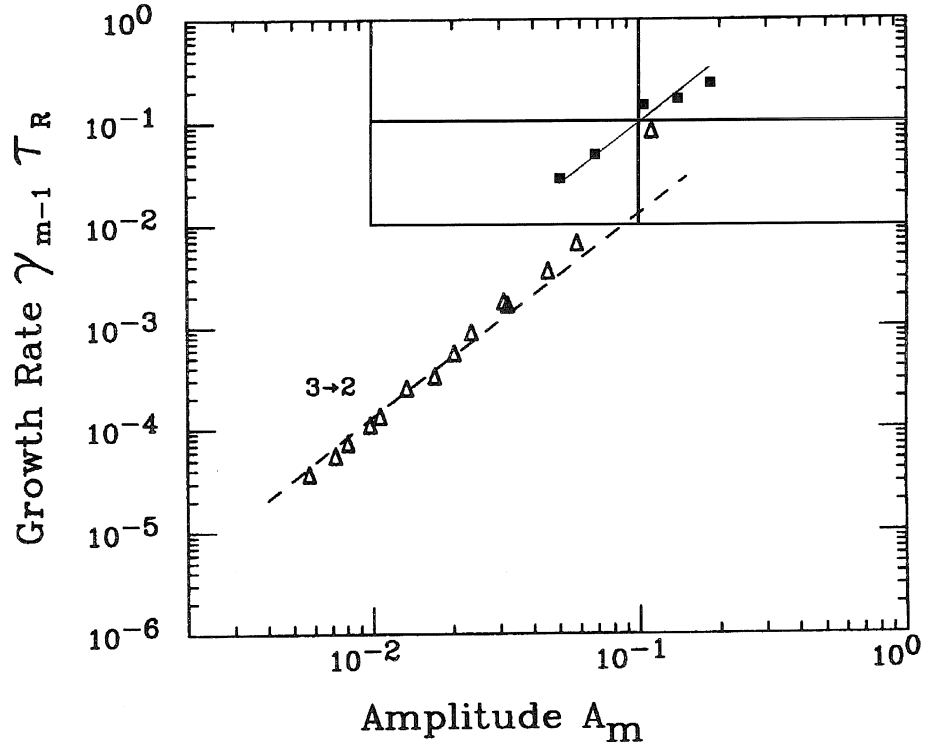


Figure 7.7: Plot of the experimental and computational growth rates for the  $m = 2$  daughter mode versus parent mode  $m = 3$  amplitude. The experimental data of Mitchell and Driscoll [22] is represented by triangles, and the computational data is represented by squares. The upper right section of the graph is the same scale shown in figure 7.6. Higher growth rates were observed in the computation.

time, which is not practical due to the necessary computational time and accumulation of errors.

### 7.3 Conclusion

The experimentally observed beat-wave resonance damping was successfully observed using the Nonlinear Fluid Code. The growth rates of the daughter wave are larger in the computation than in the experiment, with the coupling constant 8 times higher than the experimental value.

The growth rate is not easily computed for the five computations discussed in this section. Additional nonlinear phenomena cause fluctuations in the envelope of the

$m = 2$  mode as a function of time which degrade the least squares fit for the growth rate. For the amplitudes used in the computation, the coupling constant may not be independent of amplitude.

The results presented in this chapter are only preliminary. More work is necessary to understand beat-wave resonance damping, the source of the variations in the computed growth rate, and the discrepancies with the experiment. Further work may resolve the difference between the growth rates found from the experiment and the growth rates found from the computation.

# Chapter 8 Conclusion and Future Work

## 8.1 Summary of Results

A cylindrical pure electron plasma can under certain approximations be described by the equations for a two-dimensional, incompressible, inviscid fluid. By applying numerical techniques to these equations, a two-dimensional, cylindrical, nonlinear fluid code was created and used to study the response of a pure electron plasma to various externally applied pulses.

For small amplitude pulses, the response of the plasma, quantified by the perturbed electric field at the wall, was found to decay exponentially in time. The decay rate is strongly dependent on the density profile used in the calculation. The decay is caused by a collisionless phase mixing process, due to differential rotation of the plasma at different radii. This mixing process is clearly illustrated in successive images of the perturbed density. As expected, the results from the Nonlinear Fluid Code agree with linearized calculations for these small amplitude pulses.

For moderate amplitude pulses, fluid elements are trapped within the potential well of the resulting wave. The circulation of the trapped fluid elements in the well causes a modulation of the decay envelope, a phenomenon which is illustrated in images of the perturbed density. For a slowly applied pulse, a perturbation, which is nearly stationary in the wave frame, similar to a BGK mode, is excited.

For two small amplitude pulses that are separated in time, the code also shows that an echo may occur after the second pulse. The response to the first pulse will decay by the collisionless phase mixing process and the response to the second pulse will also decay by this process. A nonlinear interaction between the two applied pulses can then generate an echo response. Based on a simplified theory, several aspects of echo behavior have been predicted and verified with the fluid code. An echo can only occur if the azimuthal mode number of the second pulse is greater than that

of the first pulse. A nonlinear interaction between the two applied pulses allows the echo to form, with the second pulse partially unmixing the first pulse. The echo has azimuthal mode number  $m_2 - m_1$  and occurs at time  $t = m_2\tau/(m_2 - m_1)$ , where the first pulse of  $m_1$  azimuthal symmetry occurs at time  $t = 0$ , and the second pulse of  $m_2$  azimuthal symmetry occurs at time  $t = \tau$ . The amplitude of the echo is proportional to the amplitude of the first pulse, the amplitude of the second pulse, and the time between the two applied pulses,  $\tau$ . For larger pulses, the echo amplitude saturates. Echoes due to the interaction with various harmonics, and echoes of echoes can also occur.

Very large perturbations are known to be subject to a decay instability based on previous experimental work. A parent wave with azimuthal symmetry  $m$  can decay to a daughter wave with  $m - 1$  symmetry by an interaction with the beat frequency between the two waves. The growth rates seen in the computation are higher than the growth rates reported in the experiment, and the coupling constant for the daughter wave is 8 times higher than the experimentally derived value.

## 8.2 Further Work

As with any area of research, for every question answered, many new questions are generated. This section will highlight some of the questions which still remain for further research.

### 8.2.1 Improvements to the Nonlinear Fluid Code

The Nonlinear Fluid Code presented in this thesis is very useful for studying nonlinear phenomena in non-neutral plasmas. Improvements to the Nonlinear Fluid Code could be made by adding additional physics to the code, and by changing some of the computational methods. Some possible improvements are presented in this section.

## Viscosity

Viscosity was neglected in the Nonlinear Fluid Code. However, viscosity may be an important effect in real plasmas. It is expected that over long time scales viscosity will destroy the fine scale structure due to mixing. This would reduce the amplitude of the echo. A careful study including the effects of viscosity on the echo could provide a diagnostic for measuring the viscosity in experimental plasmas.

## Higher Order Effects

The pressure gradient, diamagnetic drift, polarization drift, and other thermal effects were neglected in the Nonlinear Fluid Code. These effects should be included to see whether they change the results significantly. For an experimental plasma with density profiles similar to those studied in this thesis, the diamagnetic drift velocity may not be negligible compared to the  $\vec{E} \times \vec{B}$  drift velocity. The diamagnetic drift does not seem necessary to describe the nonlinear phenomena studied here, but it may cause effects that could be quantitatively measured. A modification to the Nonlinear Fluid Code should be able to explore the differences due to thermal effects.

## Fourth Order Runge-Kutta Time Integration

The time integration method could be improved by using a fourth order Runge-Kutta time integration method. For the same size time step, the fourth order method should be much more accurate than the second order leapfrog method used in the Nonlinear Fluid Code. However, the necessary computational time is doubled for the same time step.

## Spectral Code

The accuracy of the Nonlinear Fluid code could be greatly improved by using spectral methods to solve the 2-D fluid equations. The azimuthal direction can be represented as a Fourier series, and the radial direction can be represented by a summation of Chebyshev polynomials. Such a spectral code would not contain the same aliasing

errors that exist in the finite difference methods of the current Nonlinear Fluid Code. However, a much smaller time step would be required to maintain computational stability, resulting in much longer computational time. With the use of faster computers, a spectral code may be practical.

### 8.2.2 Further Research on Non-neutral Plasmas

#### Fluid Trapping

It was shown that fluid elements could be trapped in an excited wave of moderate amplitude. This trapping has not been explored as a function of density profile. A different density profile may better match the experimental results of Pillai [14], including the asymptotic decay at much later times.

For a small amplitude pulse applied for 90 cycles, a perturbation that is nearly stationary in the wave frame and resembles a BGK mode is excited. Future computations may be capable of applying a pulse over a much longer duration, perhaps exciting a true BGK mode that is stationary in the wave frame. It may also be possible to find an analytical expression describing a BGK mode in a non-neutral plasma.

#### Echoes

For short times between pulses, the amplitude of the echo is proportional to the interpulse spacing. For longer times, the echo amplitude saturates. The amplitude dependence for large interpulse spacing remains unexplored. Such computations require increased resolution to accurately compute further in time.

Results from the Nonlinear Fluid Code suggest that echoes may be observable experimentally. For sufficiently large pulses, the echo amplitude can approach the amplitude of the response to the applied pulses. Based on these results, a future experimental search for echoes may be successful.

### Beat-Wave Resonance Damping

Many questions remain regarding the beat-wave resonance damping results. What causes the modulation in the growth of the  $m = 2$  mode? Why are growth rates found from the computation higher than growth rates found in the experiment? Transitions other than the  $m = 3$  to  $m = 2$  have not yet been explored with the Nonlinear Fluid Code. The dependence on the density profile is unknown, and the growth rate is probably quite sensitive to  $\frac{d n_0}{d r}$  at the beat-wave resonant radius. It should be possible to construct a density profile where the  $m = 3$  mode and the  $m = 2$  mode are undamped. For such a profile, the  $m = 2$  mode will grow unhindered by the linear decay mechanism, and beat-wave resonance damping could be studied for smaller applied pulses.

### Other Phenomena

Many other nonlinear phenomena that occur in non-neutral plasmas can be studied using the Nonlinear Fluid Code. The hollow beam instability, vortex mergers and vortex crystals are a few examples of other phenomena that could be examined. It is expected that this code will be an important new tool to be used in future research on these plasmas.

## Bibliography

- [1] R. G. Greaves, M. D. Tinkle, and C. M. Surko, Phys. Plasmas **1**, 1439 (1994).
- [2] G. Gabrielse, Sci. Am. **267**, 78 (1992).
- [3] J. J. Bollinger, D. J. Prestage, W. M. Itano, and D. J. Wineland, Phys. Rev. Lett. **54**, 1000-1003 (1985).
- [4] T. B. Mitchell, M. M. Schauer, and D. C. Barnes, Bull. Am. Phys. Soc. **41**, 1603 (1996).
- [5] L. Brillouin, Phys. Rev. **67**, 260 (1945).
- [6] H. F. Webster, J. Appl. Phys. **26**, 1386 (1955).
- [7] G. G. McFarlane and H. G. Hay, Proc. Phys. Soc. **63**, 409 (1953).
- [8] A. H. W. Beck, *Space Charge Waves and Slow Electromagnetic Waves* (Pergamon Press, 1958).
- [9] R. H. Levy, Phys. Fluids **8**, 1288 (1965).
- [10] R. J. Briggs, J. D Daugherty, and R. H. Levy, Phys. Fluids **13**, 421 (1970).
- [11] L. Landau, J. Phys. (Moscow) **10**, 25 (1946).
- [12] J. H. Malmberg and J. S. deGrassie, Phys. Rev. Lett. **35**, 577 (1975).
- [13] C. F. Driscoll and K. S. Fine, Phys. Fluids B **2**, 1359 (1990).
- [14] N. S. Pillai and R. W. Gould, Phys. Rev. Lett. **73**, 2849 (1994).
- [15] N. R. Corngold, Phys. Plasmas **2**, 620 (1995).
- [16] R. L. Spencer and S. N. Rasband, Phys. Plasmas **4**, 53 (1997).

- [17] C. W. Roberson and C. F. Driscoll, *Non-Neutral Plasma Physics*, AIP Conf. Proc. No. 175 (American Institute of Physics, New York, 1988).
- [18] J. Fajans and D. H. E. Dubin, *Non-Neutral Plasma Physics II*, AIP Conf. Proc. No. 331 (American Institute of Physics, Woodbury, 1995).
- [19] N. S. Pillai, Ph.D. thesis, California Institute of Technology (1995).
- [20] I. B. Bernstein, J. M. Greene, and M. D. Kruskal, Phys. Rev. **108**, 546 (1957).
- [21] R. W. Gould, Phys. Plasmas **2**, 2151 (1995).
- [22] T. B. Mitchell and C. F. Driscoll, Phys. Rev. Lett. **73**, 2196 (1994).
- [23] Charles K. Birdsall and A. Bruce Langdon, *Plasma Physics via Computer Simulation* (McGraw-Hill, 1985).
- [24] William H. Press, Brian P. Flannery, Saul A. Teukolsky, and William T. Vetterling, *Numerical Recipes, The Art of Scientific Computing* (Cambridge University Press, 1986).
- [25] N. A. Phillips, Quart. J. Roy. Meteorol. Soc. **82**, 123-164 (1956).
- [26] N. A. Phillips, *The Atmosphere and the Sea in Motion* (Rockefeller Institute Press and the Oxford Univ. Press, New York, 1959) pp. 501-504.
- [27] A. Arakawa, J. Comput. Phys. **1**, 119 (1966).
- [28] K. M. Case, Phys. Fluids **3**, 143 (1960).
- [29] W. Thompson, Nature **23**, 45 (1880).
- [30] E. L. Hahn, Phys. Rev. **80**, 580 (1950).
- [31] R. M. Hill and D. E. Kaplan, Phys. Rev. Lett. **14**, 1062 (1965).
- [32] R. W. Gould, Phys. Lett. **19**, 477 (1965).
- [33] I. D. Abella, N. A. Kurnit, and S. R. Hartman, Phys. Rev. **141**, 391 (1966).

- [34] R. W. Gould, T. M. O'Neil, and J. H. Malmberg, Phys. Rev. Lett. **19**, 219 (1967).
- [35] J. H. Malmberg, C. B. Wharton, R. W. Gould, and T. M. O'Neil, Phys. Fluids **11**, 1147 (1968).
- [36] J. D. Crawford and T. M. O'Neil, Phys. Fluids **30**, 2076 (1987).
- [37] T. M. O'Neil to R. W. Gould, private communication (1997).